
Polymer Dynamics in External Fields

Franz Xaver Walther Eberhard Schlagberger



Munich, 2006

Polymer Dynamics in External Fields

Franz Xaver Walther Eberhard Schlagberger

Dissertation
der Fakultät für Physik
der Ludwig-Maximilians-Universität
München

vorgelegt von
Franz Xaver Walther Eberhard Schlagberger
geboren am 20. September 1975 in Bremen

München, Mai 2006

Erstgutachter: Prof. Dr. Roland R. Netz

Zweitgutachter: Prof. Dr. Erwin Frey

Tag der mündlichen Prüfung: 11. Juli 2006

Contents

Abstract	vii
Zusammenfassung	ix
1 Introduction	1
2 Polymers in Solution: Analytical and Simulation Tools	5
2.1 Hydrodynamic simulation methods at low Reynolds numbers	5
2.1.1 Stokes flow dynamics	7
2.1.2 Comparison of Brownian Dynamics simulations with other methods	8
2.2 Electrostatic effects	9
3 Sedimentation of Semiflexible Rods	13
3.1 Modeling hydrodynamics of flexible objects	13
3.1.1 Rigid body motion	13
3.1.2 Bead model	14
3.2 Zero temperature results	16
3.2.1 Deformation	16
3.2.2 Orientation	18
3.3 Full temperature results	19
3.3.1 Stationary motion	19
3.3.2 Dynamics	21
3.4 Anisotropic materials	23
3.5 Discussion	25
3.5.1 Hydrodynamic orientation in the literature	25
3.5.2 Comparison with experiments	26
4 Driven Rotation of a Semiflexible Filament	29
4.1 Modeling bacterial motility	29
4.2 Shape transition of the rotating rod	32
4.3 Propulsion efficiency	35
5 Sedimentation of Flexible Polymers	39
5.1 Comparison of different models and approximations	40
5.2 Compactification of short chains	44
5.3 Unfolding transition	47
5.3.1 Linear chains	47

5.3.2	Circular chains	50
5.4	Discussion	51
6	Salt Dependent Diffusion of Semiflexible Polymers	53
6.1	Diffusion of neutral semiflexible chains	54
6.2	Salt dependence of polymer diffusion	60
6.2.1	Method of investigation	60
6.2.2	Charged spheres	61
6.2.3	Rod-like polymers	63
6.2.4	Semiflexible polymers	64
6.3	Discussion and comparison with experiments	68
7	Electrophoresis of Charged Rods	71
7.1	Polarizabilities of ion clouds	72
7.1.1	Method of investigation and definitions	72
7.1.2	Analytical calculations	76
7.1.3	Effects of polymer and salt concentration	81
7.1.4	Length dependence	82
7.1.5	Free versus bound counterions	84
7.2	Electric birefringence and anomalies	85
7.2.1	Arguments for a hydrodynamic orientation	86
7.2.2	Discussion	89
8	General Conclusions and Outlook	93
A	Description of the Numerical Method	95
A.1	Langevin iteration	95
A.2	Data analysis	99
B	Treatment of Hydrodynamic Orientation	101
B.1	Quasi-rigid bodies in the bead-model approximation	101
B.2	Perturbative calculation of a three-bead rod	102
B.3	Consistency checks with analytical results	104
B.4	Diffusion of semiflexible chains - some calculations	106
	Bibliography	109
	List of Publications	117
	List of Figures	119
	Acknowledgments	121
	Curriculum Vitae	123

Abstract

The dynamics of single semiflexible polymers in solution under the influence of an external field are investigated with Brownian Dynamics simulations. Hydrodynamic interactions are included on the Rotne-Prager level and proof to be essential. Model equations are used to derive scaling laws. The work consists of five projects that are distinct but closely related to each other:

In the first project, a neutral semiflexible particle is moved by centrifugal or gravitational forces relative to quiescent fluid. A coupling between hydrodynamic interactions and flexibility leads - depending on the elastic parameters - to a rod orientation perpendicular to the external field. This coupling is also investigated for a filament that is rotated at one end by some external torque (second project). Above a critical torque the filament folds itself around the rotational axis, with important consequences for the propulsion with a nano-machine. The third project deals with flexible polymers in an ultracentrifuge where a novel compactification and unfolding scenario is predicted: The established theories on sedimentation use the preaveraging approximation of the hydrodynamic interactions and cannot explain the polymer configurations at high fields consisting of a dense head and a long tail, which make a new efficient separation technique possible. In the fourth project, the diffusion of charged semiflexible polymers under different salt conditions is treated. Ions are included explicitly and not on a mean-field level. The theory of electrolyte friction for spherical objects is qualitatively extended to semiflexible polymers. A heuristic formula for the diffusion constant over the whole range of persistence lengths is proposed. In the final project, the hydrodynamic orientation mechanism found in the first project is suggested as a possible source of anomalous electric birefringence which is observed for rod-like polymers. It is compared with the competing parallel induced dipole orientation. The dependence of the polarizability on rod length, salt and polymer concentration is clarified.

Zusammenfassung

Die Dynamik von semiflexiblen Polymeren in Lösung in einem äußeren Feld wird mittels Simulationen der Brownschen Dynamik untersucht. Hydrodynamische Wechselwirkungen werden auf dem Rotne-Prager Niveau berücksichtigt und stellen sich als wesentlich heraus. Modellgleichungen werden aufgestellt um Skalengesetze herzuleiten. Die Arbeit besteht aus fünf getrennten aber benachbarten Teilprojekten:

Im ersten Projekt wird ein semiflexibles Teilchen mittels Zentrifugal- oder Gravitationskräfte durch eine stille Flüssigkeit bewegt. Die Kopplung zwischen hydrodynamischen Wechselwirkungen und der Flexibilität des Teilchens bewirkt eine Senkrecht-Stellen des Teilchens zum äußeren Feld, je nach den elastischen Parametern. Diese Art der Kopplung wird ferner für ein Filament untersucht, das an einem Ende durch ein äußeres Drehmoment rotiert wird (zweites Projekt). Oberhalb eines kritischen Drehmoments wird das Filament um die Rotationsachse gebogen, was für den Antrieb einer möglichen Nano-Maschine von Bedeutung ist. Das dritte Projekt handelt von flexiblen Polymeren in einer Ultrazentrifuge; ein neuartiges Kompaktifizierungs- und Entfaltungsszenario wird vorhergesagt: Bisherige theoretische Untersuchungen verwenden eine Preaveraging-Näherung zur Beschreibung der hydrodynamischen Wechselwirkungen und können die Polymer-Konfigurationen bei starken Feldern bestehend aus einem dichten Kopf und einem langen Schwanz nicht erklären, welche eine neue effiziente Trennmethode ermöglichen. Im vierten Projekt wird die Diffusion geladener semiflexibler Polymere unter verschiedenen Salzlösungsbedingungen untersucht. Ionen werden explizit und nicht auf dem Mean-Field Niveau berücksichtigt. Die Theorie der Elektrolyten-Reibung für sphärische Objekte wird erweitert für semiflexible Polymere. Eine heuristische Gleichung für die Diffusionskonstante im gesamten Bereich der Persistenzlänge wird vorgeschlagen. Im letzten Projekt wird der im ersten Projekt gefundene hydrodynamische Orientierungsmechanismus als mögliche Ursache für anomale Doppelbrechung stabförmiger Polymere interpretiert und der konkurrierenden parallelen Orientierung mittels induzierter Dipole gegenübergestellt. Die Abhängigkeit der Polarisierbarkeit von der Stablänge und der Salz- und Polymerkonzentration wird geklärt.

Chapter 1

Introduction

An important branch of biophysics deals with the characterization and manipulation of macromolecules. Classical problems are the separation of deoxyribonucleic acid (DNA) strands according to their molecular weight by sedimentation or electrophoresis, the function of actin filaments in the cell [7, 59, 152] and the physical properties of the rod-like viruses [31]. In many experimental situations the macromolecules are subject to an external field. In the case of capillary electrophoresis it is a static electric field that is homogeneous on the scale of the sample dimension. Static electric fields are used also in an electric birefringence experiment where the mean orientation of the particles is recorded by optical means. A third example is ultracentrifugation in which the sedimentation velocity gives valuable information about the physical properties of the solute particle, and which is also used for size separation.

Usually these biopolymers are dissolved in water so that hydrodynamic effects have to be taken into account. The sizes of these molecules, which are in the range from nanometers to several micrometers (see fig. 1.1), make low-Reynolds number hydrodynamics applicable and the inclusion of the fluctuating Brownian forces in the theoretical description indispensable. The presence of an external field gives rise to non-equilibrium phenomena.

Although many of the phenomena I discuss in my thesis are known for decades, their theoretical description still presents a challenge. The reason for this is twofold: On the one hand, the use of statistical mechanics is complicated by the fact the systems are often far from equilibrium. On the other hand, analytical solutions of the hydrodynamic equations in the presence of flexible objects are in general not possible, since the particle surface which gives a boundary condition to the fluid velocity changes with time. Due to this complications, available theories often rely on (more or less justified) approximations and usually are restricted to situations that are close to certain limiting cases which are known analytically (rigid bodies, thermodynamic equilibrium). Numerical studies, however, were until recently restricted to very simple systems.

This is the point where my thesis sets in. Simulations avoid many of the approximations made so far, and at the same time, they provide a clear physical picture that is very useful to devise models in order to derive scaling laws. They shed light on some unresolved issues, and some unexpected new phenomena are predicted. Most of these problems are as relevant as thirty years ago, some have received even more attention in the last ten years: Modern optical detection systems have revived the interest in analytical ultracentrifugation as a contemporary research tool [92]; and many experiments with polymers can now work with - in principle - single molecule precision [27, 86]. The dynamics of single polymers can often be directly

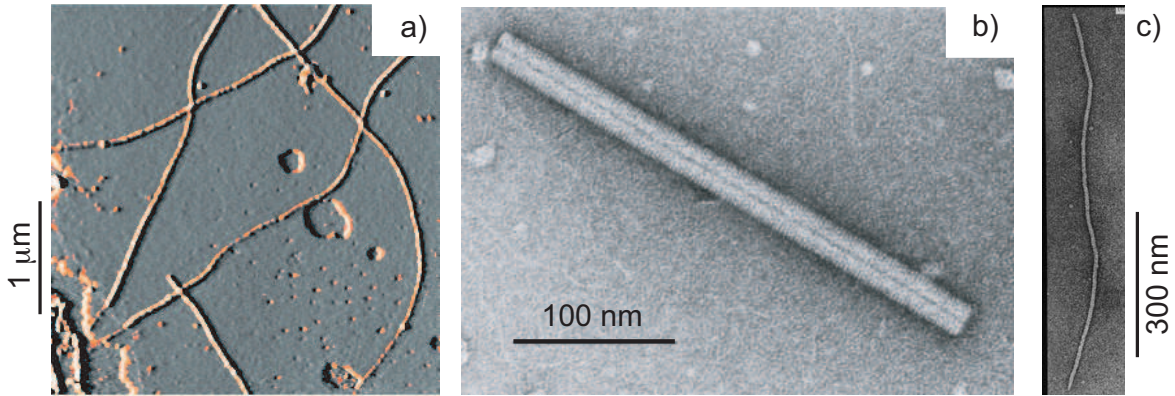


Figure 1.1: Examples of biologically important semiflexible rods: a) Electron micrograph of actin filaments (f-actin) obtained from J. Kwak’s webpage (elchem.kaist.ac.kr/jhkwak). b) Tobacco mosaic virus (TMV) from the virus database of the International Committee on Taxonomy of Viruses (www.ncbi.nlm.nih.gov/ICTVdb). c) fd-virus, picture taken from [116].

tested in experiments [99], without a detour to bulk properties.

Outline of the Thesis

This work investigates the non-equilibrium dynamics of single polymers in solutions in external fields. The long-ranged hydrodynamic interactions play an important role. No restriction on the flexibility of the polymers is made but special emphasis is paid to the limiting cases of a weakly bending rod and a very flexible chain. The thesis consists of five projects: In the first three projects neutral polymers are investigated, or rather situations where the charge of the polymers plays a minor role. New phenomena special to rod-like, semiflexible and flexible polymers are the subject of chapter 3, 4, and 5, respectively. The last two projects deal with charged polymers in a salt solution, the diffusion constant of semiflexible polymers, and the polarizability and birefringence of rod-like polymers in electric fields.

The thesis starts with an overview of the techniques used for a dynamical description of soft materials in solution. The theoretical foundations of the simulation methods are sketched, and the choice of Brownian Dynamics simulations as the central tool in this work is motivated.

In chapter 3 the Brownian Dynamics method is used to investigate the hydrodynamic properties of a single microscopic semiflexible rod in a homogeneous Stokes flow. Such a situation is especially relevant for ultracentrifugation experiments when a dilute solution of rod-like particles is subject to strong centrifugal fields, but under certain circumstances also for electrophoresis. As a result of a coupling between flexibility and hydrodynamic interactions the rods are oriented with their long axis perpendicular to the external field. Analytical calculations for a simple model support this finding, scaling laws are established that predict a strong dependence on the ratio of the rod length to the rod diameter.

The interplay between flexibility and hydrodynamic interactions is further investigated for a semiflexible filament rotated at one end as relevant for the propulsion of several types of bacteria and nano-machines (chapter 4). Most of the work in this field of mathematical biology concentrated on the fluid dynamics of rigid objects. Here it is shown that shape transformations of the rotating flagellum can strongly affect the propulsion efficiency and can

even lead to the design of a rectifying device that yields forward thrust irrespective of the direction of rotation.

In chapter 5 elastic polymers in strong centrifugal fields are considered. Hydrodynamic shielding leads to a compactification at small fields which for short chains gives rise to compact globules. Longer chains unfold at higher fields; their limiting conformation at very high fields has a tadpole shape consisting of a dense head plus a tail parallel to the direction of motion. These conformational changes strongly affect the sedimentation coefficient in a way much different from the established model proposed by B. Zimm. Our results explain the sedimentation behavior of closed polymer rings, for which the Zimm model gives no deformation and thus no dependence of the sedimentation coefficient on the driving force.

Chapter 6 deals with the diffusion constant of semiflexible polyelectrolytes in solutions containing different amounts of added salt, which was recently investigated with Fluorescence Correlation Spectroscopy [8, 154]. In a first step a heuristic formula for the diffusion constant as a function of the persistence length is proposed that interpolates between the swollen (good solvent) flexible limit and the rod limit. The presence of salt does not only lead to conformational changes that affect the diffusion constant but also to an increased friction due to the small ions surrounding the polyelectrolyte. Existing theories on electrolyte friction of charged spheres are reviewed and - at least qualitatively - extended to the diffusion of semiflexible polymers.

The polarizability of the ion cloud of a rod-like particle and its dependence on ionic strength and rod length is investigated in chapter 7. The question whether the complete cloud or rather the close and strongly bound counterions dominate the polarization is discussed. A strong and unexpected dependence of the polarizability on polymer concentration is discovered. The induced dipoles lead to an orientation of the particles in the electric field that can be measured in birefringence and dichroism experiments. Possible sources of anomalous birefringence are presented with a focus on the perpendicular orientation mechanism of chapter 3.

The work closes by relating the five projects with each other. A short outlook is given.

Chapter 2

Polymers in Solution: Analytical and Simulation Tools

In this chapter, I present and discuss methods and approximations that are used throughout the thesis. The systems under investigation are dilute and semidilute solutions of polymers that can be flexible or semiflexible. Using a very large persistence length also microscopic rodlike objects can be described. Their usually mesoscopic size makes a classical mechanics description possible.

2.1 Hydrodynamic simulation methods at low Reynolds numbers

To reduce the number of degrees of freedom in a dynamical system one would ideally use projection operators to separate out the dynamics of the relevant variables (e.g. the positions of the molecules of interest); the irrelevant variables (e.g. positions and momenta of the solvent molecules) should then only appear in the memory function and the noise term of a generalized Langevin equation [118, 194]. Such a method is exact but in most cases only formally possible, i.e. does not lead to explicit results. One needs further assumptions to extract physical properties. One possible set of assumptions is that the masses and momentum relaxation times of the Brownian particles are much larger than those of the solvent molecules; and that their velocities are much smaller than the buffeting solvent particles. A further requirement is that continuous hydrodynamics can be used at this microscopic scale to include solvent-mediated interactions between Brownian particles [30]. Since all these objects are at the micrometer and nanometer scale a Reynolds number

$$\text{Re} = \frac{\rho L v}{\eta} \quad (2.1)$$

much less than unity can safely be presumed. It will be checked later with explicit examples. ρ and η are the mass density and viscosity of the solvent, and L and v the length and velocity scale. The equations for the incompressible stationary low-Reynolds number flow (*Stokes flow*) read [63]

$$\eta \nabla^2 \mathbf{u}(\mathbf{r}) - \nabla P(\mathbf{r}) = -\mathbf{f}(\mathbf{r}) \quad (2.2)$$

$$\nabla \cdot \mathbf{u} = 0 \quad (2.3)$$

where \mathbf{u} is the velocity field of the fluid, P the pressure and \mathbf{f} the density of external forces. Its Green's function is called the *Oseen tensor* [137]

$$H(|\mathbf{r}_i - \mathbf{r}_j|) = \frac{1}{8\pi\eta|\mathbf{r}_i - \mathbf{r}_j|} (\mathbf{I} + \hat{\mathbf{r}}_{ij} \otimes \hat{\mathbf{r}}_{ij}) . \quad (2.4)$$

$\hat{\mathbf{r}}_{ij}$ is short for \mathbf{r}_{ij}/r_{ij} , $\mathbf{r}_{ij} = \mathbf{r}_i - \mathbf{r}_j$ and $r_{ij} = |\mathbf{r}_i - \mathbf{r}_j|$. \mathbf{I} is the 3×3 unit matrix. The velocity field at a point \mathbf{r}_i created by distant particles j is then given by

$$\mathbf{u}(\mathbf{r}_i) = \sum_{i \neq j} H(r_{ij}) \cdot \mathbf{F}_j \quad (2.5)$$

where \mathbf{F}_j is the direct force on particle j . It can be used to calculate the indirect, solvent-mediated force on particle i at position \mathbf{r}_i if one assumes that the flow field has the velocity of the Brownian particle at its surface (“stick boundary condition”).

Ermak and McCammon [38] used this as a starting point to derive a position-Langevin equation that is suitable for simulations. Integration over one time step Δt leads to

$$\mathbf{r}_i(t + \Delta t) = \mathbf{r}_i(t) + \sum_{j=1}^N \mu_{ij}(t) \cdot \mathbf{F}_j(t) \Delta t + k_B T \sum_{j=1}^N \nabla_{\mathbf{r}_j} \cdot \mu_{ij}(t) \Delta t + \Delta \boldsymbol{\eta}_i(t) . \quad (2.6)$$

$\nabla_{\mathbf{r}_j}$ is the gradient with respect to the position of the j th particle. The mobility matrix $\mu_{ij}(t)$ is equal to Oseen tensor (evaluated at time t) for $i \neq j$ and equal to the Stokes mobility of a sphere of radius a_i for $i = j$, $\mu_{ii} = \mathbf{I}/(6\pi\eta a_i)$. For this special choice of μ_{ij} the derivative $\nabla_{\mathbf{r}_j} \cdot \mu_{ij}$ vanishes. $\Delta \boldsymbol{\eta}_i(t)$ is a Gaussian random vector the components of which obey

$$\langle \Delta \eta_i^\alpha(t) \rangle = 0 \quad (2.7)$$

$$\langle \Delta \eta_i^\alpha(t) \cdot \Delta \eta_j^\beta(t') \rangle = 2 k_B T \Delta t \delta_{tt'} \mu_{ij}^{\alpha\beta}(t) \quad (2.8)$$

with Latin letters indicating different particles and Greek letters space directions. The correlation of the noise at discrete times t and t' insures the validity of the fluctuation-dissipation theorem. It is important that Δt is small enough that the forces and positions do not change appreciably, but that it is at the same time large compared to the momentum relaxation time to insure local thermodynamic equilibrium: $\Delta t \gg m_i \mu_{ii}$, where m_i is the mass of particle i . In the continuum limit, $\Delta t \rightarrow 0$, eq. (2.6) can be written as a stochastic differential equation [134]

$$d\mathbf{r}_i = \sum_{j=1}^N \mu_{ij}(t) \cdot \mathbf{F}_j(t) dt + k_B T \sum_{j=1}^N \nabla_{\mathbf{r}_j} \cdot \mu_{ij}(t) dt + d\boldsymbol{\eta}_i(t) \quad (2.9)$$

where the Itô convention is used.

If always a finite time step Δt is assumed eq. (2.6) can be written as

$$\dot{\mathbf{r}}_i(t) = \sum_{j=1}^N \mu_{ij} \cdot \mathbf{F}_j + k_B T \sum_{j=1}^N \nabla_{\mathbf{r}_j} \cdot \mu_{ij} + \boldsymbol{\xi}_i(t) . \quad (2.10)$$

$\boldsymbol{\xi}_i(t)$ is a stochastic velocity process the integral of which over a time step Δt gives the random increment $\Delta \boldsymbol{\eta}_i$ [1]. Its expectation values are

$$\langle \xi_i^\alpha(t) \rangle = 0 \quad (2.11)$$

$$\langle \xi_i^\alpha(t) \cdot \xi_j^\beta(t') \rangle = 2 k_B T \delta(t - t') \mu_{ij}^{\alpha\beta}(t) \quad (2.12)$$

where the time is now continuous.

Are the above made requirements met? For colloidal particle of the order 100 nm or larger this seems to be true. But in the following chapters, Langevin dynamics is also to be applied to single ions which are certainly smaller than water molecules. One way of circumventing this problem is to say that ions in water always have a hydration shell so that one should rather treat the whole complex, ion plus at least one layer of water molecules, as the appropriate Brownian particle (cf. the discussion and references in [149]). Here I will take the point of view that Brownian dynamics constitutes a model for calculating non-equilibrium properties of a system defined by mobilities and a Hamiltonian.

2.1.1 Stokes flow dynamics

Despite the linearity of the Stokes flow equations (2.2, 2.3) only highly symmetric problems can be solved in closed form. A general introduction can be found in [63, 75]. An expression for the hydrodynamic interaction between Brownian particles, i.e. for the mobility tensor μ_{ij} , is sought that can be used in the Langevin equation. The Oseen description is only valid for widely separated point-like bodies and includes only pairwise interactions. A way of improving this is the *method of reflections* [63] for a collection of spherical particles, which gives an expansion in inverse powers of the particle separations divided by their radii, r_{ij}/a_i . In eq. (2.6) one restrains oneself to pairwise interactions, the neglect of multi-particle interactions being motivated by the supposed diluteness of the system. An expansion to very high powers of r_{ij}/a_i for two spheres is given in [40, 156]. For equal sphere radii a and stick boundary conditions one finds for the lowest correction to the Oseen tensor

$$\mu_{ij} = \frac{1}{8\pi\eta r_{ij}} \left[\left(\mathbf{I} + \hat{\mathbf{r}}_{ij} \otimes \hat{\mathbf{r}}_{ij} \right) + \frac{2a^2}{r_{ij}^2} \left(\frac{\mathbf{I}}{3} - \hat{\mathbf{r}}_{ij} \otimes \hat{\mathbf{r}}_{ij} \right) \right] , \quad i \neq j \quad (2.13)$$

while the self-mobility μ_{ii} is unaffected. For two spheres with different radii a_1 and a_2 , a^2 has to be replaced by $(a_1^2 + a_2^2)/2$. Mazur and van Saarloos used a different scheme [112] and obtained additional multi-body terms, but their result agrees with eq. (2.13) at the $\mathcal{O}(r_{ij}^{-3})$ level. It should be remarked that $\mu_{ij} \cdot F$ with μ_{ij} given by eq. (2.13) is just the second order in a multipole expansion for the velocity perturbation of the fluid at distance r_{ij} far away from the sphere if a unit force F is homogeneously distributed over the surface of the sphere. The calculation can be found e.g. in [106, 188].

Rotne and Prager used a variational method to derive eq. (2.13) for non-overlapping equal-sized spheres $i \neq j$ and

$$\mu_{ij} = \frac{1}{6\pi\eta a} \left[\left(1 - \frac{9}{32} \frac{r_{ij}}{a} \right) \mathbf{I} + \frac{3}{32} \frac{r_{ij}}{a} \hat{\mathbf{r}}_{ij} \otimes \hat{\mathbf{r}}_{ij} \right] , \quad i \neq j \quad (2.14)$$

for overlapping ones. The self-mobility is again given by the Stokes expression

$$\mu_{ii} = \mathbf{I}/(6\pi\eta a) \equiv \mu_0 \mathbf{I} \quad (2.15)$$

It will be henceforth referred to as *Rotne-Prager tensor*. By construction it is positive definite. A further useful property is that $\nabla_{\mathbf{r}_j} \cdot \mu_{ij} = 0$. Since it is the hydrodynamic interaction tensor used in this thesis I will spend a few words on how it was derived: The energy dissipation rate $\dot{\epsilon}$ of a collection of beads reads

$$\dot{\epsilon} = \frac{1}{2\eta} \int_V \sum_{\alpha\beta} \sigma'_{\alpha\beta} \sigma'_{\alpha\beta} d^3r = \sum_i \sum_{\alpha\beta} F_i^\alpha \mu_{ij}^{\alpha\beta} F_j^\beta , \quad \alpha, \beta = 1, 2, 3 , \quad (2.16)$$

where $\sigma'_{\alpha\beta}$ is the traceless, symmetric viscous stress tensor and F_i the force on sphere i . V is the space outside all spheres. Any trial viscous stress $\sigma'^{(1)}$ fulfilling the correct boundary conditions and the corresponding trial mobility tensor $\mu^{(1)}$ give an upper limit to the true energy dissipation via eq. (2.16). $\mu^{(1)}$ itself is an upper limit to the true μ and hence positive definite. If one uses for $\sigma'^{(1)}$ the superposition of single sphere solutions $\sigma'_i^{(1)}$, $\sigma'^{(1)}(\mathbf{r}) = \sum_i \sigma'_i^{(1)}(\mathbf{r})$, and extends the region of integration over the whole space (letting $\sigma'_i^{(1)}$ be zero inside sphere i) one finds precisely eq. (2.13) for non-overlapping beads, which is somehow expected. For overlapping beads one obtains eq. (2.14) with the same argument.

So far all beads were just translating frictional points with first order corrections for their radii. In principle one should also include rotational degrees of freedom and use the *grand mobility matrix* \mathcal{M} defined by

$$\begin{pmatrix} \mathbf{V} \\ \mathbf{\Omega} \end{pmatrix} = \begin{bmatrix} \mathcal{M}^{tt} & \mathcal{M}^{tr} \\ \mathcal{M}^{rt} & \mathcal{M}^{rr} \end{bmatrix} \begin{pmatrix} \mathcal{F} \\ \mathcal{T} \end{pmatrix} \quad (2.17)$$

where the vector \mathbf{V} contains the velocities of all beads, $\mathbf{\Omega}$ the angular velocities, \mathcal{F} the forces and \mathcal{T} the angular momenta. \mathcal{M}^{tt} is the translational mobility tensor considered so far. In polymer physics where the beads correspond to the monomers such an extension is necessary if one wants to describe torsional effects. Including rotational-translational coupling modifies also \mathcal{M}^{tt} if the spheres are not freely rotating, for correction terms see e.g. [58]. Rigid body Stokes flow dynamics will be described at the beginning of chapter 3.

Despite the smallness of the Reynolds number Re there are situations where the Stokes flow approximation breaks down. The dissipated energy from an object dragged through the fluid with some external force diverges due to the long-ranged character of the hydrodynamic interaction. The solution to this apparent problem is that for distances $r \sim \eta/(\rho u)$ the neglect of the non-linear term in the Navier-Stokes equation, $(\mathbf{u} \cdot \nabla) \mathbf{u}$, is not possible anymore so there is a natural cutoff [90]. u is the fluid velocity relative to the center of mass of the object. The case is related to the Stokes paradox: Equations (2.2) and (2.3) for the flow field $\mathbf{u}(\mathbf{r})$ around an infinite cylinder have no solution that fulfill both the boundary condition at the surface of the cylinder and at infinity. This problem is restricted to sedimentation. For a charge-neutral system in an electric field the hydrodynamic interactions decay much faster at large distances; positive and negative charges give opposite contributions to the flow field such that just force dipole effects remain.

A last comment concerns the approximation of distant spheres. For nearly touching spheres *lubrication* effects will give qualitatively new features and can be treated using different methods [34]. Although monomers in a polymer chain are not far away from each other, it is the long ranged hydrodynamic interactions that determine many of the dynamical aspects [32] so that lubrication is neglected in this work.

2.1.2 Comparison of Brownian Dynamics simulations with other methods

Eq. (2.6) for the time evolution of a collection of particles in a fluid is called the Brownian Dynamics methods. It will be the method of choice in this thesis. It is especially useful for dilute solutions. Brownian Dynamics simulations offer the possibility to observe the dynamical evolution of the system, e.g. the collapse and unfolding of a polyelectrolyte [122, 185], and does not just calculate averages. In that point it has the same advantage as Molecular Dynamics. The solvent molecules only enter the mobility matrix and the noise term but at the price that every time step the correlated random numbers have to be calculated according to eq. (2.8) by

Cholesky decomposition or a similar method (see appendix A). The number of floating point operations per Cholesky decomposition grows as the third power of the number of particles N which makes the method impractical if N is greater than several hundreds.

Another difficulty arises if the system displays several widely separated time scales. For example in the polarizability studies of chapter 7 the motion of the ions is much faster than the rotational diffusion time of the rod-like polymer. The time step is determined by the smallest time scale but the total simulation time by the longest time scale. This difficulty can be circumvented if instead of following physical trajectories of the system a more efficient phase space sampling is done. It was shown [179, 190] that the *Metropolis Monte Carlo* method can be used to describe non-equilibrium stationary systems. But unless cluster algorithms are applied the problem of separated time scales remains [100]. Another approach to this problem are *multiscale simulation* techniques [84].

There are other ways to include the effect of the solvent molecules in a mesoscopic simulation than using a Langevin equation. *Dissipative Particle Dynamics* (see [60] for a derivation and [171] for polymer dynamics) describes blocks of molecules that move together in a coherent fashion subject to soft potentials and governed by predefined collision rules. The soft potential allows the use of a larger time step. One can therefore explore much longer time scales. Hydrodynamic effects are accounted for by extended soft blocks of solvent particles interacting with the polymer.

Another off-lattice alternative is the *Multi-Particle-Collision Dynamics* method (MPCD) [101, 186]. In a molecular simulation with explicit solvent molecules most of the time is spent to evaluate the solvent dynamics in great detail which is not necessary if one is just interested in their hydrodynamic influence on colloidal particles. In MPCD a great number of solvent particles, typically of the order of 10^5 , is included but their dynamics is very simplified: In the first half of every time step the new position of particle i is calculated by $\mathbf{r}_i(t + \Delta t) = \mathbf{r}_i(t) + \mathbf{v}_i(t) \Delta t$. $\mathbf{v}_i(t)$ is the velocity of the i th solvent particle. In the second half-step the particles are grouped into small cells which are then rotated around their centers of mass by a random angle that differs from cell to cell. No direct interaction is imposed on the solvent particles which makes their evaluation fast. Coupling to e.g. polymers is done by including monomers in the rotation of the cells. Momentum and energy are conserved; the method is in principle not restricted to small Reynolds numbers.

In *Lattice Boltzmann* methods (for a review see [23]) time, positions and velocities are discretized, and Boltzmann equation for the fluid is solved. It can also be used for charged colloids [72] where in addition to the solvent particles the small ions are simulated on a lattice.

2.2 Electrostatic effects

Most polymers relevant for biological applications are charged and dissociate ions in water. It would therefore be a serious neglect for a realistic treatment not to include the effects of the ion cloud, especially if electric fields are applied. On a mean field level one solves the *Poisson-Boltzmann equation* for the mean electrostatic potential Φ around a fixed point charge Ze [149] which reads in SI units

$$\nabla^2 \Phi(\mathbf{r}) = -\frac{Ze}{\epsilon\epsilon_0} \delta(\mathbf{r}) - \sum_{\alpha} \frac{z_{\alpha} e c_{\alpha}}{\epsilon\epsilon_0} \exp[Ze \Phi(r)]. \quad (2.18)$$

The index α numbers the different ionic species with valencies z_{α} and bulk densities c_{α} . e is the elementary charge. The Poisson-Boltzmann equation is the result of replacing the fluctuating

electrostatic potential by its mean value. It neglects correlations among the fluctuations and hence many important physical effects [150] which must be included in an extended procedure (see e.g. [121]). In the limit of dilute solutions the exponential can be expanded in a Taylor series leading to

$$\Phi(\mathbf{r}) = \frac{Ze}{4\pi\epsilon\epsilon_0 r} \exp[-\kappa r] \quad (2.19)$$

where the *Debye-Hückel screening length* is given by

$$\kappa^{-1} = \left(4\pi \ell_B \sum_{\alpha} z_{\alpha}^2 c_{\alpha} \right)^{-1/2}. \quad (2.20)$$

Here a new length scale is introduced, the *Bjerrum length* [15]

$$\ell_B = \frac{e^2}{4\pi\epsilon\epsilon_0 k_B T}, \quad (2.21)$$

which is about 0.7 nm in water at room temperature.

Electrostatic effects could now be included by assuming a background salt concentration and adding screened Coulombic forces using eq. (2.19) between the Brownian particles in the Langevin equation (2.10). This would only give a minimal extra computational cost. But it has several disadvantages: In order to describe the deformation of the counterion cloud with respect to its equilibrium distribution one could add “Brownian” counterions to the system and let all charged particles interact with screened Coulombic forces. This would mean that counterions and salt ions are treated on a very different footing despite the fact that they have similar or even equal sizes and charges. Further, the non-equilibrium distribution of the salt ions (in the presence of external fields and conduction) is not known; it might be dangerous to use its equilibrium value instead. And after all the above mentioned approximations (mean field, dilute solutions) need not necessarily be justified for the investigated systems.

For these reasons I will include counterions and salt ions explicitly as Brownian particles. The charged polymer or polyelectrolyte (PE) will be simulated as a string of charged spherical monomers. The Langevin equation of motion then reads in case of a Rotne-Prager or Oseen mobility tensor

$$\dot{\mathbf{r}}_i(t) = \sum_{j=1}^{2N+2N_s} \mu_{ij} \cdot \left[-\nabla_{\mathbf{r}_j} U(\{\mathbf{r}_k\}) + z_j e \mathbf{E} \right] + \boldsymbol{\xi}_i(t) \quad (2.22)$$

where \mathbf{E} is the external (static homogeneous) electric field and

$$\begin{aligned} U(\{\mathbf{r}_k\}) = & U_{\text{pol}} + k_B T \sum_{i \neq j} \frac{z_i z_j \ell_B}{r_{ij}} \\ & + \epsilon_{LJ} \sum_{i \neq j} \Theta(2a - r_{ij}) \left[\frac{(2a)^{12}}{r_{ij}^{12}} - \frac{2(2a)^6}{r_{ij}^6} + 1 \right]. \end{aligned} \quad (2.23)$$

N is the number of monomers and hence the number of counterions, N_s the number of pairs of salt ions. The first term is the stretching and bending potential of the polymer which will be specified later. The second term gives the Coulomb energy between two charged Brownian particles, monomers or small ions, with valencies z_i and z_j , and the last term, the truncated Lennard-Jones potential of strength $\epsilon_{LJ} = k_B T$, prevents strong overlap of oppositely charged

particles and is responsible for the swollen (excluded volume) behavior of the polymer chain. Θ is the Heavyside step function. For simplicity, all Brownian particles have the same radius a and magnitude of valency z ,

$$z_i = s_i z \quad , \quad s_i = \pm 1 . \quad (2.24)$$

Rescaling all lengths by the monomer radius a and energies by $k_B T$ eq. (2.23) can be written as

$$\tilde{U}(\{\tilde{\mathbf{r}}_k\}) = \tilde{U}_{\text{pol}} + \sum_{i \neq j} \left\{ \frac{s_i s_j \zeta}{\tilde{r}_{ij}} + \Theta(2 - \tilde{r}_{ij}) \left[\frac{2^{12}}{\tilde{r}_{ij}^{12}} - \frac{2^7}{\tilde{r}_{ij}^6} + 1 \right] \right\} \quad (2.25)$$

with the *coupling parameter*

$$\zeta = \frac{z^2 \ell_B}{a} . \quad (2.26)$$

Since the linear charge density of the polyelectrolyte is $z/(2a)$ it is related to the Manning parameter ξ_M [108] by

$$\zeta = 2 \xi_M . \quad (2.27)$$

From the Debye-Hückel theory I borrow the expression of the screening length including salt ions and counterions but not the polyelectrolyte in the screening

$$\tilde{\kappa}^{-1} = \left(4\pi \zeta (N + 2N_s) / \tilde{B}^3 \right)^{-1/2} . \quad (2.28)$$

B is the size of the cubic simulation box. For finite polymer and hence finite counterion density it is natural to include not only the background salt but also the counterions in κ . The repulsion between the polyelectrolytes on the other hand renders their screening unimportant up to length scales of their mutual overlap. A thorough discussion is given in [119]. If there are $N_p > 1$ polyelectrolytes per simulation cell all $N_p N$ counterions are included.

Chapter 3

Sedimentation of Semiflexible Rods

Rod-like objects are ubiquitous in colloidal science and biophysics. Their contour lengths span the range from several nanometers, as e.g. short DNA strands (persistence length of about 50 nm under physiological conditions), up to several hundreds of micrometers like microtubules (persistence length of the order of millimeters [138]). Beside biopolymers, synthetic polymers, carbon nanotubes and stiff viruses are important examples. Usually these rods are investigated in solution, which is mainly water. The size of these rods insures that low-Reynolds number physics is a good approximation. Often these rod-like particles are moved relative to the fluid by some external field, which can be the the electric field or the gravitational field in a sedimentation or ultracentrifugation experiment.

Optical methods like birefringence and dichroism [48] measurements are widely used to determine the average orientation of these particles. Electric birefringence has been applied to Tobacco Mosaic virus (TMV) [130], fd-virus [81, 82], different synthetic polyelectrolytes [89, 136] and actin filaments [78, 79]. Restricting oneself to electrostatic phenomena, an orientation with the direction of the largest polarizability parallel to the electric field is favored. An important contribution to the polarizability comes from the easily deformable counterion cloud accompanying each charged particles which is maximal along the long axis of the particle [122, 190]. The resulting parallel orientation is called normal birefringence.

Anomalous birefringence, i.e. perpendicular orientation, is sometimes observed for semidilute particle concentrations [69, 82, 136], low salt or rods with high aspect ratio. It is at present only understood for certain special situations [22]. This chapter aims at presenting an additional and so far overseen mechanism for anomalous birefringence of semiflexible rods that is based on the coupling of elastic and hydrodynamic degrees of freedom.

3.1 Modeling hydrodynamics of flexible objects

3.1.1 Rigid body motion

A rigid object moving relative to a *homogeneous* low Reynolds number flow experiences a torque only if it has a certain degree of asymmetry either in its shape (and hence the application of hydrodynamic stress) or with respect to the application of external forces: e.g. homogeneous bodies of revolution with fore-aft symmetry (like ellipsoids or cylinders) do not turn at all under the influence of the gravitational field. The argument rests on the linearity of the flow equation and thus need not be valid for intermediate or high Reynolds numbers. More formally, there is a linear relation between the total force F and torque T_P that act on

a rigid body on the one side, and its linear velocity and angular velocity, v_P and ω , on the other side [63]:

$$\begin{pmatrix} \mathbf{F} \\ \mathbf{T}_P \end{pmatrix} = \begin{bmatrix} \zeta_P^{tt} & \zeta_P^{tr} \\ \zeta_P^{tr\dagger} & \zeta_P^{rr} \end{bmatrix} \begin{pmatrix} \mathbf{v}_P \\ \boldsymbol{\omega} \end{pmatrix}. \quad (3.1)$$

P is a point at the surface of that body, \mathbf{v}_P the velocity of P , and \mathbf{T}_P is determined relative to P (the total force and angular velocity obviously do not depend on P). ζ_P^{tt} and ζ_P^{tr} etc. are constant 3×3 generalized resistance matrices that only depend on the origin P and the particle shape. There exists a unique point P , the *center of reaction*, at which ζ_P^{tr} is symmetric. For bodies with three mutual perpendicular symmetry planes (orthotropic bodies) ζ_P^{tr} even vanishes at this point. It is then called the *center of hydrodynamic stress*.

In Brownian Dynamics simulations, one is more interested in the inverse relation

$$\begin{pmatrix} \mathbf{v}_P \\ \boldsymbol{\omega} \end{pmatrix} = \begin{bmatrix} \mu_P^{tt} & \mu_P^{tr} \\ \mu_P^{tr\dagger} & \mu_P^{rr} \end{bmatrix} \begin{pmatrix} \mathbf{F} \\ \mathbf{T}_P \end{pmatrix}. \quad (3.2)$$

Again there exists a unique point, the *center of diffusion*, at which μ_P^{tr} is symmetric. It is in general different from the center of reaction [180]. In a bead model, one can - given the position of all particles and assuming them being fixed with respect to each other - calculate the instantaneous general mobility matrix with a procedure presented in the appendix [50, 54]. If the coupling term $\mu_P^{tr\dagger}$ is non-zero then one obtains rotational motion of the body even for vanishing \mathbf{T}_P .

The orientational distribution function of rigid cylinders and ellipsoids is uniform as shown above; no orientational angle with respect to the external field is favored. For *elastic* rods, however, hydrodynamic effects may reduce the symmetry of the particle via bending and other deformation modes [36]; the translational-rotational coupling becomes finite. It will be shown that rods with a small elasticity tend to orient perpendicularly to the direction of motion. Since all materials have finite elastic moduli, this mechanism is universal, and its magnitude will be the subject of the following section.

3.1.2 Bead model

To demonstrate this effect, I will look at a specific model, a long neutral chain composed of spherical subunits, interacting via elastic potentials and hydrodynamically with each other. Scaling relation for the mean bending, orientation and relaxation times are derived as a function of the elastic parameter, chain length and driving field. Hydrodynamic simulations confirm these predictions and at the same time provide the prefactors, which are often very different from unity. Analytical calculations for a three-bead chain will further support these findings.

In the simulations we model an elastic rod as a chain of $N = M + 1$ connected monomers which are numbered from $i = 0$ to $i = M$. M is therefore the number of bonds. The elastic potential U is the discrete version of the *extensible* worm-like chain model [97]

$$U(\{\mathbf{r}_k\}) = \sum_{i=0}^{M-1} \left[\frac{\gamma}{4a} [r_{i+1} - 2a]^2 + \frac{\varepsilon}{2a} [1 - \cos \vartheta_i] \right] \quad (3.3)$$

where ϑ_i is the angle between neighboring bonds \mathbf{r}_{i-1} and \mathbf{r}_{i+1} . Here ε and γ are the bending and stretching moduli, respectively, and a denotes the sphere radius. In the continuum limit

this corresponds to

$$U = \frac{1}{2} \int_0^L ds \left\{ \gamma \left[\left| \frac{\partial \mathbf{r}}{\partial s} \right| - 1 \right] + \varepsilon \left| \frac{\partial \hat{\mathbf{t}}}{\partial s} \right|^2 \right\} \quad (3.4)$$

which is similar to the model of Soda [166] and allows fluctuations around the unstretched chain. $\hat{\mathbf{t}}(s)$ is the unit tangent vector at position s . s does not necessarily correspond to the arc length along the chain if stretching is allowed, but rather to a continuous monomer number with the dimension of length. In the limit $\gamma \rightarrow \infty$ eq. (3.3) gives the discretized Kratky-Porod model [83].

The persistence length follows as

$$\ell_P = \varepsilon/k_B T. \quad (3.5)$$

For an *isotropic elastic cylinder* with radius a , bending and stretching moduli are determined by Young's modulus E_Y as [91] $\varepsilon = E_Y \pi a^4/4$ and $\gamma = E_Y \pi a^2$ which gives the relation

$$\varepsilon/\gamma = a^2/4. \quad (3.6)$$

The time evolution is governed by a Langevin equation of the type eq. (2.10)

$$\dot{\mathbf{r}}_i(t) = \sum_{j=0}^M \mu_{ij} \cdot \left[-\nabla_{\mathbf{r}_j} U + q\mathbf{E} \right] + \boldsymbol{\xi}_i(t) \quad (3.7)$$

where the external field \mathbf{E} is constant (for convenience pointing in z -direction) and acts similarly on all spheres. It can be gravitational or electric; in the first case q is the mass of one sphere, in the latter its charge. μ_{ij} is given by the Rotne-Prager expressions eqs. (2.13), (2.14) and (2.15). The vectorial random displacements $\boldsymbol{\xi}_i(t)$ furnish the coupling to a heat bath and are given by eqs. (2.11) and (2.12). Eq. (3.7) is iterated with a time step Δt .

For a wider applicability all quantities are rescaled (denoted with a tilde). The typical length scale is the monomer radius a . One could also use the chain contour length L ; but since I am interested in the explicit length dependence L/a the former rescaling seems to be more convenient. Different from later chapters of this thesis, the energy scale will not be $k_B T$ but rather qEa . The reason for this is that always an external field is present, but for the stability analysis the stochastic displacements are neglected. A natural time scale is the time needed for an isolated sphere of radius a to drift the distance a under the influence of \mathbf{E} , viz. $\mu_0 qE/a$. One is then left with the following rescaled parameters (besides the monomer number N)

$$\tilde{\gamma} = \frac{\gamma}{qE} \quad (3.8)$$

$$\tilde{\varepsilon} = \frac{\varepsilon}{qE a^2} \quad (3.9)$$

$$\tilde{E} \equiv \tilde{\beta} = \frac{qE a}{k_B T} \quad (3.10)$$

$$\tilde{\Delta} = \Delta t \frac{qE \mu_0}{a}. \quad (3.11)$$

In order to avoid inaccuracies and spurious oscillations for very stiff chains around their proper positions (see appendix A for a discussion) I chose the rescaled time step $\tilde{\Delta}$ in the range $10^{-3} - 10^{-5}$. Output values were calculated every 100 to 1000 steps; the total simulation time was in the range 10^7 to 10^9 steps depending on the number of monomers and the elastic parameters.

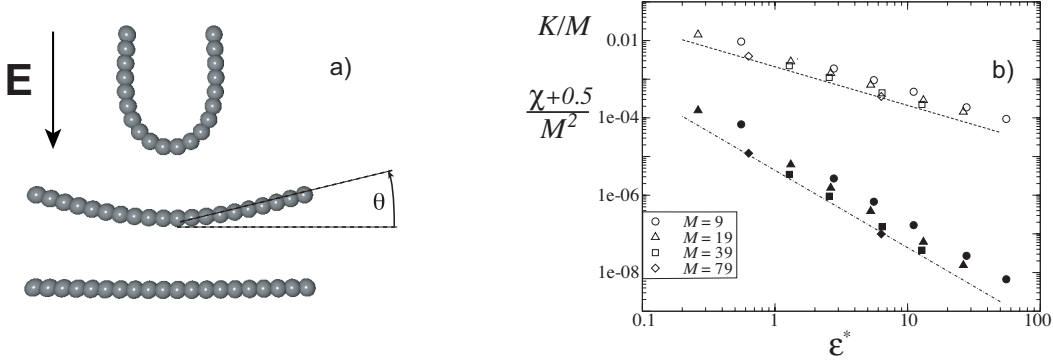


Figure 3.1: Stationary deformation of an isotropic elastic rod at *zero temperature*. a) Snapshots for $M = 19$ and $\epsilon^* = 0.03, 0.3$ and 3 (from top to bottom) of a rod moving downwards. b) Rescaled mean curvature K/M (open symbols) and alignment parameter $(\chi + 0.5)/M^2$ as a function of the rescaled rigidity ϵ^* confirming scaling predictions, eqs. (3.22) and (3.23) (broken lines with slopes -1 and -2).

3.2 Zero temperature results

The magnitude of the noise

$$\langle \boldsymbol{\xi}(t) \cdot \boldsymbol{\xi}(t') \rangle = 2k_B T \delta(t - t') \mu_0 \quad (3.12)$$

is proportional to the temperature, which means that it can be neglected in the limit $\tilde{E} \rightarrow \infty$. The rescaled deterministic equation reads

$$\tilde{\mathbf{r}}(\tilde{t} + \tilde{\Delta}) = \tilde{\mathbf{r}}(\tilde{t}) + \sum_{j=0}^M \frac{\mu_{ij}}{\mu_0} \cdot \left[-\nabla_{\tilde{\mathbf{r}}_j} \tilde{U} + 1 \right] \tilde{\Delta}. \quad (3.13)$$

Physically the neglect corresponds to large objects due to the rescaling with the monomer radius a or to very strong fields, e.g. the gravitational force in an ultracentrifuge. But one can also see this as a *stability analysis* to which temperature effects are added later.

3.2.1 Deformation

A measure of the mean chain bending is

$$K = \frac{1}{2} |\hat{\mathbf{r}}_{01} - \hat{\mathbf{r}}_{N-1N}| = \sin(\theta) \quad (3.14)$$

where θ is the bending angle of the terminal chain segment (see fig. 3.1a) and $\hat{\mathbf{r}}_{01} = \mathbf{r}_{01}/r_{01}$. The *orientation parameter* measures the *overall* rod orientation and reads

$$\psi = \frac{3}{2} \left[\frac{\mathbf{R}_e}{R_e} \cdot \frac{\mathbf{E}}{E} \right]^2 - \frac{1}{2} = \frac{3}{2} \sin^2(\alpha) - \frac{1}{2} \quad (3.15)$$

where $\mathbf{R}_e \equiv \mathbf{r}_{N-1} - \mathbf{r}_0$ is the end-to-end vector of the chain, and the orientation angle α is defined in fig. 3.4a. The electric birefringence signal is proportional to the *alignment parameter* [36]

$$\chi = \frac{1}{M} \sum_{i=0}^{M-1} \left\{ \frac{3}{2} \left[\frac{\mathbf{r}_{i+1}}{r_{i+1}} \cdot \frac{\mathbf{E}}{E} \right]^2 - \frac{1}{2} \right\} \quad (3.16)$$

and is a measure of the orientation of the *individual* bonds of the chain.

In this bead model the contour length L could be either the number of monomers N times their diameter or the sum of all $M = N - 1$ bonds. It turns out that the latter gives a much better scaling for short chains so that I set

$$L = 2 M a . \quad (3.17)$$

Throughout this chapter an isotropic elastic material is assumed, i.e. ε and γ are related by eq. (3.6). In the continuum limit, one lets $M \rightarrow \infty$ and $a \rightarrow 0$ while keeping $L = 2Ma$ fixed. To remove the dependence on the a I express the results as a function of

$$\varepsilon^* = \frac{\varepsilon}{qEL^2} = \tilde{\varepsilon} \frac{a^2}{L^2} . \quad (3.18)$$

In stationary motion, the velocities of all parts of the rod have to be same. The external force \mathbf{E} drives all monomers in the same way, but the hydrodynamic thrust coming from the external forces alone, viz. $\sum \mu_{ij} \cdot q\mathbf{E}$, is larger in the middle of the rod than at its ends, as can be seen from eq. (3.13): The middle receives thrust from both sides of neighboring segments. This has to be balanced by elastic force $-\nabla_{\mathbf{r}_j} U$ that then result in a *deformation* of the rod. Fig. 3.1a shows the bending of a 20 subunit chain for different elastic parameters. On the scaling level, the elastic torque of a rod of length L bent by an angle θ is

$$T_\theta \sim \frac{\varepsilon \theta}{L} \quad (3.19)$$

and has to balance the torque that arises from the inhomogeneity of the hydrodynamic thrust acting on the driven rod,

$$T_E \sim \frac{qEL^2}{a} . \quad (3.20)$$

The last relation can be derived as follows: If only the external force and no elastic forces are present the velocity difference $\Delta v(r)$ between the middle monomer and a monomer at a distance r from it scales like $\Delta v(r) \sim \mu_0 qE \ln[L^2/(L^2 - 4r^2)]$ where the Oseen tensor is used. Neglecting the logarithmic term, which is at most of the order $\ln[L/a]$, the monomer at distance r gives a contribution to the hydrodynamic torque, $\Delta T_E(r)$, of $\Delta T_E(r) \sim \Delta v(r) r / \mu_0 \sim qEr$. Adding the torque contributions of all $N \sim L/a$ monomers yields eq. (3.20).

Equating $T_\theta \sim T_E$ gives a stationary bending angle

$$\theta \sim \frac{qEL^3}{a\varepsilon} . \quad (3.21)$$

In fig. 3.1b the numerically determined rescaled chain bending (or mean curvature) K/M^2 (open symbols) and bond alignment $(\chi + 1/2)/M^4$ (closed symbols) are shown as a function of the inverse driving field ε^* . In agreement with the scaling prediction, data in the range of small bending are well described by the laws [153]

$$\theta \approx K = 1.1 \times 10^{-3} qEL^3/a\varepsilon \quad (3.22)$$

$$\theta^2 \approx \chi + 1/2 = 1.1 \times 10^{-6} (qEL^3/a\varepsilon)^2 , \quad (3.23)$$

except for logarithmic corrections. It is seen that the numerical prefactors deviate largely from unity, which makes the simulation necessary.

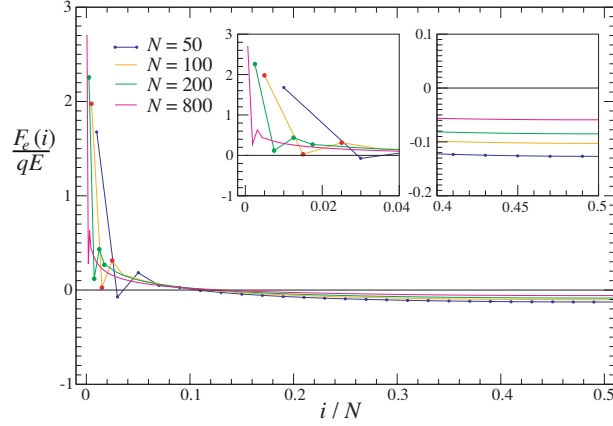


Figure 3.2: Distribution of elastic forces $F_e(i)$ along a chain moving parallel to external field E obtained from eqs. (3.25) and (3.26). The insets are blow-ups of the end and the middle part.

In principle, the hydrodynamic thrust from the elastic forces, $-\sum \mu_{iJ} \cdot \nabla_{\mathbf{r}_j} U$, should also be included in T_E . But for small bending, i.e. large elastic moduli, the elastic forces F_e are just proportional to E and independent of ε : From eq. (3.3) and using $\vartheta_i \propto 1/\varepsilon$ we find

$$F_e \propto \varepsilon \vartheta_i \propto \varepsilon/\varepsilon. \quad (3.24)$$

ϑ_i is the typical bending angle of two adjacent segments. Thus at the scaling level, eq. (3.20) is still valid.

The independence of the elastic forces of ε also justifies the use of bead models for the treatment of rigid bodies since the limit $\varepsilon \rightarrow \infty$ can safely be taken. How are - in this limit - the elastic forces $F_e(i)$ (with i the monomer number) distributed along the chain, when it is sedimenting as in fig. 3.1a ? One has to solve the following linear set of equations

$$\sum_{j=0}^N \mu_{ij} [F_e(j) + qE] = v_z \quad (3.25)$$

$$\sum_{i=0}^N F_e(i) = 0 \quad (3.26)$$

for the $N + 1$ unknowns $F_e(i)$ and v_z . $F_e(i)$ and E point in z -direction; the velocities of all beads v_z are the same. Simulations of course would do the same but are less efficient. The result is shown in fig. 3.2 for long chains $N \geq 50$. One can see that elastic forces are mainly distributed at the end of the chain, which is expected from the analysis before. In the limit $N \rightarrow \infty$ the rod becomes infinitely thin and its velocity diverges logarithmically [172]. Therefore, not all features of the continuum limit can be obtained within this bead model.

3.2.2 Orientation

As explained above, the reduction of symmetry by deformation can lead to an orientation of the rod. Fig. 3.3 illustrates this mechanism. A stiff cylinder experiences no orientational torque (a). For longitudinal (b) and transverse (c) deformation modes the orientational

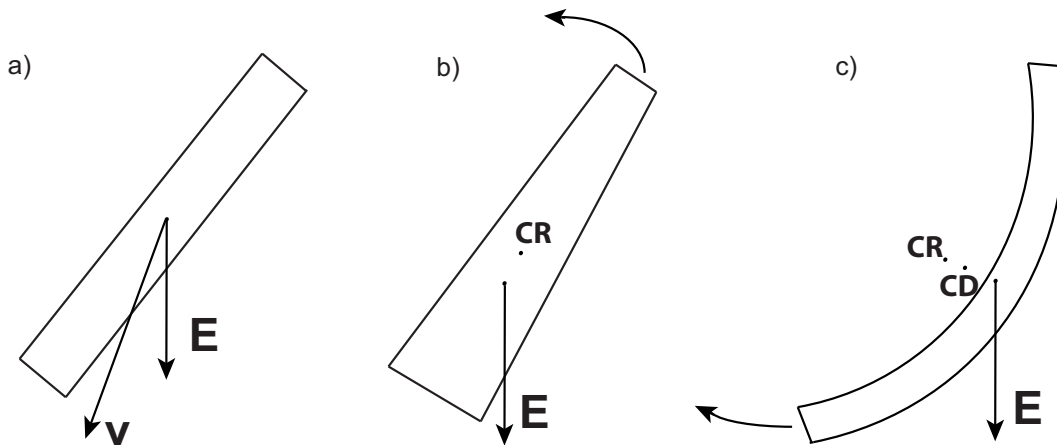


Figure 3.3: Schematic drawing of three deformation modes and their respective orientational tendency. a) Cylinder: no orientation but sideward motion. b) Stretched rod at one end: coupling tensor ζ_R^{tr} might vanish at center of reaction (CR); but mean force applies at a different point (center of mass / charge). c) Bent rod: ζ_R^{tr} is always non-zero. Also shown the center of diffusion (CD), see appendix.

tendency is parallel and perpendicular, respectively. For isotropic elastic media only the second is relevant. The dashed line in fig. 3.4a gives the time evolution of $\chi \approx \psi$ of a 20-bead initially nearly parallelly oriented rod ($\psi(0) = 0.9995$) that turns thereby adjusting its deformation (see snapshots). The solid lines include noise and are discussed later. The deformation represented by the mean curvature K relaxes much faster than the orientation, ψ and χ , as can be seen in fig. 3.4b: K approaches its constant value in about $\tilde{t} \sim 10$ while the orientation is completed in $\tilde{t} \sim 100$. This time scale separation makes it possible to treat the rod as semi-rigid.

3.3 Full temperature results

After the general features of this hydrodynamic orientation have been laid down, I now want to present the main results of this chapter, which of course have to take temperature into account. The rescaled temperature will be denoted by $1/\tilde{E}$, since in experiments the temperature is usually given, while the field E can be varied.

3.3.1 Stationary motion

For finite temperature the orientation is not complete and subject to thermal fluctuations. If the orientation angle α defined in fig. 3.4 is small enough the orientating torque is proportional to α , the bending angle θ and the driving torque

$$T_\alpha \sim \alpha \theta T_E . \quad (3.27)$$

For *low temperatures* and therefore small fluctuations, the average orientational energy αT_α equals thermal energy,

$$\alpha T_\alpha \sim k_B T . \quad (3.28)$$

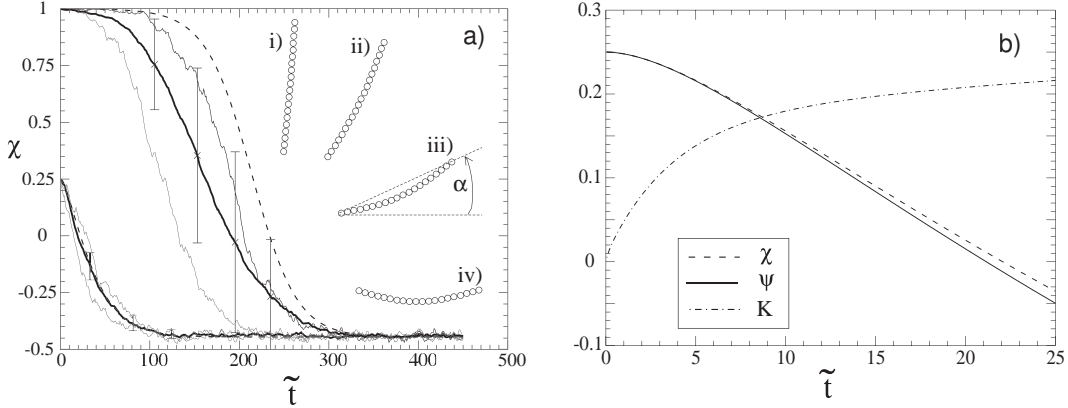


Figure 3.4: Dynamic orientation of an isotropic elastic rod. Driving field is turned on at time $\tilde{t} = t\mu_0qE/a = 0$ and turned off at $\tilde{t} = 450$. a) Time evolution of the alignment parameter χ of a chain with bending modulus $\tilde{\epsilon}a/L = 10.5$ and length $M = 19$ with initial orientation $\chi = 0.25$ and $\chi = 0.9995$. The dashed line is at zero temperature $\tilde{E} = \infty$ while solid lines are for $\tilde{E} = 20$. Thin solid lines are single trajectories while thick solid lines are averages over 10 individual runs. Snapshots are obtained for $\tilde{E} = \infty$ and initial orientation $\psi = 0.9995$ for times i) $\tilde{t} = 90$, ii) 180, iii) 260, and iv) 400. b) Same data as in a) for $\tilde{E} = \infty$ and initially $\chi = \psi = 0.25$ (corresponding to an angle $\alpha = 45^\circ$). Shown are the curvature K , alignment χ and orientation ψ .

Solving eqs. (3.27) and (3.28) for α^2 gives a mean-square orientational fluctuation of

$$\frac{2}{3}(\psi + 1/2) \simeq \langle \alpha^2 \rangle = 6.1 \times 10^3 \left(\frac{k_B T}{qEa} \right)^2 \frac{a^4 \ell_P}{L^5} \quad (3.29)$$

where eq. (3.5) has been used. The prefactor is determined numerically in fig. 3.5 for a fixed rigidity $\tilde{\epsilon}a/L = \ell_P/L = 100$.

Within linear-response theory, the orientational fluctuations are governed by a quadratic form proportional to the coupling constant J , yielding the expectation value

$$\langle \sin^2 \alpha \rangle = -\frac{\partial}{\partial (J/2)} \ln \left[\int_{-\pi/2}^{\pi/2} d\alpha \cos \alpha e^{-(J/2) \sin^2 \alpha} \right]. \quad (3.30)$$

For low temperatures (high J -values) one can extend the integration boundaries to infinity and compute the Gaussian integral to obtain

$$\langle \alpha^2 \rangle \simeq \langle \sin^2 \alpha \rangle = 1/J, \quad (3.31)$$

which together with eq. (3.29) fixes the coupling constant J .

In the *high-temperature* regime (small J), the rod orientation distribution is almost isotropic. Expanding the exponential eq. (3.30) gives

$$\langle \sin^2 \alpha \rangle \simeq 1/3 - 2J/45 + \mathcal{O}(J^2), \quad (3.32)$$

from which with the definition of ψ , eq. (3.15), the final result is obtained [153]

$$\psi \simeq -J/15 = -1.1 \times 10^{-5} \left(\frac{qEa}{k_B T} \right)^2 \frac{L^5}{\ell_P a^4}. \quad (3.33)$$

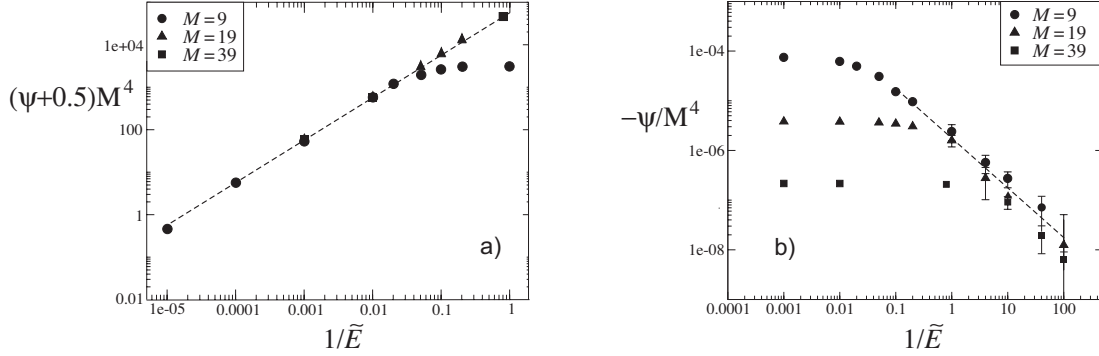


Figure 3.5: a) Rescaled orientational parameter $(\psi+0.5)M^4$ as a function of the rescaled temperature $k_B T/(qEa) = 1/\tilde{E}$ for fixed rigidity $\tilde{\varepsilon} a/L = 100$ in agreement with the low-temperature scaling prediction eq. (3.29) (broken line). b) Same data plotted as $-\psi/M^4$ compared with the high-temperature scaling prediction eq. (3.33).

This scaling law including the numerical prefactor is confirmed in fig. 3.5b (broken line). It is the limit most relevant for experiments. Note that the solvent viscosity only enters the rescaled time scale $\tilde{\Delta}$ and thus does not influence the stationary behavior.

3.3.2 Dynamics

In transient electric birefringent experiments (TEB) [48] the time dependence of the orientational response is measured after the electric driving field is suddenly turned on or off. Coming back to fig. 3.4a, the time evolution of the alignment parameter χ for zero and finite temperature (broken and solid lines, respectively) is displayed for two different initial orientations. For finite temperature averages (thick lines) over 10 individual trajectories (thin lines) are shown. The hydrodynamic response time is roughly of the order of $\tilde{\tau}_{HD} = \tau_{HD}\mu_0 qE/a \sim 100$. In fig. 3.6a the alignment parameter χ of an isotropic ensemble of 150 chains is shown for a few different rescaled temperatures. The orientational response for $\tilde{E} = 1$ (top curve) is fitted to a pure exponential $\chi(t) = -0.38 [1 - \exp(-\tilde{t}/\tilde{\tau}_{HD})]$ (broken line) with the response time $\tilde{\tau}_{HD} = 62.2$. It can also be seen that there is no significant dependence of the initial decay rate on temperature. The response after the field is turned off is fitted to $\chi(t) = -0.447 \exp(-[\tilde{t} - 450]/\tilde{\tau}_D)$ where the orientational diffusion time $\tilde{\tau}_D = \tau_D qE\mu_0/a = 218$ is given by the perturbative expression for the rotational diffusion constant of a rigid cylinder [172]

$$D = \frac{1}{6\tau_D} = \frac{18k_B T \mu_0 a}{L^3} \left[\ln \frac{L}{2a} - 0.662 + 0.917 \frac{2a}{L} - 0.05 \left(\frac{2a}{L} \right)^2 \right]. \quad (3.34)$$

On the scaling level, the decay of the orientation angle α in an applied electric field is governed by the differential equation

$$\dot{\alpha} \sim -D T_\alpha / k_B T \quad (3.35)$$

where $T_\alpha \sim \alpha \theta T_E$ is the aforementioned orientational torque. The hydrodynamic orientation time can be read off to be

$$\tau_{HD} \sim \frac{k_B T}{D \theta T_E} \sim \frac{a \varepsilon}{\mu_0 q^2 E^2 L^2}. \quad (3.36)$$

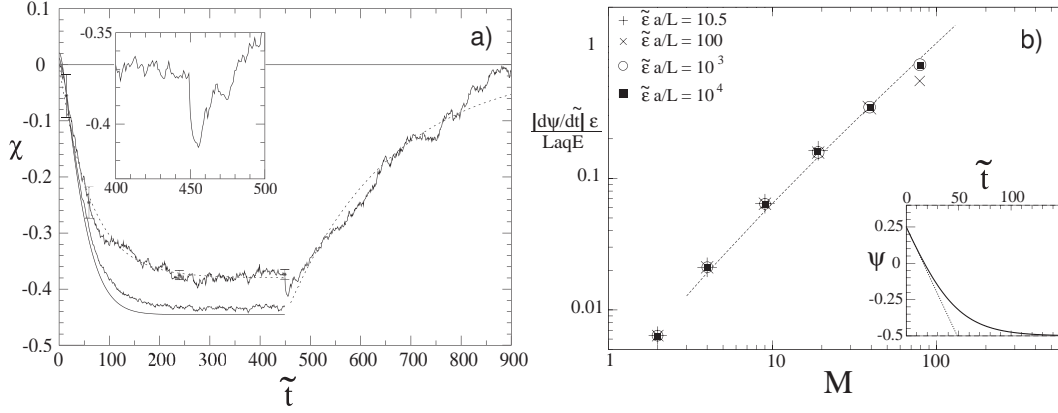


Figure 3.6: a) Time evolution of the alignment parameter χ for an ensemble of 150 rods with initially isotropic distribution for $\tilde{\epsilon}a/L = 10.5$, $M = 19$ and different rescaled fields (increasing from top to bottom) $\tilde{E} = 1, 5, \infty$. For $\tilde{t} > 450$ and in the inset only the data for $\tilde{E} = 1$ are shown, exhibiting an over-shoot right after turning off the field. The dashed lines are exponential fits. b) Rescaled orientational speed $|\dot{\psi}|$ for initially $\alpha = 45^\circ$ as function of chain length M for fixed $\tilde{E} = \infty$ and various bending moduli. The dashed line is a fit $a_0 M \ln[a_1 M]$ with the parameters $a_0 = 0.00183$ and $a_1 = 3.45$. The inset shows same data for ψ as in fig. 3.4b (solid line) for $M = 19$ and $\tilde{\epsilon}a/L = 10.5$. $|\dot{\psi}|$ is obtained from this curve as the intermediate-time slope (dotted line) which is given by $\psi(t) \simeq 0.25 - 0.0154\tilde{t}$.

In fig. 3.6b, the orientational speed $\dot{\psi}$ for various bending rigidities is determined at zero temperature, for the ease of calculation. The numerical data exhibit pronounced logarithmic corrections, which are missed by the scaling analysis, and can be fitted to (broken line)

$$\tau_{HD} = \frac{820}{\ln[1.725L/a]} \frac{a\epsilon}{\mu_0 q^2 E^2 L^2}. \quad (3.37)$$

For the ratio of the diffusional relaxation and hydrodynamic orientation time scales one obtains the relation

$$\frac{\tau_D}{\tau_{HD}} = 1.1 \times 10^{-5} \frac{L^5 q^2 E^2}{a^2 \epsilon k_B T}. \quad (3.38)$$

The strong length dependence makes the orientational process much faster for long rods, in agreement with experiments [136]. For charged rod-like objects the hydrodynamic orientation mechanism competes with the *counterion polarization mechanism* which favors parallel orientation. The orienting polarization torque is

$$T_\alpha^P \sim \alpha \epsilon_0 E^2 L^3 \quad (3.39)$$

where ϵ_0 is the dielectric constant (shifting the dispute about the L -dependence of the polarizability [190] to chapter 7). The characteristic orientation time due to electric polarization, τ_P , follows from the same differential equation as eq. (3.35),

$$\tau_P \sim \frac{k_B T}{D} \frac{\alpha}{T_\alpha^P} \sim \frac{1}{\mu_0 a \epsilon_0 E^2}, \quad (3.40)$$

and thus is independent of the length. For long polymers one has

$$\tau_D > \tau_P > \tau_{HD}. \quad (3.41)$$

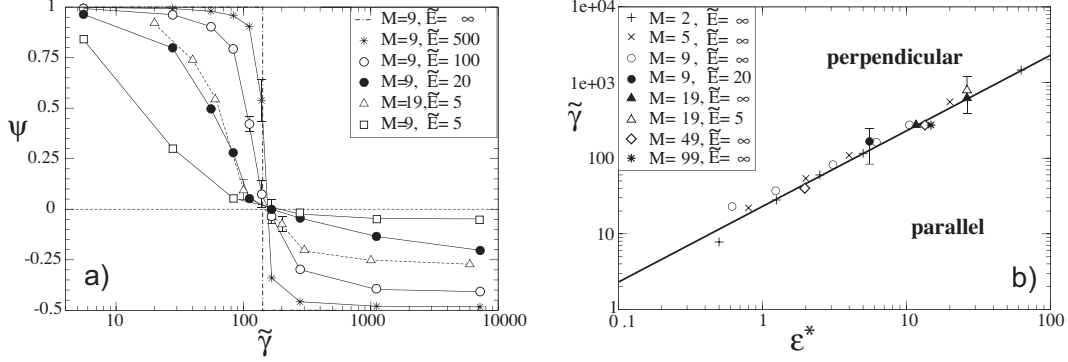


Figure 3.7: a) Orientation parameter ψ of an *anisotropic* elastic chain as a function of the rescaled stretching modulus $\tilde{\gamma} = \gamma/(qE)$ for various rescaled inverse temperatures $\tilde{E} = qEa/(k_B T)$ and chain lengths. The rescaled bending modulus $\varepsilon^* = \varepsilon/(L^2 qE) = 5.56$ is kept constant. b) Phase diagram of chain orientation as a function of the rescaled bending modulus ε^* and stretching modulus $\tilde{\gamma}$ for various lengths and temperatures. The solid line is given by eq. (3.46).

The hydrodynamically induced anomalous birefringence is the fastest process of all. Interestingly, the overshoot of the signal in fig. 3.6a after the electric field is turned off is commonly seen in experiments [94, 136]. It is caused in the simulations by a quick straightening of the bent and perpendicularly oriented chain after the strain field disappears [36]. This would also explain why AC fields tend to yield larger anomalous birefringence signals [136].

3.4 Anisotropic materials

So far it was always assumed that both elastic parameters, γ and ε , are related by $\varepsilon/\gamma = a^2/4$. It is interesting to explore also anisotropic materials which, in the simplest case, are described by two parameters. As anticipated in fig. 3.3, for very stretchable rods parallel orientation is obtained; one can therefore expect that a transition between these two orientational tendencies occurs at a certain ratio of γ and ε .

In the limit of zero temperature, i.e. $\tilde{E} = \infty$, the only parameters are $\tilde{\gamma}$, $\tilde{\varepsilon}$ and L/a . In the continuum limit one expects scaling relations to become independent of the chain radius a , and the proper scaling variables are $\tilde{\gamma}$ and $\varepsilon^* = \tilde{\varepsilon}a^2/L^2$. Fig. 3.7a displays the chain orientational parameter ψ as a function of $\tilde{\gamma}$ for fixed $\varepsilon^* = 5.56$ at various temperatures. Indeed, ψ changes sign at a constant value of $\tilde{\gamma}$. In the linear-response regime the location of the transition should be independent of the driving field strength. This suggests a linear dependence $\tilde{\gamma} \sim \varepsilon^*$.

Fig. 3.7b shows the transition $\tilde{\gamma}(\varepsilon^*)$ for various chain lengths with and without temperature. Even a 3-bead chain is already close to the continuum value $M \rightarrow \infty$ if the definition $L = 2Ma$ is taken. For this reason, the transition line in this “phase diagram” is determined analytically for three spheres in a perturbative way up to $\mathcal{O}(E^2)$:

Expanding the positions of the centers of the three spheres $i = 1, 2, 3$

$$\mathbf{r}_i = \mathbf{r}_i^{(0)} + \mathbf{r}_i^{(1)} + \mathbf{r}_i^{(2)} + \mathcal{O}(E^3) \quad (3.42)$$

and inserting them into the forces and the mobility tensor

$$\mathbf{F}_i = \mathbf{F}_i^{(1)} + \mathbf{F}_i^{(2)} + \mathcal{O}(E^3) \quad (3.43)$$

$$\mu_{ij} = \mu_{ij}^{(0)} + \mu_{ij}^{(1)} + \mathcal{O}(E^2) \quad (3.44)$$

gives

$$\sum_j \left[\mu_{ij}^{(0)} \cdot \mathbf{F}_j^{(1)} + \mu_{ij}^{(0)} \cdot \mathbf{F}_j^{(2)} + \mu_{ij}^{(1)} \cdot \mathbf{F}_j^{(1)} \right] + \mathcal{O}(E^3) = \mathbf{v} + \mathbf{v}_i^{rot} . \quad (3.45)$$

\mathbf{v} is the common translational velocity, \mathbf{v}_i^{rot} the rigid body rotation. The zeroth order of the forces, of course, vanishes in equilibrium. From the condition $\mathbf{v}_i^{rot} = 0$ it follows that

$$\tilde{\gamma} \approx 23.44 \varepsilon^* . \quad (3.46)$$

The calculation is presented in appendix B.2. The result eq. (3.46) is shown in fig. 3.7b as a solid line and gives a good fit also for $M \gg 1$.

For isotropic rods the relation

$$\tilde{\gamma} = 16 \left(\frac{L}{2a} \right)^2 \varepsilon^* \quad (3.47)$$

holds, so that for aspect ratios $L/(2a)$ slightly greater than one the rods are always in the perpendicular phase. In a sense, this also justifies the use of the (unstretchable) Kratky-Porod chain [83] for semiflexible biopolymers: Even though most of these polymers are approximately isotropic elastic (see e.g. [165] for DNA) and the inextensibility constraint ($\gamma \rightarrow \infty$) cannot be assumed from the beginning, the above analysis shows that for long chains the bending modes are responsible for hydrodynamic orientation and stretching can safely be neglected.

3.5 Discussion

All our results are valid only for low Reynolds numbers. Orientation of cylindrical objects at high Reynolds numbers is also possible, for example by streaming of the fluid along the surface of the body [90]. Is the hydrodynamic orientation mechanism discussed in this paper compatible with the low-Reynolds number assumption? Consider a cylinder of length L moving at velocity v . Its velocity scales as $u \sim F/(\eta L)$ where the total force F is given by $F \sim qEL$. The condition $Re \equiv \rho L v / \eta \ll 1$ is equivalent to

$$\frac{L}{a} \frac{qEa}{k_B T} \sim N \tilde{E} \ll \frac{\eta^2}{\rho k_B T} \approx 10^{11}, \quad (3.48)$$

where the density and viscosity of water is used. The requirement is easily fulfilled, and the model is thus consistent.

3.5.1 Hydrodynamic orientation in the literature

Hydrodynamic effects as a possible source for birefringence were considered already nearly hundred years ago for vanadium oxide sols [49]. It received some attention in the context of birefringence experiments on TMV [66, 93, 130], but explanations were based only on vague statements: Heller [66] gives a survey over possible hydrodynamic orientation mechanisms from “electrophoretic orientation” to turbulence. O’Konski and Zimm [130], and O’Konski and Haltner [132] discard hydrodynamic orientation on the basis of the cylindrical symmetry assumed for TMV particles. Like Kobayasi [79], they mention “perpendicular hydrodynamic orientation” without reference to any theory. It might therefore be just an experimental fact. Later O’Konski and Krause [133] try to support it by a two-dumbbell model but their reasoning is wrong. Finally, Grossman and Soane [62] regard it as an high-Reynolds number effect which is negligible. Interestingly, they cite [63] for this statement. It seemed therefore worthwhile to clarify this issue within a simple bead model.

Elvingson [36, 37] performed Brownian dynamics simulations including hydrodynamic effects and bending elasticity. Although it can be concluded indirectly from his results, that his chains get sometimes hydrodynamically oriented perpendicular to the field, $\psi < 0$, he only discusses bond orientation, i.e. the effects on χ (cf. eq. (3.16)), but not the orientation of the polymer as a whole. Only for rigid rods these two parameters coincide; otherwise a non-zero χ is a combined effect of an orientation ψ and a deformation. The former is a second order, the latter a first order effect in E and therefore more important for small fields. Nevertheless, one can only speak of a *coupling between hydrodynamics and elasticity* if one also examines how this hydrodynamically induced deformation in return leads to a hydrodynamic orientation.

Several authors investigated the orientation of kinked rods or arc-shaped molecules as models for short DNA [13, 141, 181] based on the hydrodynamical coupling between translational and rotational motion [63]. The thermal average of the bending angle of the semiflexible chain is used as input for the *rigid* angle. Bertolotto et al. [14] calculated the birefringence as a function of the bending angle θ and then integrated over a distribution of θ which was obtained by solving the Focker-Planck equation of θ of a hinged bent rod. This elastic rod consisted of two rigid arms with an harmonic elastic potential, which had its minimum at $\theta = \pi$. The influence of the orientation on the deformation θ was neglected.

3.5.2 Comparison with experiments

Experimental situations where this hydrodynamic orientation can be observed as well as already existing evidence is now be presented.

fd-virus

Fd-viruses are semiflexible particles having a length of $L \approx 880$ nm, a diameter of $2a \approx 9$ nm [125] and a persistence length of $\ell_P \approx 2200$ nm [31]. The total net charge is roughly $500 e^-$ so that the charge per length $2a$ is about $q = 5$ [81]. For a typical electric field of $E = 10^5$ V/m the rescaled field strength $\tilde{E} = aqE/k_B T$ is $\tilde{E} \approx 0.1$. Eq. (3.33) gives $\psi \approx 60$ meaning that complete perpendicular orientation should occur were there not electrostatic effects. Solutions of fd-virus show anomalous birefringence in certain situations [69, 82]. This will be discussed in chapter 7.

For the sedimentation case, the reduced driving field acting on the monomers is

$$\tilde{E} \simeq \frac{4\pi a^4 \rho g G}{3 k_B T} \quad (3.49)$$

where $G = 9.81$ m/s² is the gravitational acceleration, g is the g-factor of a centrifuge, and $\rho \approx 10^3$ kg/m³ is the density difference between the sedimenting particle and the solvent. For the parameters of the fd-virus one gets $\tilde{E} \simeq 10^{-8}g$. To obtain $\psi \simeq 1$, one would need a g-factor of $g \approx 10^6$ which is large but can still be reached in an ultracentrifuge without much effort.

Tobacco mosaic virus

The tobacco mosaic virus (TMV) is a rod-shaped macromolecule with a length of $L \approx 300$ nm and a diameter of $2a \approx 15$ nm [48]. The length is calculated from a rotational diffusion constant $D_r = 333$ s⁻¹ [131] using Broersma's cylindrical rod model [20]

$$D_r^{\text{Br}} = \frac{3k_B T}{\pi \eta L^3} \left[-1.57 + \ln(L/a) + 7 \left(\frac{1}{\ln(L/a)} - 0.28 \right)^2 \right], \quad (3.50)$$

or from direct electron microscope observations. Its persistence length is at least $\ell_P > 10 L$ [47]. At slightly alkaline pH TMV has a charge of approximately $-6000e$ [132] some of which might be compensated by close counterions. The hydrodynamic orientation is much weaker due the smaller aspect ratio and larger persistence length, but might still be measurable: Assuming the same reduced charge density as for the fd-virus and $\ell_p = 10 L$ one still finds $\psi \simeq 0.1$. Positive electric birefringence signals of dilute TMV solutions are usually attributed to an orientation of the stiff macromolecule parallel to the applied electric field (this can be checked by flow birefringence), while negative birefringence seems to be a low-field effect [5, 130]. O'Konski et al. [130, 132] favor induced dipole moments caused by polarization of the counterions adjacent to the macromolecule as orientation mechanism. While this mechanism certainly plays the dominant role one can still ask for the orientation caused by hydrodynamic forces.

f-actin

One of the best candidates for hydrodynamic orientation is possibly f-actin. It is a semiflexible polymer with a variable length of up to $L \approx 10 \mu\text{m}$, a diameter of $2a \approx 8 \text{ nm}$ and a persistence length of $\ell_P \approx 17.7 \mu\text{m}$ [57]. Eq. (3.33) shows that for $L = 10 \mu\text{m}$ filaments g-factors of less than 10^5 are sufficient to achieve $\psi \simeq 1$. Kobayasi et al. [78, 79] measured negative birefringence of in electric fields as well during ultracentrifugation. The latter might provide an unambiguous demonstration of the above effect. Unfortunately, the experiment was done already more than forty years ago and has not been reproduced later. It should be noted that Dr. M. Claessens (TU München) plans to perform an ultracentrifugation experiment with a dilute solution of actin so that this issue might be clarified soon.

Short DNA

Antosiewicz and Porschke [4] reported an amplitude inversion in the electric dichroism decay of 179 to 256 bp DNA strands at small field strengths. It was subsequently explained either with an apparent permanent dipole moment perpendicular to the long axis of the chain which should be caused by bending [4, 12] or with an hydrodynamic orientation mechanism [14, 36, 141]. Using $L = 60 \text{ nm}$ (179 bp), $2a = 2 \text{ nm}$, $\ell_P = 50 \text{ nm}$ and a pulsed electric field with amplitude $E = 10^6 \text{ V/m}$, eq. (3.33) gives $\psi \simeq 30$; for $L = 20 \text{ nm}$ chains one still gets $\psi \simeq 0.1$ showing that the presented mechanism is of great relevance.

Neutral rods

Neutral boehmite rods have the great advantages that investigations are not complicated by charge effects, and that its lengths can be varied. Buitenhuis and Philipse [21] studied sedimenting rods of length $L \approx 250 \text{ nm}$ and diameter $2a \approx 9 \text{ nm}$ in dilute solution. Centrifuged with $g \approx 800$ the sediments show domains in which the rods are aligned perpendicular to the sedimentation velocity. Assuming $\ell_P = 10L$ one finds $\psi \sim 10^{-9}$ for this small g . Thermal wash-out represses the above orientation mechanism. It is more likely that interactions with the wall cause the observed orientation different from an earlier expectation [153]. Nevertheless, for larger particles and higher g-factors boehmite rods should be a promising model system.

Chapter 4

Driven Rotation of a Semiflexible Filament

The last chapter provided a very simple example of the coupling between hydrodynamics and flexibility. The following example is similar in spirit and of great importance for propulsion at the nano- and micrometer scale. Here some external torque is applied to the base of an end-grafted elastic filament, and the resulting angular velocity is determined as a function of this torque and the elastic parameters. Different approximations to describe the hydrodynamic interactions are checked. Allowing the filament to move, the translational velocity caused by this rotation and the propulsion efficiency is calculated. The inclusion of flexibility leads to the noteworthy result that forward motion is achieved irrespective of the sense of rotation, different from rigid rods (where no net propulsion results) or helices (which move according to their sense of rotation).

The main idea and many of the results are presented in [105, 106]. Nonetheless, this chapter differs from our publication in two respects: Firstly, I concentrate on the large-force regime in which the external torque $M \gg k_B T$. This is indeed the case for most bacterial motors [96]. One can therefore neglect temperature effects as done in section 3.2, which not only speeds up the simulation considerably but also states the problem more clearly. Secondly, the dependence of the propulsion on elasticity will be investigated to a broader extend.

The first section gives an introduction into the mathematical modeling and the biological background of bacterial motility in order to motivate the investigation and places it within the field. The second one deals with the deformation of the rod while the last one comes back to the main topic of propulsion with this rotating rod.

4.1 Modeling bacterial motility

Propulsion at low Reynolds number is essentially different from the one we are used to at high Reynolds number since inertia effects do not play a role [24, 95, 145]. For objects at the scale of $1 \mu\text{m}$ or less and typical swimming speeds in water Stokes flow dynamics is a very good approximation. This means that propulsion based on inertia, as well-known from the ordinary macroscopic world, is hopelessly inefficient: Moving an oar slowly forward and quickly backward will not generate a forward thrust [145]. The dynamics are governed by a first-order differential equation in time that is symmetric with respect to time reversal, and therefore moving an appendix back and forth the same path even with different velocities

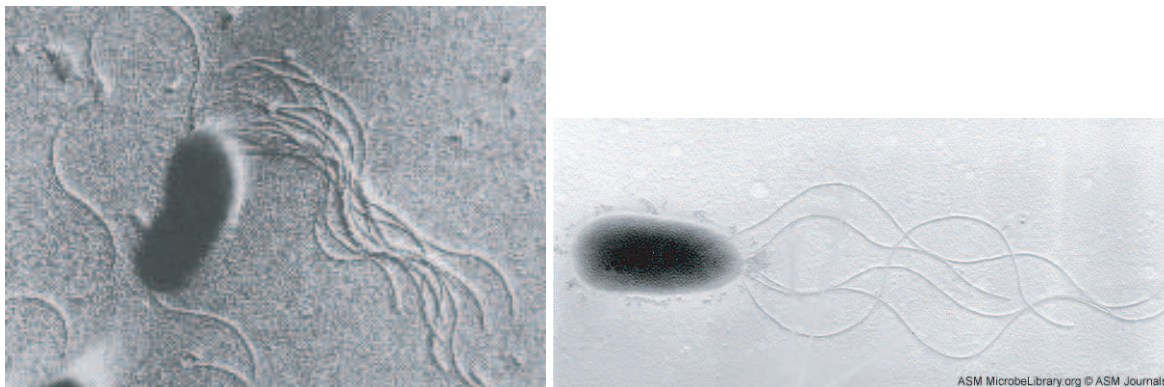


Figure 4.1: Left picture: Transmission electron micrograph showing bundling of the flagella of a *E. coli* bacterium during chemotaxis. Right picture: *Pseudomonas putida* bacterium with six flagella. Taken from the ASM Microbe Library (www.microbelibrary.org).

renders the self-propelled object at its original point after one cycle. Different mechanisms are required for Stokesian swimmers, among them the beating of rod-like cilia and the rotation of helical flagella.

Lighthill [96] gives an overview of the vast variety of microorganisms with flagella. One can classify them into eukaryotic and prokaryotic organisms; and skimming over many details one may say that there are two major kinds of microorganisms with flagella, (eukaryotic) sperms and (prokaryotic) bacteria. The former have one flagellum, with $\sim 0.25 \mu\text{m}$ diameter in the case of the sea urchin sperm, consisting of the axoneme (the core of the flagellum) enclosed by an extension of the cell membrane. The cross-section of the axoneme has the so-called “9+2” pattern of nine doublets of microtubules along the outer circle and two single microtubules in the center. It seems now very clear that these microtubules can slide along each other so that the flagellum can be *actively bent* by the sperm thereby propagating a wave along the flagellum [96].

Bacteria - here I concentrate on *Escherichia coli* (*E. coli*) - are usually much smaller with a cell body of $\mathcal{O}(1 \mu\text{m})$ and one or several flagella. The flagella are semiflexible intrinsically bent helical filaments with a diameter of $\sim 20 \text{ nm}$ and a length of $\mathcal{O}(10 \mu\text{m})$ [76] each of which is driven by a rotary motor [10]. The motor turns at roughly 100 Hz. When rotated counter-clockwise the flagella form a bundle, and the bacterium moves, while clockwise rotation causes the bacterium to “tumble” resulting in a random change of the direction of motion, which is essential for chemotaxis. The flagella are thus *passively bent* by the motion through the viscous fluid while driven at one end. This chapter is motivated by the study of bacterial flagella, as well as by nano-motors that mimic bacterial propulsion.

Earlier investigations of propulsion at low Reynolds number [95] mostly concentrated on the motion of *rigid* objects for their easier analytical tractability. Often, the flagellum is replaced by a slender, i.e. one-dimensional, object such that it can be represented by a line of Stokeslets [98], which is just another name for the Green’s function of the Stokes equation and the Oseen tensor. Distribution of Stokeslets not on the centerline but on the surface of the flagellum is in general an unsurmountable task [143]. Resistive-force theory [61] replaces the long-ranged hydrodynamic interactions by local friction coefficients that differ in tangential and normal direction along the slender body. These coefficients are obtained by cutting the

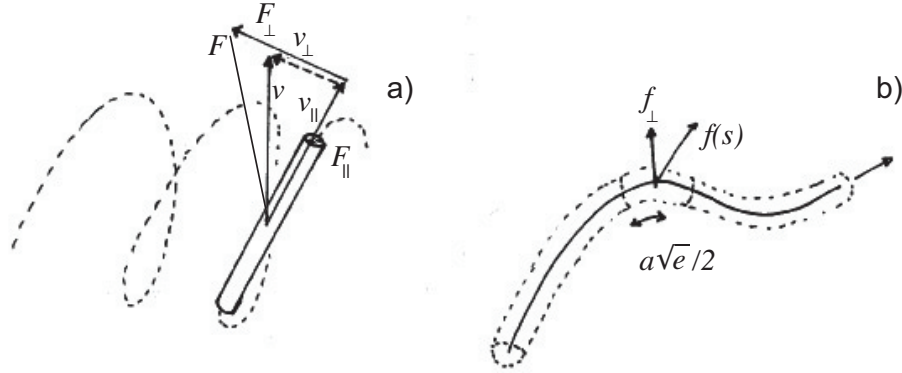


Figure 4.2: a) Illustration of the resistive-force theory for a rotating helix. The cylindrical segment moves with velocity v in tangential direction to axis of rotation. The components of v and the frictional force on the segment F parallel and perpendicular to the cylinder axis are shown. The larger friction coefficient in perpendicular direction results in an increased component F_{\perp} . Integration over all cylinder segments of the helix gives a frictional force on the fluid acting to the left, or vice versa a thrust on the helix to the right. b) Flagellum (dashed lines) and its centerline (solid line) in the slender-body theory. The given forces per length $f(s)$ that originally act on the surface of the flagellum are placed on the centerline. In the near region the flagellum is approximately straight and only the component f_{\perp} influences the fluid velocity $\mathbf{u}(s)$.

flagellum into cylindrical segments. Some arbitrariness is involved in how long these cylinders should be although some optimal choice has been proposed [95]. Resistive-force theory gives an intuitive explanation how propulsion can work at low Reynolds number: When e.g. a helix is rotated by a bacterial motor the cylindrical segments are inclined with respect to their local motion leading to a thrust along the rotational axis (see fig. 4.2a).

To incorporate hydrodynamic interactions Lighthill [96] splits the flagellum into a near and a far region to obtain the fluid velocity at a point $\mathbf{r}(s)$ along the centerline (with arc length s) for a given force per length distribution $\mathbf{f}(s)$

$$\mathbf{u}(s) \approx \frac{\mathbf{f}_{\perp}(s)}{4\pi\eta} + \int_{|\mathbf{r}(s)-\mathbf{r}(s')|>a\sqrt{e}/2} H(|\mathbf{r}(s)-\mathbf{r}(s')|) \cdot \mathbf{f}(s') ds \quad (4.1)$$

where \mathbf{f}_{\perp} is the normal component of the force, a is the radius of the flagellum and e is Euler's number. This approach is often called slender-body theory and valid in the limit of long flagella neglecting end effects. The actual calculation proceeds as follows: A rigid slender body is moved with a prescribed velocity. This gives the frictional forces on the surface of the flagellum. After angular averaging the force per length $\mathbf{f}(s)$ is obtained which is used as input for eq. (4.1). For slender bodies the fluid velocity at the surface of the flagellum for a given s is nearly independent of the position on the circumference. It can thus be represented by the fictitious velocity at the centerline $\mathbf{u}(s)$. Slender-body theory differs from bead models [53] mainly by the diagonal term and the cutoff distance $a\sqrt{e}/2$. A realistic theory must include the cell body which not only provides a frictional center for the translational and rotational flow but also balances the torque of the rotating flagellum by counter-rotation [67].

Bacterial flagella are by far not rigid and undergo a series of shape transformations [173]. Flagellar bundling has been investigated in numerous articles [45, 77, 142]; nonetheless no

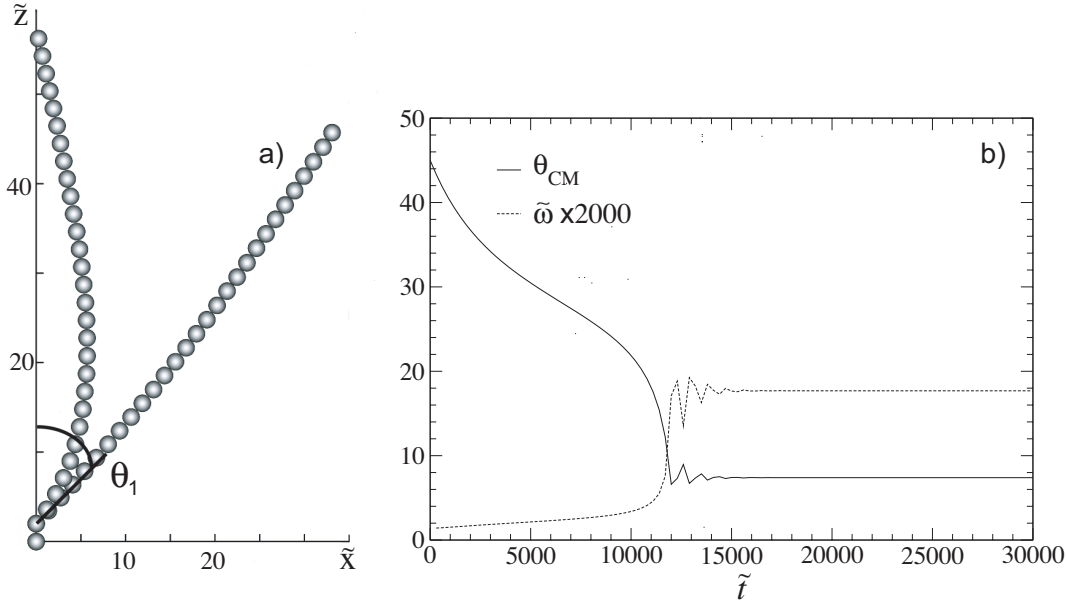


Figure 4.3: a) Sketch of the filament before ($1/\varepsilon^* = 0.3$, right) and after ($1/\varepsilon^* = 0.45$, left) the shape transition for case A. The tilt angle θ_1 is included. Note that the configuration is in 3D with the right filament pointing out of the x - z -plane. b) Evolution of the center-of-mass angle θ_{CM} and angular velocity ω (multiplied by 2000) with time for $1/\varepsilon^* = 0.39$ and case A. At $\tilde{t} \approx 12000$, θ_{CM} decreases dramatically, and as a result of the reduced moment of inertia $\tilde{\omega}$ jumps up.

work has yet been attempted to tackle the full problem including long-ranged hydrodynamics, several flagella, elasticity and torsion in a direct and simple way [45]. As a first step that deserves interest not only for its application in bacteria propulsion one can look at an elastic filament rotated at one end [183, 187], which will be the subject of this chapter.

4.2 Shape transition of the rotating rod

An elastic rod is studied that is driven at its base by some external torque generated by a microscopic motor. As in the previous chapter the filament is described by a bead model whose time evolution is given by a Langevin equation. An isotropic elastic medium is assumed, eq. (3.6). The elastic energy is given by eq. (3.3), except that for the angle at the second sphere from the base θ_1 a fixed tilt angle of 45° is taken, yielding a term of

$$\frac{\varepsilon}{2a} [1 - \cos(\theta_1 - 45^\circ)] \quad (4.2)$$

in U (see fig. 4.3). Twist and torsional degrees of freedom are omitted. A constant external torque $\mathbf{M} = M \hat{e}_z$ is applied to monomer 2 (third from the bottom) which is generated by a force

$$\mathbf{F}_2^{\text{ext}} = \frac{\mathbf{M} \times \mathbf{r}_{12}}{r_{12}^2}. \quad (4.3)$$

Again hydrodynamic interactions are treated on the Rotne-Prager level, and monomers are numbered from 0 to $N-1$. Except for fig. 4.5, thermal noise is omitted, and the time evolution

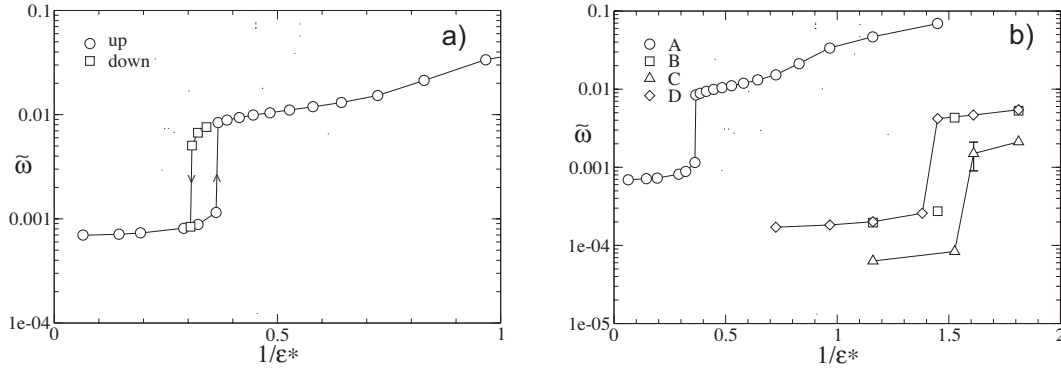


Figure 4.4: a) Terminal angular velocity $\tilde{\omega}$ as a function of $1/\varepsilon^*$ starting from a straight (circles) and from a folded configuration (squares), showing a hysteresis cycle. b) Same plot as a) for a straight initial configuration for all 4 cases A-D. Hydrodynamic interactions are thus not a prerequisite for this wrapping transition.

becomes deterministic. Energies are rescaled by T , and lengths and times as before. For non-zero temperatures $\tilde{M} \equiv M/k_B T$ is defined. Similar to eq. (3.18) I set

$$\varepsilon^* = \frac{\varepsilon}{ML} \quad (4.4)$$

where L is the length of the rotating part of the chain, that is for $N = 30$ used in this simulation, $L = 58a$. $1/\varepsilon^*$ is proportional to the torque if the elastic parameters are fixed.

The filament is thought to be attached at its base to a hypothetical cell body. In the *stalled* case the first two monomers are fixed by virtual forces; in the *moving* case virtual forces are applied to the first two monomers only laterally which are otherwise free to move in the z -direction. The following cases are investigated:

- A: The first two monomers are fixed by virtual forces, but the virtual forces have no hydrodynamic effect on the other monomers. The remaining hydrodynamic interactions are taken into account. It is chosen to illustrate the influence of the hydrodynamic effects from the virtual forces, and also because it shows the strongest shape transition effects.
- B: The stalled case with full hydrodynamic interactions where the virtual forces also act hydrodynamically on the other monomers. Every time step a 6×6 matrix has to be inverted to find the virtual forces.
- C: The free draining case. If the shape transition comes about due to a coupling between hydrodynamics and flexibility then no effect should be seen here.
- D: The moving case with full hydrodynamic interactions. The x and y velocities of the first two monomers are fixed by virtual forces. The simulation proceeds as in case A such that every time step a 4×4 matrix is inverted.

In the simulation a rescaled time step of the order of 10^{-3} is chosen, and a total simulation time up to 10^8 steps. Fig. 4.3b shows the center-of-mass angle θ_{CM} as a function of time as well as the angular velocity for $1/\varepsilon^* = 0.39$, which is slightly above the transition value. θ_{CM} is defined as the angle which the line from the center of mass of the filament \mathbf{R}_{CM} to \mathbf{r}_1 forms

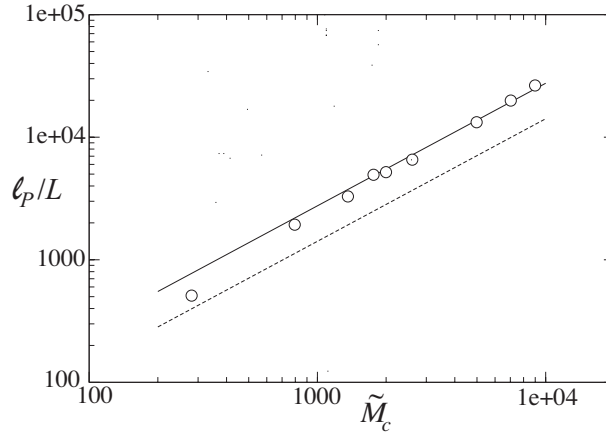


Figure 4.5: Critical torque T_c versus rescaled persistence length for case A *including temperature*. The solid line is the zero-temperature limit obtained from fig. 4.4b. The dashed line is the scaling prediction eq. (4.6)

with the axis of rotation \hat{e}_z . Here and in fig. 4.4a, case A is chosen, but cases B-D give similar results. Starting from a straight configuration, $\theta_{CM} = 45^\circ$, the rod bends while the upper end lags behind, and after roughly two full turns, $\tilde{t} \approx 12000$, the filament folds itself around the z -axis and θ_{CM} decreases. Due to the reduced friction of the folded state the angular velocity $\tilde{\omega}$ increases considerably. It will therefore be a useful parameter describing this dynamical transition.

Fig. 4.4a shows the terminal angular velocity as a function of the inverse elastic parameter $1/\varepsilon^*$ for a straight and a folded initial configuration. Below a critical $1/\varepsilon^*$ the filament is only moderately deformed; $\tilde{\omega}$ stays nearly constant. For higher values $\tilde{\omega}$ increases nearly abruptly by a factor of more than ten. After the transition the filament continues to deform but at a much slower rate which is reflected by the slowly increasing $\tilde{\omega}$. A hysteresis is seen in this zero temperature case. In fig. 4.4b the “up” part of the hysteresis, i.e. the runs starting from a non-folded straight configuration, is shown for the four cases A-D. B and D lie nearly on top of each other. In the free draining case C, the transition occurs at the highest torque or smallest bending modulus ε , respectively. One can see that hydrodynamic interactions are not necessary for this effect, but greatly enhance it. It is of purely elastic origin. In the following, simulations always start from the unfolded configuration. Qualitatively, the transition takes place when the bending radius R gets of the order of the filament length, $R \sim L$. Balancing the bending torque due to deformation, $\varepsilon \sin \theta_1 / R$, and the external torque M one finds

$$\varepsilon^* = \frac{\varepsilon}{M L} = \sin \theta_1 \quad (4.5)$$

which is correct within twenty percent for the cases B-D (fig. 4.4b). The critical value of $1/\varepsilon^*$ in case A is about a factor of four too small. In the case of non-zero temperature eq. (4.5) becomes

$$\frac{\ell_P}{L} = \frac{M}{k_B T} \sin \theta_1 \quad (4.6)$$

which is plotted in fig. 4.5 for several $M/k_B T$ and shows that the transition is not modified by the inclusion of a heat bath.

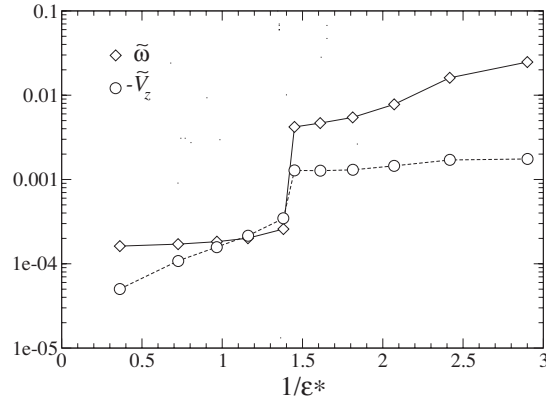


Figure 4.6: Angular and translational velocity of the filament in the moving case D across the critical $1/\varepsilon^*$. At the transition a jump not only of ω but also of V_z takes place. For rigid rods, $1/\varepsilon^* \rightarrow 0$, the propulsion velocity vanishes.

A similar elastic instability was described in the presence of twist and at higher threshold critical angular frequencies [187], or using resistive-force theory [142]. The importance of the above phenomenon is that it can serve as a new propulsion mechanism at low Reynolds number [105], which will be studied next. It might also be a method of determining the bending modulus. For bacteria torsional stiffness should certainly be included in the analysis. However, artificial motors have been developed that have freely rotating backbones [33] which are well described by our bead model.

4.3 Propulsion efficiency

So far hydrodynamic interactions were not essential. This changes when the filament is allowed to move, viz. case D. In that case, the rotating filament moves in negative z -direction, i.e. in the direction of the cell body. For a rigid straight rod, $1/\varepsilon^* \rightarrow 0$, a vanishing propulsion velocity V_z is expected from the analysis of the first section, using e.g. the Gray-Hancock argument [61]. Indeed, a strong decrease of $-\tilde{V}_z$ can be seen in fig. 4.6. Finite elasticity leads to forward thrust irrespective of the sense of rotation. The setup can function as force-rectifying device: A randomly turning motor will always move in one direction, which is not the case for a rigid helix. At the critical $1/\varepsilon^*$ the absolute value of \tilde{V}_z increases by more than a magnitude. One can envision a motor that can slightly change its torque thereby switching between very different velocities.

To be more realistic, the cell body also adds some load to the self-propelling object. The load force F_L points in positive z -direction, i.e. is opposed to the swimming velocity V . For *rigid propellers* the linear relation [63]

$$\begin{pmatrix} V_z \\ \omega \end{pmatrix} = \begin{bmatrix} \mu^{tt} & \mu^{tr} \\ \mu^{rt} & \mu^{rr} \end{bmatrix} \begin{pmatrix} F_L \\ M \end{pmatrix}. \quad (4.7)$$

holds with constant μ^{tt} , μ^{tr} and μ^{rr} . For flexible objects the matrix elements depend also on

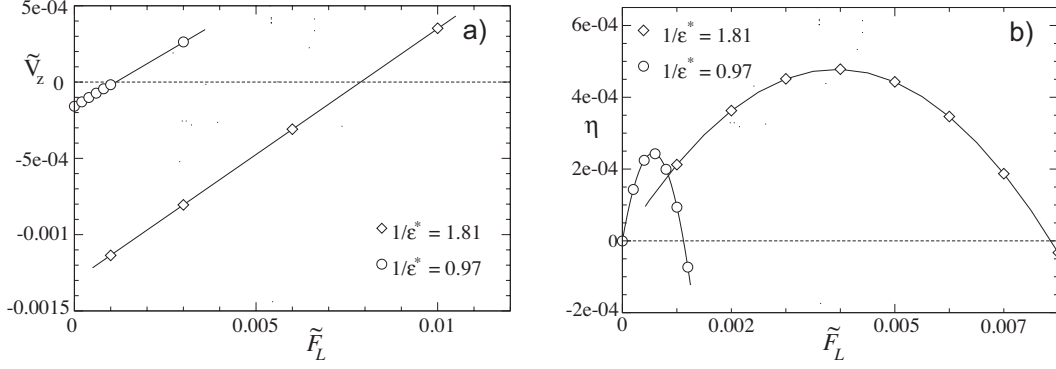


Figure 4.7: a) Propulsion velocity as a function of the load force F_L for $1/\varepsilon^*$ below (circles) and above the transition (diamonds). The lines are linear fits. b) Efficiency of the power converter as defined in eq. (4.9). The lines are parabolic fits with the maxima occurring at $F_L = F_{\text{stall}}/2$.

M and F_L . It will be shown, however, that eq. (4.7) is still approximately valid, except at the transition. One can see from fig. 4.6 that $\mu^{rr} \approx \text{const}$, and from fig. 4.7a that $\mu^{tt} \approx \text{const}$, with different values below and above the transition. It was checked that for ε^* not too far from the transition also $\mu^{tr} \approx \text{const}$. The load force at which the velocity for a given torque gets zero is called the *stall force* F_{stall} . From eq. (4.7) one finds

$$F_{\text{stall}} = -\frac{\mu^{tr}}{\mu^{tt}} M. \quad (4.8)$$

The lines in fig. 4.7a are given by $\tilde{V}_z = -1.6 \times 10^{-4} + 0.14 \tilde{F}_L$ for $1/\varepsilon^* = 0.97$, and $\tilde{V}_z = -0.0013 + 0.165 \tilde{F}_L$ for $1/\varepsilon^* = 1.81$. The abscissae and slopes of these fits yield μ^{tr} and μ^{tt} for the two values of $1/\varepsilon^*$ from which rescaled stall forces of $F_{\text{stall}} = 0.0011$ and $F_{\text{stall}} = 0.0079$ follow.

One can define the efficiency of the power converter as the propulsive power output per rotary power input,

$$\eta = \frac{-V_z F_L}{\omega M}, \quad (4.9)$$

Inserting eq. (4.7) gives

$$\begin{aligned} \eta(F_L) &= -\frac{\mu^{tr} F_L M + \mu^{tt} F_L^2}{\mu^{rr} M^2 + \mu^{rt} F_L M} \\ &\approx -\frac{\mu^{tr} F_L M + \mu^{tt} F_L^2}{\mu^{rr} M^2} \end{aligned} \quad (4.10)$$

since it was checked numerically that for the values investigated

$$\mu^{rr} M \gg \mu^{rt} F. \quad (4.11)$$

η is thus a quadratic function of F_L with its maximum at $F_L = F_{\text{stall}}/2$ (see fig. 4.7b). The quasi-rigid approximation thus holds.

The efficiencies displayed in fig. 4.7b are quite low whereat the folded filament performs better than the one in the normal state. A rigid helix has a propulsive efficiency at the percent level [24, 145], which is at least a magnitude better than the rotating rod. On the other hand, as Purcell [145] pointed out, efficiency is not really an issue for bacteria. The higher power consumption of the presented mechanism will be compensated by a greater flexibility of use. Summarizing, a rotating elastic filament thus offers an alternative to a rotating quasi-rigid helix (as assumed for bacterial flagella) or beating cilia [183].

Can this effect be observed? For the macroscopic scale model of [76] with a filament length of $L = 24$ cm and a bending modulus ε of the order of 10^{-2} Nm² eq. (4.5) yields a critical torque of about $M = 0.05$ Nm. Hence, it should be no problem to test the prediction of this chapter quantitatively. The flagellar motor of *E. coli* generate torques of the order of $M = 10^3 k_B T$ [11]. Using a filament length of $L = 10 \mu\text{m}$ and a persistence length of $\ell_P = 2.5$ mm for the flagellum [76] one gets $\ell_P/L = 250$ which is well below $M/k_B T = 10^3$. For actin with a similar length but a much smaller persistence length of $\ell_P \sim \mathcal{O}(10 \mu\text{m})$ [57] torques of a few $k_B T$ should be sufficient. The effect should therefore easily be observed for straight biopolymers attached microscopic motors.

Chapter 5

Sedimentation of Flexible Polymers

The importance of (long-ranged) hydrodynamic interactions (HI) for various quantities in external fields constitutes a major thread in this thesis. This chapter demonstrates once more that a hydrodynamic description within the Oseen framework as compared to a local or preaveraged one leads to qualitatively different results. The classical problem of a flexible polymer in a homogeneous flow [74] is revisited and applied to ultracentrifugation and electrophoresis. In a sedimentation velocity experiment (as compared to a sedimentation equilibrium experiment) the moving boundary of the investigated substance with time is recorded to obtain the sedimentation coefficient S (defined as the radial velocity per centrifugal acceleration) [64]. In sufficiently dilute solutions interactions between the macromolecules are negligible, and the mass and conformation determine S . In a series of classical papers, dilute solutions of long DNA ($> 10^8$ Da) showed a concentration independent decrease of S with increasing rotor speed [26, 151]. This was explained by Zimm [191] through a deformation of the polymer coil to a more ellipsoidal form caused by the inequality of the friction in the center and at the boundary of the coil: The middle part receives greater hydrodynamic shielding while the ends lag behind. In order to solve the problem analytically a preaveraged form of the hydrodynamic interaction tensor was used which was able to correctly predict the trend for linear polymers but could not achieve quantitative agreement with experiments [26]. Further, polymer rings are not deformed within Zimm's theory contrary to experiments [146].

Ignoring complications due to backflow (for not infinitely dilute systems) and interactions with the ultracentrifuge tube boundary the centrifugal force per monomer G can be written as

$$G = m \omega^2 R_{\text{AUC}} (1 - \rho_{\text{sol}} \bar{v}_p) \quad (5.1)$$

where m is the mass per monomer, ω the angular velocity and R_{AUC} the radius of the analytical ultracentrifuge (AUC) at which the probe is placed. ρ_{sol} is the mass density of the solvent and \bar{v}_p the partial specific volume of the polymer which accounts for the buoyancy. The sedimentation coefficient or rate reads

$$S' = \frac{V_p}{\omega^2 R_{\text{AUC}}} \quad (5.2)$$

where V_p is the radial velocity of the polymer. Since masses do not appear in this low-Reynolds number description I will use a slightly different definition,

$$S = \frac{V_p}{G}, \quad (5.3)$$

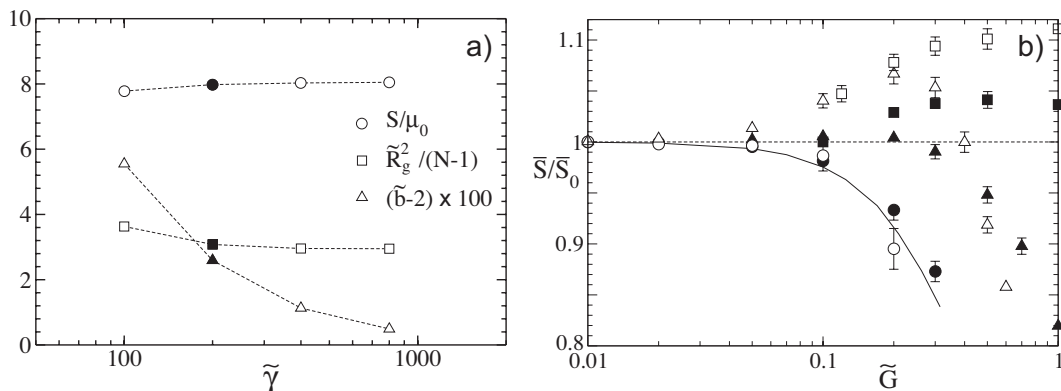


Figure 5.1: a) Test of the $\gamma \rightarrow \infty$ limit for the numerical implementation of the FJC: Rescaled sedimentation coefficient S , radius of gyration \tilde{R}_g and average bond length \tilde{b} for a $N = 60$ chain at $\tilde{G} = 0.5$. It can be seen that $\tilde{\gamma} = 200$ (filled symbols) is a good compromise between accuracy and numerical efficiency. b) Test of Zimm's theory for linear $N = 40$ chains: Relative approximate sedimentation coefficient \tilde{S}/\tilde{S}_0 , eq. (5.6), for a self-avoiding FJC (squares), eq. (5.9), and self-avoiding (triangles) and ideal (circles) Gaussian chains, eq. (5.8). White symbols are for Rotne-Prager HI, black ones for preaveraged HI. The solid line is Zimm's calculation for preaveraged Gaussian ideal chains, eq. (5.7). For Gaussian chains $\tilde{\gamma} = 3/2$, for the FJC $\tilde{\gamma} = 200$ is chosen.

which will subsequently be called the *sedimentation coefficient* in this chapter. It will be rescaled by the mobility of a single bead,

$$\tilde{S} = S/\mu_0. \quad (5.4)$$

Due to the overlap of the flow fields of the individual beads, S depends strongly on the configuration and is roughly determined by the largest length scale of the chain. Ultracentrifugation is therefore a sensitive method to measure changes of the chain configuration under strong homogeneous external forces.

5.1 Comparison of different models and approximations

Starting point is Zimm's Gaussian ideal chain model with a preaveraged Oseen tensor which is widely used to describe velocity sedimentation data of long (chromosomal) DNA [26, 146, 151, 192]. It will be investigated whether his predicted rotor speed dependence is a general feature of flexible polymers, and whether relaxing some of his approximations can lead to new effects of possibly great experimental relevance. In the later sections I will then concentrate on swollen (excluded volume) chains where the hydrodynamics are treated on the Rotne-Prager level. In that case both a compactification or an unfolding can arise depending on G and N where as usual N is the number of monomers per chain.

Preaveraging replaces the distance dependent mobility tensor by its equilibrium value:

$$\mu_{ij} = \frac{\mathbf{I}}{2\eta a \sqrt{6\pi^3 |i-j|}} \quad (5.5)$$

Monte Carlo studies showed that the error by this approximation is usually less than twenty percent [193]. Since the sedimentation velocity becomes independent of the configuration

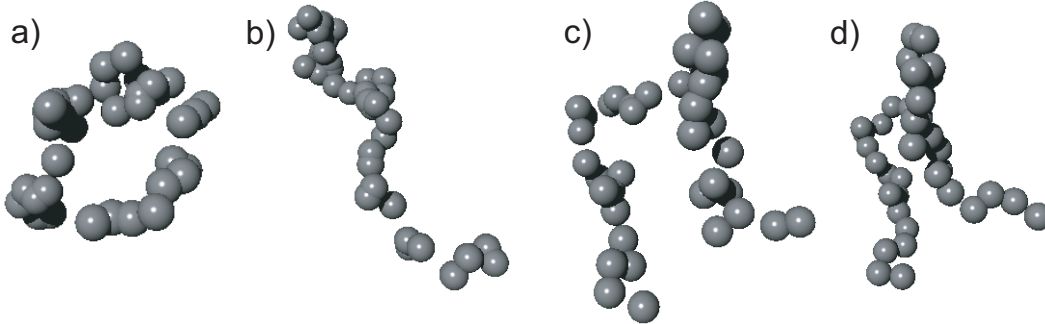


Figure 5.2: *Low field* configurations of a $N = 40$ chain with $\tilde{G} = 0.2$ for ideal Gaussian chains with PA and RP, a self-avoiding Gaussian chain with PA, and a self-avoiding FJC with PA (from left to right), i.e. the cases 1, 2, 3 and 5. In a)-c) $\tilde{\gamma} = 3/2$, in d) $\tilde{\gamma} = 200$. Here and in the following snapshots, the sedimentation force points upwards.

if approximation eq. (5.5) is used Zimm looks instead at the approximate sedimentation coefficient

$$\bar{S} = \frac{3\mu_0}{4N} \sum_{i \neq j} \left\langle \frac{1}{r_{ij}} + \frac{z_{ij}^2}{r_{ij}^3} \right\rangle \quad (5.6)$$

where the brackets denote the average over the perturbed configurations. It is obtained from the Oseen tensor if the diagonal elements and elastic forces are neglected.

Normal mode analysis of the Smoluchowski equation for the monomer positions [32] with the mobility tensor replaced by its approximate form of eq. (5.5) yields the distribution functions necessary to evaluate the averages in eq. (5.6). Expanding $\langle 1/r_{ij} \rangle$ and $\langle z_{ij}^2/r_{ij}^3 \rangle$ with respect to the sedimentation field leads to [191, 192] (corrected by [26])

$$\frac{\bar{S}}{\bar{S}_0} \approx 1 - 2.9 \times 10^{-2} [0.039 N^{3/2} \tilde{G}]^2 + 2.1 \times 10^{-3} [0.039 N^{3/2} \tilde{G}]^4 \quad (5.7)$$

for small $\tilde{G} = Ga/k_B T$. \bar{S}_0 is the value of \bar{S} at $\tilde{G} = 0$.

This approximation is tested with simulations using the elastic potential of a *Gaussian chain*

$$U(\{\mathbf{r}_k\}) = \epsilon_{LJ} \sum_{i < j} \Theta(2a - r_{ij}) \left[\frac{(2a)^{12}}{r_{ij}^{12}} - \frac{2(2a)^6}{r_{ij}^6} + 1 \right] + \sum_{i=1}^{N-1} \frac{\gamma}{4a} |r_{i+1}|^2 \quad (5.8)$$

or a *freely jointed chain* (FJC)

$$U(\{\mathbf{r}_k\}) = \epsilon_{LJ} \sum_{i < j} \Theta(2a - r_{ij}) \left[\frac{(2a)^{12}}{r_{ij}^{12}} - \frac{2(2a)^6}{r_{ij}^6} + 1 \right] + \sum_{i=1}^{N-1} \frac{\gamma}{4a} [r_{i+1} - 2a]^2. \quad (5.9)$$

In the first model, $\gamma = 3k_B T/(2a)$ is always chosen to give a an average bond length of $b = 2a$. In the second model, the stretching modulus γ is chosen high enough such that measurable quantities like the sedimentation velocity or the radius of gyration R_g ,

$$R_g = \left(\sum_i \langle (\mathbf{r}_i - \mathbf{R}_{CM})^2 \rangle / N \right)^{1/2}, \quad (5.10)$$

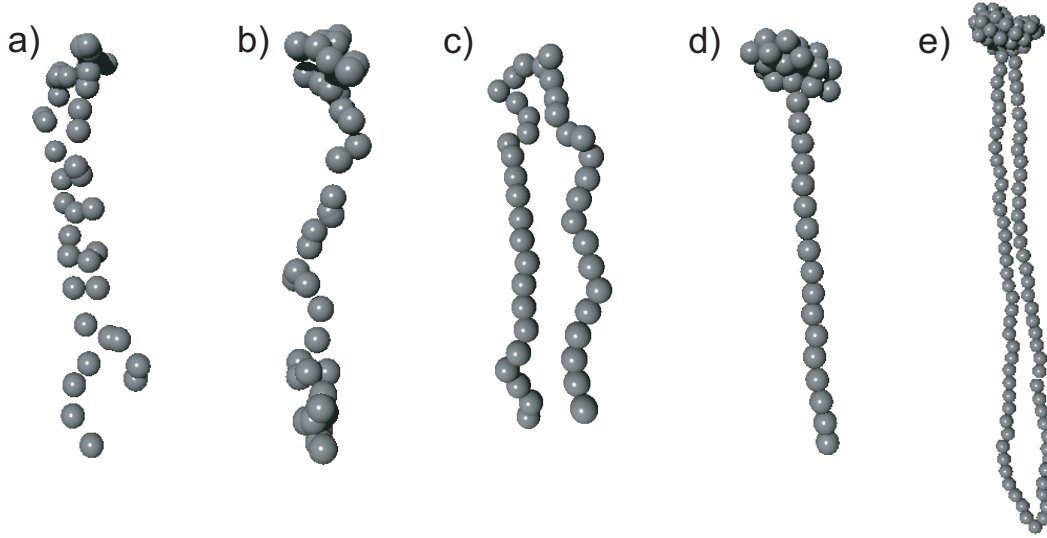


Figure 5.3: Typical configurations for long chains at *high fields* for ideal Gaussian chains (a and b), and self-avoiding FJC (c - e). Parameters: a) PA, $N = 40$, $\tilde{\gamma} = 3/2$ and $\tilde{G} = 1$. b) RP, $N = 40$, $\tilde{\gamma} = 3/2$ and $\tilde{G} = 0.7$. c) PA, $N = 40$, $\tilde{\gamma} = 400$ and $\tilde{G} = 2$. d) RP, $N = 40$, $\tilde{\gamma} = 1600$ and $\tilde{G} = 8$. e) Freely jointed *circular chain* with RP, $N = 140$, $\tilde{\gamma} = 400$ and $\tilde{G} = 2$ (see section 5.3).

are nearly independent of it, usually $\tilde{\gamma} \geq 400\tilde{G}$ (see fig. 5.1a). $\mathbf{R}_{\text{CM}} = \sum_i \mathbf{r}_i / N$ denotes the center of mass. In eq. (5.8) $\epsilon_{\text{LJ}} = 0$ is set for the *ideal* and $\epsilon_{\text{LJ}} = k_B T$ for the *self-avoiding chain*.

The following cases are investigated (in eq. (5.9) only the case $\epsilon_{\text{LJ}} = k_B T$ is considered):

- 1: Ideal Gaussian chain with preaveraged hydrodynamic interactions (PA). This is used in Zimm's calculation.
- 2: Ideal Gaussian chain with Rotne-Prager hydrodynamics (RP).
- 3: Self-avoiding Gaussian chain with PA.
- 4: Self-avoiding Gaussian chain with RP.
- 5: Self-avoiding FJC with PA.
- 6: Self-avoiding FJC with RP. This is the standard in most simulations if not otherwise mentioned. This case will also be used for circular chains.

Fig. 5.1b shows these six cases in the limit of small \tilde{G} : For ideal Gaussian chains the preaveraging approximation induces only a minor change in \bar{S}/\bar{S}_0 . A monotonic decrease as calculated by Zimm can be seen. Self-avoiding chains, on the other hand, pass through a maximum before they also decrease. The maximum is more pronounced if the Rotne-Prager tensor is used. An even more drastic effect is seen for self-avoiding FJC.

Configurations at low field, $\tilde{G} = 0.2$, are shown in fig. 5.2. The ideal Gaussian chain with PA (a) is compared with chains in which one of the following parameters is changed: $\epsilon_{\text{LJ}} = k_B T$ (b), RP (c), and self-avoiding FJC (d). For PA both ends point downward while for RP also an unfolding can occur.

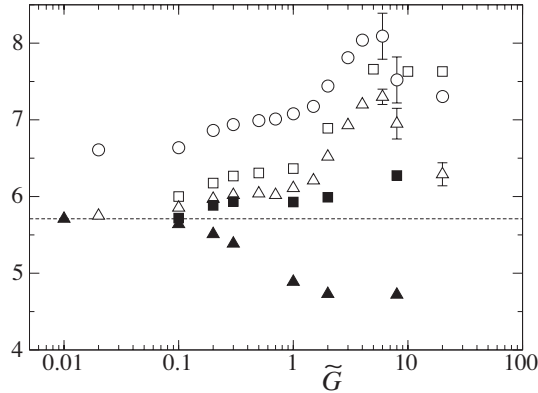


Figure 5.4: Self-avoiding FJC with $N = 40$: S/μ_0 (circles), \bar{S}/μ_0 (squares) and N/\tilde{R}_h (triangles) - defined in eqs. (5.3), (5.6) and (5.11) - for preaveraged (black symbols) and Rotne-Prager hydrodynamics (white symbols). For preaveraged HI the rescaled sedimentation coefficient is constant by construction, $S/\mu_0 \approx 10.46$. The dashed line is the $G \rightarrow 0$ limit of N/\tilde{R}_h .

For higher fields the difference between PA and RP becomes more visible (see fig. 5.3a-d). PA chains approach a double-strand configuration, RP chains a “tadpole” structure with a dense head and an unfolded tail. Fig. 5.3e shows a circular chain for which Zimm’s model predicts no rotor speed dependence [146, 191]. It will be considered in more detail later. In the following I will concentrate on linear self-avoiding FJC with RP. This will be henceforth called the *standard type*.

Whether S and \bar{S} are related is tested in fig. 5.4 for self-avoiding FJC. Snapshots of the two chains are presented fig. 5.3, (c) and (d). Also shown is the inverse hydrodynamic (Kirkwood) radius [32]

$$\frac{1}{R_h} = \frac{1}{N^2} \sum_{i \neq j} \left\langle \frac{1}{r_{ij}} \right\rangle \quad (5.11)$$

which is the angular average of $\bar{S}/(\mu_0 N)$. In the limit $\tilde{G} \rightarrow 0$, \bar{S}/μ_0 and N/\tilde{R}_h are therefore the same; for higher fields \tilde{G} , \bar{S}/μ_0 lies above N/\tilde{R}_h . For Rotne-Prager HI (white symbols) S/μ_0 , \bar{S}/μ_0 and N/\tilde{R}_h show the same trend, whereas for preaveraged HI (black symbols) \bar{S}/μ_0 increases while N/\tilde{R}_h decreases. The sedimentation coefficient S is independent of \tilde{G} , viz. $S/\mu_0 \approx 10.46$. Eq. (5.5) is derived for an ideal chain, S is thus much larger than for this swollen chain. In eq. (5.6) both the largest dimension of the chain, $\langle 1/r_{ij} \rangle$, and its orientation, $\langle z_{ij}^2/r_{ij}^3 \rangle$, contribute: In fact, in fig. 5.2d the Kirkwood hydrodynamic radius R_h increases with \tilde{G} although \bar{S} does not decrease (see fig. 5.4).

Summarizing, all types of flexible chains show a qualitatively different behavior at high rotor speeds when hydrodynamic interactions are taken into account on a non-preaveraged level. This means that results for the sedimentation coefficient are highly model dependent, and the universality hypothesis according to which the Gaussian model correctly captures large-scale and long-time properties is violated in this far-from-equilibrium situation.

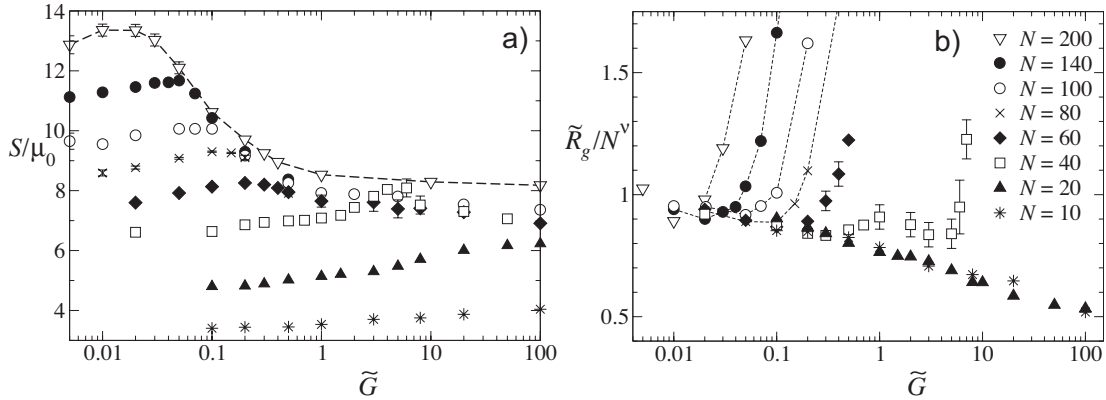


Figure 5.5: a) Sedimentation coefficient of a self-avoiding linear FJC for several monomer numbers (legend in b) over four decades of \tilde{G} . The broken line connects the points with $N = 200$. b) Reduced radius of gyration for the same chains using $\nu = 0.588$ [32]. Some points are connected for better visibility.

5.2 Compactification of short chains

In the next two sections I will only investigate the self-avoiding linear FJC, i.e. the standard type. Circular chains are treated in section 5.3. Fig. 5.5a shows S/μ_0 over four decades of \tilde{G} for *linear* chains with $N = 10$ to $N = 200$ monomers. With the exception of the two shortest chains, the sedimentation coefficient $S(\tilde{G})$ displays a non-monotonic behavior: For small fields, S increases slightly; the polymer coil gets more condensed. After passing through a maximum, S drops considerably until it saturates at a much lower value than for the unperturbed ($G \rightarrow 0$) chain. It is interesting to note that the longest chain with $N = 200$ is the envelope of the other chains, which is indicated by connecting the symbols with a broken line. Curves of long chains seem not to cross each other, different from short chains (see $N = 40$). Two critical centrifugal field values characterize the curves: \tilde{G}^* where the chains start to unfold and \tilde{G}^{**} where - if present - they start to form a dense globule.

Close to equilibrium, i.e. $\tilde{G} = 0$, hydrodynamic interactions lead to a crumpling of the front part (in the direction of motion) of the chain, which eventually leads to a prolate spheroid. Fig. 5.5b shows the field dependence of the radius of gyration, R_g , divided by the swollen chain prediction for $G = 0$, $R_g \sim N^\nu$ with $\nu = 0.588$ [32]. Irrespective of N , R_g decreases from unity until it abruptly increases again at $G^*(N)$. For $N = 20$ and $N = 10$ G^* is either not yet reached in this simulation, or the chains are too short for this long-chain behavior to take place.

What is the mechanism for the compactification of the chains before they unfold? Monomers in the center of the coil move faster than those outside. This leads to an internal recirculation of the chain with a velocity that scales as $v \sim \mu_0 G N a / R_g$, where it is assumed that R_g scales like hydrodynamic radius of the chain. This gives a recirculation time scale of

$$\tau_c \sim R_g / v \sim \frac{R_g^2}{\mu_0 G N a}. \quad (5.12)$$

In order to compress the chain, the recirculation time scale τ_c needs to be shorter than the

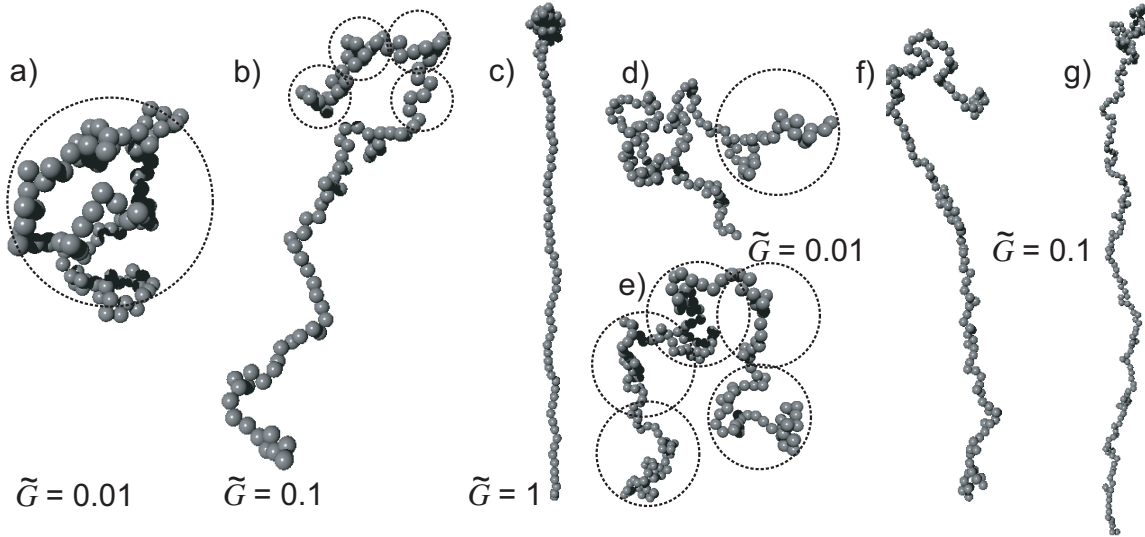


Figure 5.6: Typical configurations of a self-avoiding FJC for $N = 100$ (a-c), $N = 140$ (d, f), and $N = 200$ (e, g) for case 6 and $\tilde{\gamma} = 200$, except for (c) where $\tilde{\gamma} = 400$. Circles represent the estimated blob size ξ .

coil relaxation time $\tau_R \sim R_g^3/(\mu_0 k_B T a)$, which gives the scaling

$$\tilde{G}^{**} \sim N^{-1-\nu} . \quad (5.13)$$

When $\tilde{G} > \tilde{G}^{**}$, the chain with monomer number N begins to collapse.

It is interesting to note that the chains of different length show the same behavior at small fields \tilde{G} (see fig. 5.5b). Before the transition the curves of \tilde{R}_g/N^ν lie nearly on top of each other; the contraction is small and seems to be scale invariant. It can be accounted for by extending the recirculation picture by a blob argument: It is assumed that for small fields the chain is still self-avoiding on small length scales. As a whole it consists of a globule (or an elongated string) of blobs in which the chain is self-avoiding. The blob size ξ decreases when G is raised. Below \tilde{G}^{**} , the blob size is larger than the chain, $\xi > R_g$, and the scaling behavior is unchanged. If \tilde{G} is raised above \tilde{G}^{**} , the chains collapse on smaller and smaller scales. The collapsing starting from large scales is intuitively clear as the velocity difference is greatest between the center and the outer boundary of the coil; neighboring monomers move with nearly the same speed. The argument proceeds as before but on the scale of a blob: The recirculation time τ_c and coil relaxation time τ_R for the blob are $\tau_c \sim \xi R_g/(\mu_0 G N a)$ and $\tau_R \sim \xi^3/(\mu_0 k_B T a)$, respectively. This leads to a blob size of

$$\xi \sim \left(\frac{R_g a}{\tilde{G} N} \right)^{1/2} . \quad (5.14)$$

For $\tilde{G} = \tilde{G}^{**}$ the blob size is $\xi \sim (R_g a N^\nu)^{1/2} \sim R_g$ as anticipated.

According to the blob picture with an *overall globular structure*, the size R_g of the chain is $R_g \sim \xi (N/n)^{1/3}$ where n is the number of monomers inside one blob, i.e. $n \sim (\xi/R_g)^3 N$. With eq. (5.14) one arrives at

$$R_g \sim a N^{\frac{1-\nu}{3\nu+1}} \tilde{G}^{\frac{1-3\nu}{3\nu+1}} , \quad \tilde{G} > \tilde{G}^{**} . \quad (5.15)$$

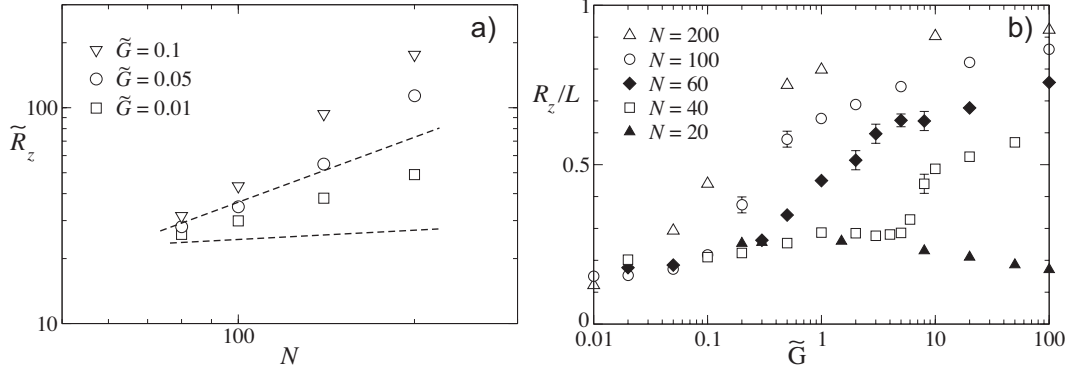


Figure 5.7: a) N -dependence of the maximum extension at three different field strengths. The lines have slopes one and 1/7, respectively. b) Relative root mean square maximum extension in field direction, R_z/L , as a measure for the unfolding of the linear chains.

For self-avoiding chains one has $\nu \approx 3/5$ and thus

$$R_g \sim a N^{1/7} \tilde{G}^{-2/7} \quad , \quad \tilde{G} > \tilde{G}^{**} \quad , \quad (5.16)$$

and

$$\xi \sim a N^{-3/7} \tilde{G}^{-9/14} \quad . \quad (5.17)$$

The scaling of eq. (5.16), $R_g \sim N^{1/7}$, is only valid until the blob size ξ is of the order of the monomer radius a . For longer chains or higher fields, the radius of gyration scales like a compact object, $R_g \sim N^{1/3}$. This scaling is not reached for long chains because they unfold before appreciable compactification sets in.

Fig. 5.6 shows typical configurations for different field strengths and chain lengths. The dashed circles show the estimated blob sizes ξ that scale approximately as in eq. (5.17). In (a) the whole chain is inside one blob, the compactification is small. In (b) and (e) the chain consists of a string a unperturbed pieces. The global structure can be a globule, as assumed in equations (5.14) to (5.17) and displayed in (a), (d) and (e) for a rescaled field strength of $\tilde{G} = 0.01$, or already partially unfolded as in (b), (f) and (g) for $\tilde{G} = 0.1$. Fig. 5.6c shows the nearly completely unfolded state at $\tilde{G} = 1$.

For long chains, the unfolding starts before the globular structure is reached on small length scales. The hydrodynamic forces that lead to the recirculation at small fields also elongate the chain at higher field strengths. To that end another chain length is defined, the root mean square of the maximum extension in z -direction

$$R_z = \left(\langle \max^2[r_{i,z} - r_{j,z}] \rangle \right)^{1/2} \quad . \quad (5.18)$$

In the *extreme case of straight chain of blobs*, the argument above with the maximum extension R_z instead of the radius of gyration as the relevant length scale leads to

$$R_z \sim a N \tilde{G}^{1/4} \quad (5.19)$$

$$\xi \sim a \tilde{G}^{-3/8} \quad (5.20)$$

where logarithmic factors are neglected and assuming a scaling of the center-of-mass velocity of $v \sim \mu_0 G N a / R_z$. The blob size is nearly independent of the chain length, and the extension

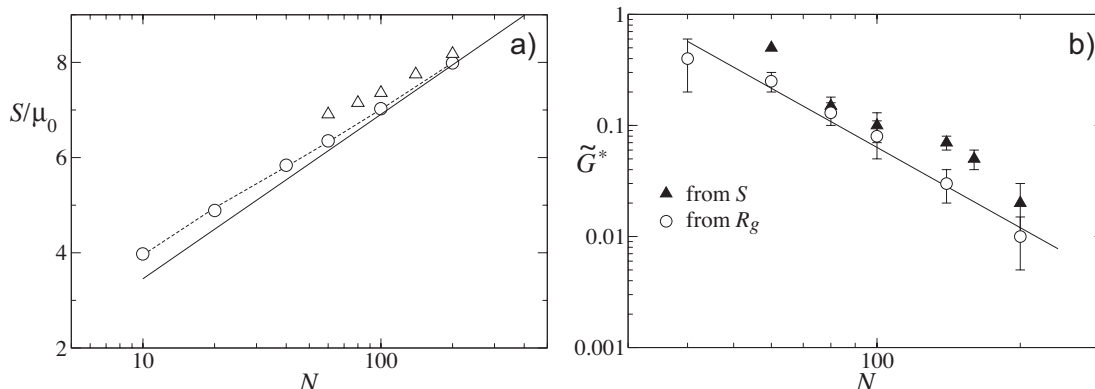


Figure 5.8: a) Sedimentation coefficient as a function of monomer number for $\gamma = 200G$ in the zero-temperature limit. Circles show the deterministic case starting with a straight chain at an angle of 45° to the G . The dashed line is eq. (5.23) with $c = 0.48$. The solid line is the long-tail limit $S/\mu_0 = (3/2) \ln(N)$. Triangles are the values for $\tilde{G} = 100$ from fig. 5.5a. b) Field strength where the unfolding starts, \tilde{G}^* obtained graphically from the maxima of S/μ_0 in fig. 5.5a (triangles) and from the points in fig. 5.5b where the sudden rise of R_g begins (circles). The line is $\tilde{G}^* = 4000 N^{-12/5}$.

R_z rises with increasing field strength. The real situation is in-between these two extremes, eq. (5.16, 5.17) and eq. (5.19, 5.20), respectively (see fig. 5.6b). Fig. 5.7a shows how the maximum extension R_z scales with the monomer number. For small fields the blob argument is valid; the exponent of N is between eq. (5.16) and eq. (5.19) and the overall shape neither globular nor elongated. For higher fields, the unfolding sets in and the recirculation alone cannot explain the scaling.

5.3 Unfolding transition

5.3.1 Linear chains

Up to now no explanation has been given why the polymer unfolds. As depicted in fig. 5.3d, the chain approaches a “tadpole” configuration for $G > G^*$. To demonstrate the unfolding more clearly, the relative maximum extension in z -direction, R_z/L , is plotted in fig. 5.7b. For small G a slight elongation of the coils can be seen. Above the field strength $G^*(N)$, the elongation R_z/L rather smoothly crosses over to its final value at infinite G . $L = 2a(N - 1)$ is the contour length.

In order to derive scaling relations for the onset of unfolding it is important to know the limiting values at $G \rightarrow \infty$. A similar (but not completely equivalent) procedure is to express the internal energies in units of G , viz. $\gamma = 200G$ and $\epsilon_{LJ} = Ga$, and omit the random displacements ξ_i as done in eq. (3.13), which amounts to taking the *zero-temperature limit* (cf. section 3.2). In that case, a complete sampling of the phase space is not done, and the final configuration depends on the initial conditions. Often a spinning motion is obtained as the terminal state. The $\xi_i = 0$ case might be illuminating as it describes how the tadpole formation is purely hydrodynamically driven. To be specific, a straight chain at an angle of 45° to the centrifugal field G is chosen as starting configuration and the resulting S shown in fig. 5.8. All chains, even $N = 10$, deform to a two-dimensional tadpole where the size of the

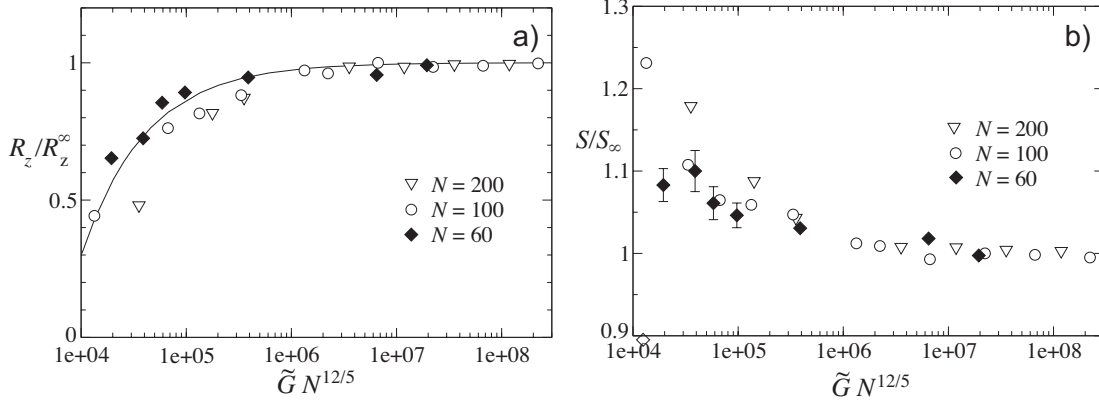


Figure 5.9: a) Extension in field direction R_z divided by its limiting value R_z^∞ for $\tilde{G} \rightarrow \infty$ as a function of \tilde{G}/\tilde{G}^* rescaled according to Eq. (5.25) with $\nu = 3/5$. The solid line is $R_z/R_z^\infty = 1 - 500 [\tilde{G} N^{12/5}]^{-5/7}$. b) Same data points as in (a) for the sedimentation coefficient divided by its $\tilde{G} \rightarrow \infty$ value.

head increases only marginally with N . The solid line is the (approximate) prediction for a completely unfolded chain, $S/\mu_0 = (3/2) \ln(N)$, see eq. (B.30).

On the scaling level, one can model the chain as a spherical head of N_0 beads with mobility c/N_0^ν and a tail of $N - N_0$ beads with mobility $(3/2) \ln(N - N_0)/(N - N_0)$. c is a fit parameter and ν is in the range between $1/3$ and $3/5$ depending on whether the head is a globule or a coil during unfolding. The distance between the points where the forces on the head and the tail apply is approximately $L/2$, which gives an Oseen type HI between these two degrees of freedom of the order of $(3/2)/(N - N_0)$. The equation of motion for this system neglecting elastic forces,

$$\begin{pmatrix} v \\ v \end{pmatrix} = \mu_0 \begin{bmatrix} c N_0^{-\nu} & \frac{3}{2} (N - N_0)^{-1} \\ \frac{3}{2} (N - N_0)^{-1} & \frac{3}{2} \ln(N - N_0) (N - N_0)^{-1} \end{bmatrix} \begin{pmatrix} N_0 G \\ (N - N_0) G \end{pmatrix}, \quad (5.21)$$

is solved for the common velocity v and the number of monomers of the N_0 . Assuming $\nu = 1/3$ and $N \gg N_0$, one gets to lowest order

$$N_0 \sim [(3/2c) (\ln N - 1)]^{3/2} \quad (5.22)$$

and

$$S/\mu_0 \sim (3/2) \ln N + 81 [\ln N - 1]^3 / (32c^3 N^2). \quad (5.23)$$

The dashed line in fig. 5.8 shows this prediction for $c = 0.48$. Also shown are values for $\tilde{G} = 100$ taken from fig. 5.5 approaching this limiting prediction.

What is the field strength necessary to fully unfold the chain? It will be used to estimate the field G^* where the unfolding starts assuming that both display the same scaling with N . A slight backfolding from the tadpole state, i.e. changing N_0 , creates a force on the tail that is proportional to the velocity difference Δv of head and tail. From eq. (5.21) it is clear that the primary change in the velocity difference in the limit $N \gg N_0$ comes from the velocity of the head. If N_0^* denotes the number of monomers in the head in the tadpole state and

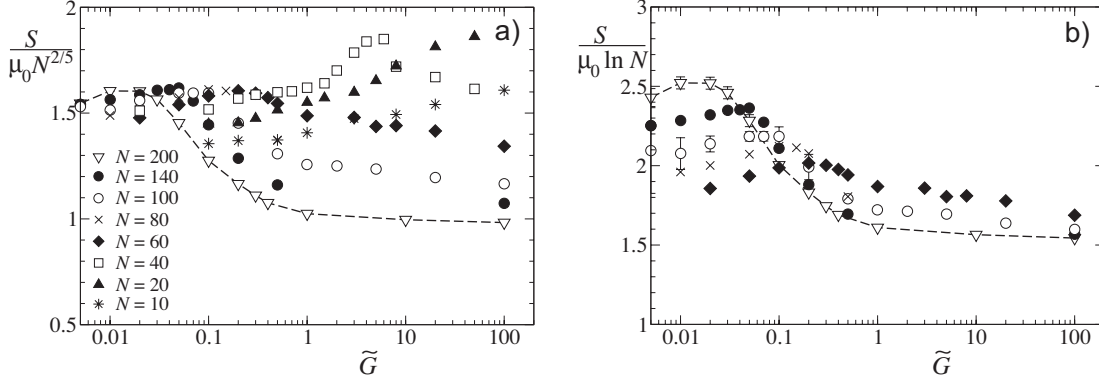


Figure 5.10: Same data as in fig. 5.5 but rescaled with the low and high field prediction, $S/\mu_0 \sim N^{2/5}$ and $S/\mu_0 \sim \ln(N)$, respectively. The short chains are omitted in (b).

$\Delta N_0 = N_0 - N_0^*$ then the velocity difference for $N_0^* \ll \Delta N_0 \ll N$ scales like $\Delta v \sim \mu_0 G \Delta N_0^{1-\nu}$. The force f that the tail acts on the head is thus

$$f(\Delta N_0) \sim \mu_0^{-1} \Delta v (N - N_0) \sim G \Delta N_0^{1-\nu} (N - \Delta N_0). \quad (5.24)$$

Integrating $f(\Delta N_0)$ from a value close to zero up to $N/2$ gives the work with respect to the head of going from the tadpole ground state to the halfway backfolded state, which we demand to equal thermal energy. In principle, this work should be calculated with respect to the center of resistance, but on the scaling level the difference does not matter. The field strength below which thermal fluctuations destroy the tadpole shape follows as

$$\tilde{G}^* \sim N^{-3+\nu}. \quad (5.25)$$

If the head is a coil at the beginning of unfolding, $\nu = 3/5$, which is the case for long polymers, then $\tilde{G}^* \sim N^{-12/5}$. Figure 5.9 demonstrates that the curves for different N can be approximately described by a single curve in the high field limit if one plots them with an argument G/\tilde{G}^* instead \tilde{G} . The scaling is not perfect because the size of the head N_0^* is not negligible for the chains under investigation. R_z^∞ and S_∞ are the values in the limit $\tilde{G} \rightarrow \infty$ of R_z and S , respectively. The line in fig. 5.9a the function $R_z/R_z^\infty = 1 - 500 [\tilde{G} N^{12/5}]^{-5/7}$ where the factor 500 is fitted to $N = 100$. The scaling $1 - R_z/R_z^\infty \sim \tilde{G}^{-5/7}$ is again obtained from integrating equation (5.24) up to a fraction of N .

The data of fig. 5.5a are replotted in fig. 5.10 and divided by the low and high field scaling, $S/\mu_0 \sim N^{2/5}$ and $S/\mu_0 \sim \ln(N)$, respectively. The curves collapse within a factor of approximately ten percent for chain length above $N = 60$.

So far it was tacitly assumed that elastic forces can safely be neglected on the scaling level. In principle one should add the direct force between head and tail to the right hand side of eq. (5.21). This is conceptionally important because the balance of the head and tail velocities does not require the head to move first. If the tail is shorter than the value determined by eq. (5.22) an elastic (stretching) force due to the velocity difference appears that slows down the head and accelerates the tail. In addition, the force unwinds the head making the tail longer and reducing thereby the difference in velocity. An estimate for the force that opposes the unwinding is the force that causes the crumpling of the head by recirculation, which scales

like the number of head monomers times the velocity:

$$F_{\text{head}} \sim G N_0^{2-\nu} . \quad (5.26)$$

In eq. (5.24) the force on the tail due to the velocity difference is estimated under the assumption $N_0^* \ll \Delta N_0 \ll N$. In the opposite limit, $\Delta N_0 \ll N_0^* \ll N$, one finds $\Delta v \sim \mu_0 G \Delta N_0 (N_0^*)^{-\nu}$ and thus for the force on the tail:

$$F_{\text{tail}} \sim G N \Delta N_0 (N_0^*)^{-\nu} . \quad (5.27)$$

Equating both, $F_{\text{head}} \sim F_{\text{tail}} \sim F_{\text{el}}$, and using $\Delta N_0 \ll N_0^*$ gives in the case of $\nu = 1/3$: $\Delta N_0 \sim N^{-1} (\ln N - 1)^3$, and hence

$$F_{\text{el}} \sim G (\ln N - 1)^{5/2} . \quad (5.28)$$

Plugging F_{el} into eq. (5.21) does not change the scaling, equations (5.22) and (5.23). The configuration, in which the tail moves before the head, is unstable as can be seen from the following: If the tail is slightly longer than the velocity balance it moves faster pulling the slower head that hence even more unwinds and shrinks.

It remains to be shown that the scaling eq. (5.25) also describes the beginning of the unfolding. Fig. 5.8b shows \tilde{G}^* defined by two different ways as a function of the monomer number. In both cases the fit function to eq. (5.25),

$$\tilde{G}^* = 4000 N^{-12/5} , \quad (5.29)$$

describes the data quite.

5.3.2 Circular chains

The question arises whether the described behavior is specific to linear chains. Within a preaveraging approach this cannot be decided [146, 191]. Ralston and Schumaker [146] showed that *circular* DNA has a similar sedimentation speed dependence as linear DNA with half the length. Indeed, the curves for the speed dependence of S in fig. 5.11b show a similar trend as those in fig. 5.5a. The maximum extension in field direction, which is approximately the length of the tail, of a circular $N = 200$ chain shows very similar behavior for large G as a linear $N = 100$ chain. The explanation can be found by looking at fig. 5.3e: Circular chains form a two-strand tail the length of which determines the mobility in the unfolded state. However, the sedimentation velocity of a circular $N = 200$ is nearly a factor of two higher than that of a linear $N = 100$ chain in the limit $\tilde{G} \rightarrow \infty$ (see fig. 5.11b). The reason is that the twofold number of monomers (and thus the twofold total centrifugal force) is contained in the tail of the circular $N = 200$ chain compared to the linear $N = 100$ chain, although the lengths and thus the mobilities are nearly equal. At small field strengths circular chains with the same number of monomers are only slightly faster than linear ones. The maximum of $S(\tilde{G})$ is more pronounced than for linear chains, which can be ascribed to the additional topological constraint of a closed chain that hinders the unfolding.

Linear chains and circular chains both show only a logarithmic length dependence of the sedimentation velocity at high fields, but the difference between these two classes is about factor of two. This fact can be exploited to separate linear and circular chains of the same molecular weight. The method should be quite efficient because a factor of two can be easily resolved in an ultracentrifugation experiment, and therefore only short runs are necessary. Closed polymer chains are also relevant in the context supercoils [128] where a strong rotor speed dependence has been observed.

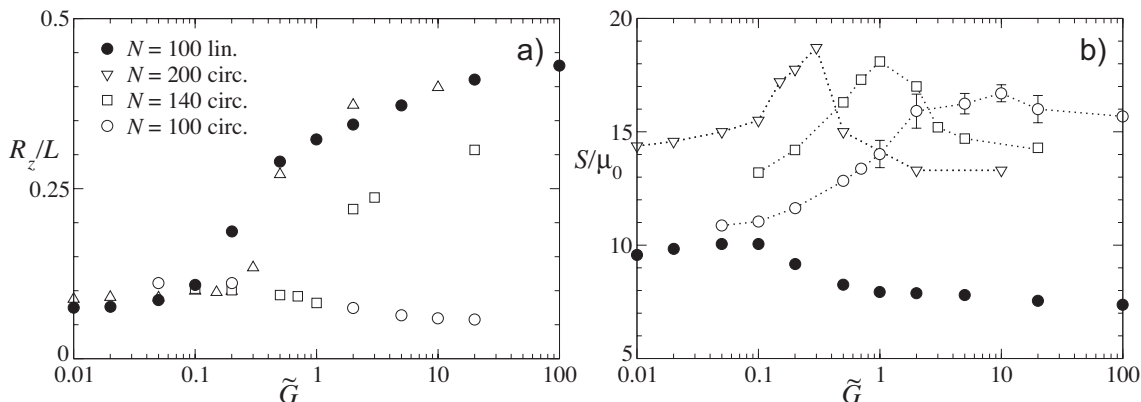


Figure 5.11: Sedimentation of *circular* (white symbols) and *linear* chains (black symbols). a) Relative maximum extension: The black circles are divided by a factor of 2. b) Rescaled sedimentation coefficient: The legend is in part (a).

5.4 Discussion

Unfolding in elongational and shear flow has long been investigated [162]; unfolding in homogeneous flow has not been considered probably due to its smallness compared to the other types of flow at typical shear rates. Historically, the ultracentrifugation studies of flexible polymers were partially motivated by the length separation of very long DNA [151, 192]. To avoid the rotor speed dependent decrease of the sedimentation coefficient and obtain well-defined results, the sedimentation field may not be too large for chromosomal DNA, which makes this separation method less attractive. Our simulations suggest that above a certain monomer number and for a given field strength, longer chains are faster than shorter one, different from [192]. Mass separation is therefore possible at all rotor speeds though difficult. In addition, it allows to separate circular from linear polymers.

There are accounts for an increase of the sedimentation coefficient with rotor speed, as for certain chaperones [18], which can be explained by a deformation of the protein decreasing its dimensions. Rotor speed effects are also observed under theta conditions, as for polystyrene in cyclohexane [28]; the decrease of the sedimentation coefficient is small and approximately in the range of Zimm's theory.

The presented transition might be important in the context of electrophoresis and electric birefringence if strong enough electric fields lead to fast electrophoretic motion. Here a second unfolding mechanism due to dipoles takes place [122] where the critical field strength E^* scales as $E^* \sim N^{-1/2}$, that is with a much smaller power than the proposed unfolding mechanism of this chapter.

It is interesting to ask which birefringence signals correspond to the different stages of the configurational changes in the external field. Fig. 5.12a shows the birefringence parameter χ , see eq. (3.16), as a function of field strength. As expected for system with many degrees of freedom, there are several regimes with different scaling: The low field regime, i.e. a slight deformation of the chain, is only reached for short chains. It is characterized by $\chi \sim \tilde{G}$. In the range where the sedimentation coefficient $S(\tilde{G})$ exhibits a maximum, viz. around $\tilde{G} = 0.1$ for $N = 100$, the birefringence χ increases more steeply, until χ starts to saturate when the chain is unfolded and begins to straighten. The unfolding is less abrupt than in the

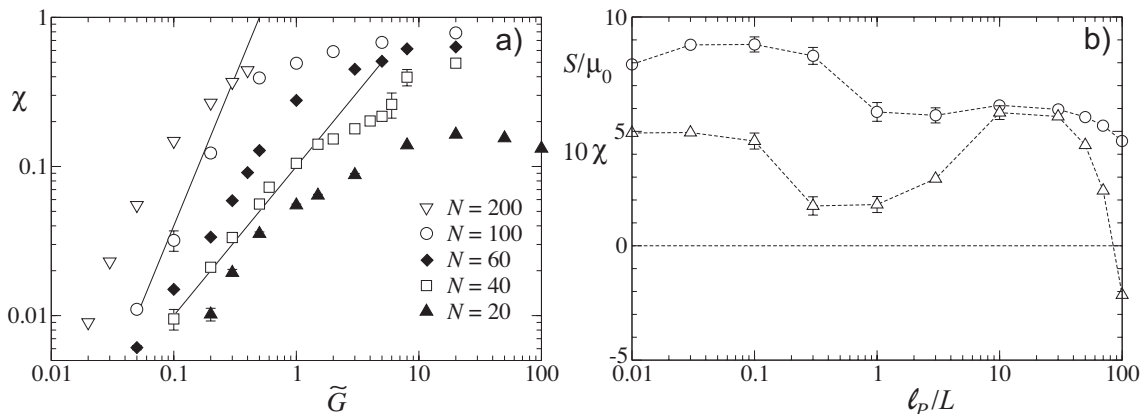


Figure 5.12: a) Birefringence as a function of sedimentation force for different chain lengths. The lines have slope one and two, respectively. b) Birefringence parameter χ (triangles, multiplied by 10 for visibility) and sedimentation coefficient S/μ_0 (circles) as a function of the reduced persistence length ℓ_p/L for $N = 100$, $\tilde{G} = 1$ and $\tilde{\gamma} = 400$.

dipole orientation case [122] which should manifest itself also in the field dependence of the birefringence.

In fig. 5.12b the persistence length is changed from flexible to rod-like for a $N = 100$ chain at a finite field, $\tilde{G} = 1$. The limit of $\ell_p = 0$ is depicted in fig. 5.6c, the opposite limit, $\ell_p \gg L$, was described in detail in chapter 3. The sedimentation coefficient and birefringence parameter show a non-monotonic behavior at $\tilde{G} = 1$. For $a \ll \ell_p \ll L$ the head is more extended than in the completely flexible case. At $\ell_p \sim L$ the head unfolds, and the chain approaches an bent perpendicular oriented arc. For $\tilde{G} \rightarrow 0$, S is proportional to the diffusion constant of a neutral semiflexible chain discussed in chapter 6, which monotonically crosses over from the swollen to the rod behavior. The high field case yields a mobility that is about a factor of two higher in the flexible than in the rod-like limit because in the former the tadpole rods point in field direction and in the latter perpendicular to it. The last figure suggests that an analytical ultracentrifuge can be used to determine the persistence length and other elastic parameters if the rotor speed can be tuned over a wide range.

Chapter 6

Salt Dependent Diffusion of Semiflexible Polymers

So far the problem was completely hydrodynamical. The systems were neutral and infinitely dilute: Electrostatic interactions, counterions, salt and other polymers were not taken in to account. From now on I will also consider charged polymers, i.e. polyelectrolytes, which introduces two additional lengths to the system, the screening length $\tilde{\kappa}^{-1}$ and the box size B as a measure for the semi-diluteness of the polymer solution. In this chapter I will be concerned with the diffusion and small-field sedimentation of semiflexible and rod-like polymers in an electrolyte solutions. It is in some sense complimentary to the last chapter that concentrated on strong fields and flexible polymers.

The long-time translational diffusion constant of the center of mass \mathbf{R}_{CM} of a microscopic object is defined as

$$D = \lim_{t \rightarrow \infty} \frac{\langle [\mathbf{R}_{CM}(t) - \mathbf{R}_{CM}(0)]^2 \rangle}{6t}. \quad (6.1)$$

By virtue of the fluctuation-dissipation theorem [88], it is equal to the linear response with respect to an external force F_G , called the *sedimentation force*, acting only on this object and not on e.g. the small ions:

$$D = k_B T \lim_{F_G \rightarrow 0} \frac{(\dot{\mathbf{R}}_{CM})_z}{F_G} \quad (6.2)$$

where it is assumed that F_G points in z -direction. Since for most experimental situations the sedimentation force can be considered as weak (with respect to $k_B T$ divided by the typical particle dimension) both problems will be treated interchangeably.

A related transport process is electrophoresis of semiflexible polymers for which there exists a considerable number of publications, both experimentally [68] and theoretically [6, 108]. Since the electric field moves the polyelectrolyte and the counterions in opposite directions hydrodynamic interactions are screened over distances much larger than the Debye-Hückel screening length, resulting in a logarithmic dependence of the electrophoretic mobility on the ionic strength for long polymers. On the other hand, the literature dealing with the effect of the ionic strength on the sedimentation and diffusion of dilute polymer solutions is rather sparse. In the last few years experimental methods have become available to investigate polymer diffusion on the single molecule level [86]. Understanding salt dependent diffusion may help to resolve discrepancies of diffusion measurements in different buffer solutions, and is relevant for many biological processes on the intracellular level. It may also clarify the

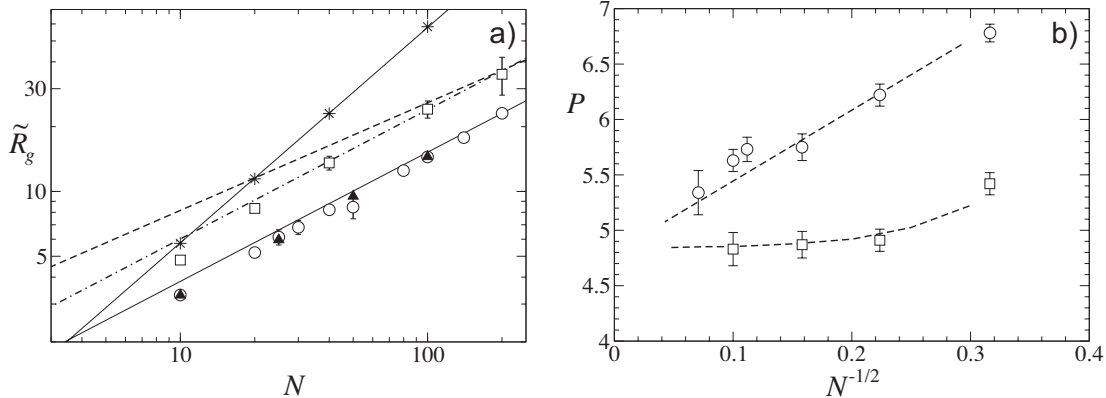


Figure 6.1: a) Radius of gyration versus monomer number for freely-jointed chains with (circles) and without hydrodynamic interactions (black triangles), semiflexible chains with $\ell_P = 10a$ (squares) and rod-like chains with $\ell_P = 5L$ (stars). The upper solid line is linear, eq. (6.16); the lower solid line has an exponent $3/5$, eq. (6.7); the dotted-dashed line is eq. (6.10); and the dashed line is eq. (6.13). b) Flory parameter P of a FJC with excluded volume for $\ell_P = 0$ (circles) and $\ell_P = 10a$ (squares). The lines are guides to the eye.

applicability of the Nernst-Einstein equation which recently caused some confusion in the literature [170].

6.1 Diffusion of neutral semiflexible chains

Before turning to the salt dependence I briefly address the diffusion of a neutral semiflexible chain where the flexible and the rod-like limits are well investigated. Analytical treatments for the intermediate regime [65, 189] neglect the self-avoidance of the chains and yield complicated expressions not very practical for a comparison with experiments. For this reason I propose a *heuristic interpolation formula* that serves as a reference state for the salt dependence of the diffusion constant but might also be important in its own right.

Flexible chains

The flexible regime is determined by $\ell_P \ll L$. For a realistic treatment excluded volume effects need to be taken into account. Polymers with monomer radius is larger or equal than the persistence length, $\ell_P \leq a$, are well described by the freely jointed chain (FJC). In the simulations, the FJC is again realized with a potential eq. (5.9) where $\tilde{\gamma} = 360$. In the case of $a < \ell_P$, the diffusion constant also depends on the persistence length. Short chains show an ideal behavior; for longer chains excluded volume effects become important. Ideal chains scale as $R_g \sim R_e \sim N^{1/2}$ in the long chain limit where R_g is the radius of gyration and R_e the end-to-end distance, self-avoiding chains as $R_g \sim R_e \sim N^\nu$ with $\nu \approx 0.588$ [32]. For our purpose $\nu = 3/5$ is sufficient.

The prefactors of the diffusion constants of these chains are not analytically known. In the case of the self-avoiding FJC the prefactor will be determined by simulations. For semiflexible chains with $a \ll \ell_P$, the prefactor of the radius of gyration is obtained by matching the FJC value at $\ell_P = a$, see equations (6.7) and (6.10). To derive the diffusion constant, the known

value of the Flory parameter P defined as [51]

$$P = \frac{k_B T}{\sqrt{6} \eta D R_g} \quad (6.3)$$

is used, which relates the diffusion constant to the radius of gyration, and which is assumed to be universal for each class of chains.

The use of the Flory parameter is illustrated in the case of Zimm's *ideal Gaussian chain* with preaveraged hydrodynamic interactions of chapter 5. One finds [32] a diffusion constant of

$$D_{\text{Zimm}} = \frac{4k_B T}{3\sqrt{6} \pi^{3/2} \eta a N^{1/2}} \quad (6.4)$$

which together with $R_g = 2a N^{1/2}/\sqrt{6}$ (note that the Kuhn length is $2a$ and the end-to-end radius is given by $R_e = 2a N^{1/2}$) gives

$$P_{\text{Zimm}} = 3\sqrt{6} \pi^{3/2}/8 \approx 5.11 . \quad (6.5)$$

For an *ideal semiflexible chain* with separated length scales satisfying $a \ll \ell_P \ll L$, one has [189]: $R_g^2 = L \ell_P/3$ and obtains by an explicit calculation on the Zimm level

$$D_{\text{Zimm}}^{\text{wLC}} = \frac{k_B T}{3\pi\eta L} \frac{4}{3} \sqrt{\frac{6}{\pi}} \left(\frac{L}{2\ell_P} \right)^{1/2} . \quad (6.6)$$

This result can also be obtained from eq. (6.4) by replacing the Kuhn length $2a$ by twice the persistence length, $2\ell_P$. The Flory parameter P thus turns out to be the same as in eq. (6.5), as expected based on the universality hypothesis.

In the case of a *self-avoiding freely-jointed chain* obtained in the simulation by setting $\ell_P = 0$ one finds by fitting the prefactor to the asymptotic behavior (see fig. 6.1a):

$$R_g = 0.96 a N^{3/5} , \quad (6.7)$$

Both, hydrodynamic and free draining results are used for the fitting and show no difference as expected for equilibrium properties. The diffusion constant follows from fig. 6.2b as

$$D_{\text{FJC}} = 1.68 \frac{k_B T \mu_0}{N^{3/5}} . \quad (6.8)$$

The last two equations give a Flory parameter $P = 4.8 \pm 0.3$ which is reproduced in fig. 6.1b although the large error bars make the extrapolation $N \rightarrow \infty$ difficult. García Bernal et al. [52] find a value of $P = 5.3 \pm 0.2$ for a FJC with a Lennard-Jones radius slightly larger than the bead radius a using Monte Carlo simulations and rigid-body hydrodynamics, in which the velocity of the chain is calculated from the configuration according to the equations (3.25) and (3.26).

For long *self-avoiding* (SA) semiflexible chains satisfying $a \ll \ell_P \ll L$, one expects more complicated behavior, as the spatial size under good solvent conditions scales as $R_g \sim (a \ell_P)^{1/5} L^{3/5}$ and thus shows a weak dependence on the persistence length [124]. It is obtained from minimizing the free energy \mathcal{F} with respect to the radius R_g :

$$\mathcal{F} \simeq \frac{R_g^2}{\ell_P L} + v_2 R_g^3 \left(\frac{L}{\ell_P R_g^3} \right)^2 \quad (6.9)$$

where the first term is the entropic elastic energy associated with the swelling of the semiflexible polymer chain to a radius R_g and the second term is the second-virial repulsive energy proportional to the (excluded volume) coefficient v_2 , where $v_2 \sim \ell_P^2 a$, and the segment density squared, integrated over the volume R_g^3 [124]. The prefactor is matched with eq. (6.7) for $\ell_P = a$, which corresponds to an effective Kuhn length $2a$,

$$R_g = 0.96/2^{3/5} (a \ell_P)^{1/5} L^{3/5} \approx 0.63 (a \ell_P)^{1/5} L^{3/5}, \quad (6.10)$$

and is consistent with the simulated data (see fig. 6.1a). In fig. 6.1b the Flory parameter P for self-avoiding chains with $\ell_P = 0$ and $\ell_P = 10a$ is presented. For $N \rightarrow \infty$ both chains approach approximately the same value within their error bars. Table 6.1 summarizes the values for the ratios of the three characteristic radii, the end-to-end radius, the radius of gyration, and the hydrodynamic radius, expressed by R_e^2/R_g^2 and P . It is assumed that these ratios are universal for each of the four classes of chains.

The diffusion constant in this asymptotic regime is thus determined by the radius of gyration and scales as $D \sim \mu_0 k_B T (a^4/\ell_P)^{1/5} L^{-3/5}$. To obtain the prefactor D is matched with eq. (6.8) for $\ell_P = a$:

$$D_{SA} = 1.68 \times 2^{3/5} \mu_0 k_B T \frac{a^{4/5}}{\ell_P^{1/5} L^{3/5}} = 2.55 \mu_0 k_B T \frac{a^{4/5}}{\ell_P^{1/5} L^{3/5}}. \quad (6.11)$$

The self-avoidance is only effective above the length L_{SA} which is defined as

$$L_{SA} = \ell_P^3/a^2. \quad (6.12)$$

It is proportional to the square of the inverse excluded volume fraction, $L_{SA} \sim \ell_P (\ell_P^3/v_2)^2$. Below L_{SA} the chain is ideal:

$$R_g = (2\ell_P L/6)^{1/2}. \quad (6.13)$$

The relation is tested in fig. 6.1a for $\ell_P = 10a$ which corresponds to $L_{SA} = 1000a$: The radius of gyration first increases nearly linearly with N as expected for rodlike chains, crosses over to a $R_g \propto N^{1/2}$ behavior for $L \gg \ell_P$, until self-avoidance effects become important for $L \gg \ell_P^3/a^2$. Good agreement with the intermediate ideal regime is visible, the self-avoiding regime is not reached in fig. 6.1a. Using the numerically determined $P = 6.0$ for the ideal FJC [55], the diffusion constant for the *ideal semiflexible chain* in the regime $a < \ell_P$ and $L \ll \ell_P^3/a^2$ is obtained from $R_g = 2a N^{1/2}/\sqrt{6}$ where the prefactor is again given by the matching at $\ell_P = a$:

$$D_{ideal} = 2.22 \mu_0 k_B T \frac{a}{(\ell_P L)^{1/2}}. \quad (6.14)$$

It replaces the estimate eq. (6.6) derived in the preaveraging approximation for a Gaussian chain.

Rod-like chains

In the rod-like case, $L \ll \ell_P$, the numerical result for a cylinder model by Tirado et al. [172] with length L and radius a ,

$$D_{cyl}(L, a) = \frac{k_B T}{3\pi \eta L} \left[\ln \left(\frac{L}{2a} \right) + 0.312 + 0.565 \left(\frac{2a}{L} \right) - 0.1 \left(\frac{2a}{L} \right)^2 \right], \quad (6.15)$$

	ideal Gaussian	ideal FJC	self-avoiding FJC	rod-like	rod with $\mathcal{O}(L/\ell_P)$
R_e^2/R_g^2	6	6	6.4 ± 0.1	12	$12 - 8L/(5\ell_P)$
P	5.11	6.0 ± 0.1	4.8 ± 0.3	0	0

Table 6.1: Theoretical predictions for the squared ratio of the end-to-end radius to the radius of gyration, and the Flory parameter P . The ideal Gaussian chain is Zimm’s preaveraging value [32], the ideal FJC is the Monte Carlo result of [55], and the self-avoiding FJC shows the limiting value of fig. 6.1b. The Flory parameter vanishes logarithmically in the $N \rightarrow \infty$ limit for a rod.

is taken, which is compared with simulations and other numerical and analytical results in appendix B.3. Tirado’s model seems to be best suited to describe short rod-like chains. The radius of gyration is simply

$$R_g = 4\sqrt{3} a N . \quad (6.16)$$

Wormlike chains

Two approximate analytical results for the whole range of flexibility, L/ℓ_P , are presented: Harnau, Winkler and Reineker [65] use preaveraged hydrodynamic interactions and a global inextensibility constraint to derive

$$D = \frac{k_B T}{3\pi\eta L} \left\{ 1 + \sqrt{\frac{6}{\pi}} \int_{2a}^L \frac{L-s}{L\sqrt{f(s)}} e^{-6a^2/f(s)} ds \right\} \quad (6.17)$$

where $f(s)$ is given by

$$f(s) = 2\ell_P s - 2\ell_P^2 [1 - \exp(-s/\ell_P)] \quad (6.18)$$

and is in fact the squared distance of two points with contour length difference s for a given persistence length ℓ_P , in particular $f(L) = R_e^2$. It correctly describes the trend (see fig. 6.2a) and gives $D \sim 1/\sqrt{L}$ for $\ell_P \ll L$, and $D \sim \ln L/L$ for $\ell_P \gg L$, but it has the following shortcomings: The result is not explicit and does not take excluded volume effects into account; the use of the global inextensibility constraint is questionable [87]; and the rod-like limit is only reproduced up to $\sqrt{6/\pi}$.

Yamakawa and Fujii [189] calculate a series expansion for the mean reciprocal distance $\langle 1/R_e(s) \rangle$ between two points along a wormlike cylinder using a preaveraged Oseen tensor both for small and large contour lengths (with respect to the persistence length) and determine the coefficients such that the first and second derivatives with respect to s are the same at $s = 4.556\ell_P$, where s is the contour length difference between these two points. The transition point, $s/\ell_P = 4.556$, also follows from the requirement of the continuity of the first two derivatives and has no further meaning. The diffusion constant is then given by

$$D = \frac{k_B T}{3\pi\eta L} \int_0^L \frac{L-s}{L} \left\langle \frac{1}{R_e(s)} \right\rangle . \quad (6.19)$$

The resulting formula is presented in the appendix B.4. The limiting form for $\ell_P \gg L \gg a$,

$$D(L, a, \ell_P) = \frac{k_B T}{3\pi\eta L} \left[\ln \left(\frac{L}{2a} \right) + 0.386 + \frac{1}{2} \left(\frac{2a}{L} \right) + \frac{1}{12} \left(\frac{L}{\ell_P} \right) \right] , \quad (6.20)$$

is very similar to eq. (6.15) and gives in addition the first order correction for a weakly bending rod. The flexible limit, $\ell_P \ll L$, including the first order corrections in ℓ_P/L is given by

$$D = \frac{4\sqrt{6}k_B T}{9\pi^{3/2}\eta} (2\ell_P L)^{-1/2} \left\{ 1 - \frac{\sqrt{3\pi}}{4} (\ell_P/L)^{1/2} \right\}. \quad (6.21)$$

The main objection is that excluded volume effects are again neglected and that the series is badly converging thus rendering the comparison with experimental results difficult.

Interpolation formula

It is therefore desirable to find a simpler fitting formula for the semiflexible chain even if no physical derivation can be given. It will be useful for the later investigations of the salt dependence. The three regimes, diffusion of rod-like chains, eq. (6.15), ideal flexible chains, eq. (6.14), and swollen flexible chains, eq. (6.11), are included.

In a first step a correction to the rod limit for finite persistence length is presented: A weakly bending rod has an end-to-end distance R_e of $R_e = L[1 - L/(6\ell_P)]$ which follows from eq. (6.18) by expansion with respect to L/ℓ_P . As seen from the last column of table 6.1, the radius of gyration (and thus also the hydrodynamic radius) need not have the same $\mathcal{O}(L/\ell_P)$ correction to the rigid rod limit. Only in the limiting case $\ell_P \rightarrow \infty$, the radius of gyration and the diffusion constant can be directly inferred from the end-to-end distance. A qualitative understanding of the correction term $L/(12\ell_P)$ in eq. (6.20) is possible from the following argument: The diffusion constant is approximately given by the Kirkwood hydrodynamic radius [32], $D \sim \sum \langle 1/r_{ij} \rangle / N^2$, where r_{ij} is the distance between the two frictional elements i and j . Neglecting discretization and end effects this amounts to calculating (see also eq. (6.17))

$$D \sim \frac{1}{L^2} \int (L-s) \left\langle \frac{1}{r_s} \right\rangle ds \sim \frac{1}{L^2} \int \frac{L-s}{s} ds + \frac{1}{L^2} \int \frac{L-s}{6\ell_P} ds \quad (6.22)$$

where $\langle 1/r_s \rangle \sim 1/f(s) \approx [1 - s/(6\ell_P)]/s$ has been used (cf. eq. (6.18)). The first term gives the usual rod limit, while the second gives, integrated from zero (or the small distance cutoff) to L , a term of $L/(12\ell_P)$. It is precisely the $\mathcal{O}(L/\ell_P)$ term in eq. (6.20). This motivates the following modification of Tirado's formula, eq. (6.15), for weakly bending rods (WBR):

$$D_{\text{WBR}} = \frac{k_B T}{3\pi\eta L} \left[\ln \left(\frac{L}{2a} \right) + 0.312 + 0.565 \left(\frac{2a}{L} \right) - 0.1 \left(\frac{2a}{L} \right)^2 + \frac{1}{12} \left(\frac{L}{\ell_P} \right) \right]. \quad (6.23)$$

The interpolation between the ideal and swollen flexible regimes is done on the level of the (exact) hydrodynamic radius R_D , defined by

$$R_D = \frac{k_B T}{6\pi\eta D}, \quad (6.24)$$

which should be distinguished from the Kirkwood hydrodynamic radius R_h , eq. (5.11), that is just an approximation to it. In the flexible regime this interpolation reads

$$R_D^{(\text{flex})} = 0.45 (\ell_P L)^{1/2} \left[1 + 0.25 \frac{v_2}{\ell_P^3} \left(\frac{L}{\ell_P} \right)^{1/2} \right]^{1/5} = 0.45 (\ell_P L)^{1/2} \left[1 + 0.5 \left(\frac{L}{L_{\text{SA}}} \right)^{1/2} \right]^{1/5} \quad (6.25)$$

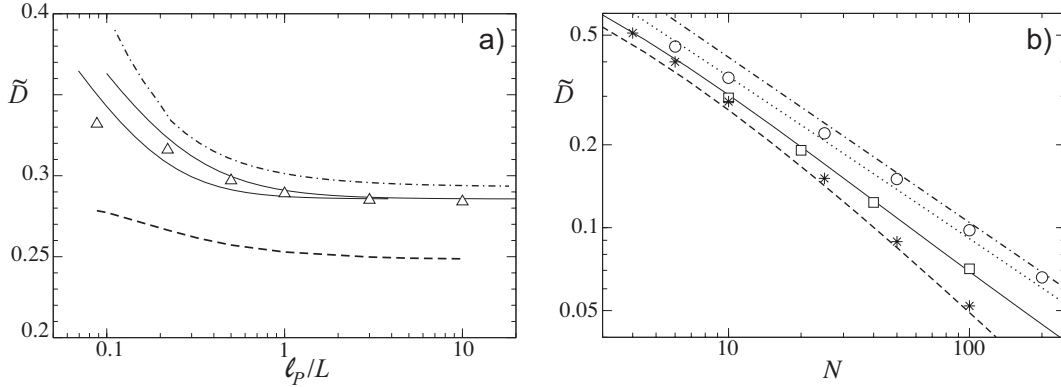


Figure 6.2: a) Simulation of a neutral $N = 10$ chain with $\tilde{\gamma} = 360$ (triangles) compared with the predictions of Yamakawa et al., eq. (6.20) (dotted-dashed), Harnau et al., eq. (6.17) (dashed line), and the interpolation, eq. (6.30), with $\alpha = 3$ or $\alpha = 4$, respectively (upper and lower solid lines). b) Neutral chains with $\tilde{\gamma} = 360$: Flexible ($\ell_P = 0$, circles), semiflexible ($\ell_P = 10a$, squares) and stiff chains ($\ell_P/L = 5$, stars). Respective theoretical predictions: D_{FJC} , eq. (6.8), (dotted-dashed line); D_{flex} , eq. (6.29), with $\ell_P = a$ (dotted line); D_{int} , eq. (6.30), with $\ell_P = 10a$ and $\alpha = 3$ (solid line); and D_{cyl} , eq. (6.15), (dashed lines).

where L_{SA} is defined in eq. (6.12) and v_2 is the second virial coefficient of the excluded volume interactions that is given by [124]

$$v_2 = \ell_P^2 2a. \quad (6.26)$$

The interpolated radius of gyration and end-to-end radius read

$$R_g = 3^{-1/2} (\ell_P L)^{1/2} \left[1 + 1.59 \left(\frac{L}{L_{\text{SA}}} \right)^{1/2} \right]^{1/5} \quad (6.27)$$

$$R_e = \sqrt{2} (\ell_P L)^{1/2} \left[1 + 1.87 \left(\frac{L}{L_{\text{SA}}} \right)^{1/2} \right]^{1/5}. \quad (6.28)$$

In the limits $L/L_{\text{SA}} \rightarrow 0$ and $L/L_{\text{SA}} \rightarrow \infty$, the diffusion constant D_{flex} given by

$$D_{\text{flex}} = \frac{k_B T}{6\pi\eta R_D^{\text{flex}}} = 2.22 \mu_0 k_B T (\ell_P L)^{-1/2} \left[1 + 0.5 \left(\frac{L}{L_{\text{SA}}} \right)^{1/2} \right]^{-1/5} \quad (6.29)$$

reduces to D_{SA} , eq. (6.11), and D_{ideal} , eq. (6.14), respectively.

Surprisingly, the simple heuristic expression

$$D_{\text{int}}(\ell_P/L) = (D_{\text{cyl}}^\alpha + D_{\text{flex}}^\alpha)^{1/\alpha} \quad (6.30)$$

that interpolates on a logarithmic scale between the flexible, eq. (6.29), and the rod limit, eq. (6.15), gives a good description of the Brownian dynamics data (see solid lines in fig. 6.2). α is a fit parameter for which $\alpha = 3$ turns out to give good numerical agreement. If not otherwise mentioned, $\alpha = 3$ is chosen.

Fig. 6.2a shows a comparison of the predictions of Yamakawa et al., eq. (B.38) and (B.39), and Harnau et al., eq. (6.17), together with the interpolation formula, eq. (6.30), for $\alpha = 3$

and $\alpha = 4$. Simulation results for $N = 10$ show the validity of the choice of α . $\tilde{\gamma}$ is chosen large enough that the influence of the stretching on the diffusion is small; $\tilde{\gamma} = 360$ seems to be sufficient.

In fig. 6.2b, the persistence length ℓ_P is fixed ($\ell_P = 0$, $\ell_P = 10a$ and $\ell_P = 5L$, respectively), and the length N is changed. The transition from a $\ln N/N$ to a $N^{-3/5}$ behavior is well reproduced. It can also be seen that D_{FJC} describes the simulation data for flexible chains only from a certain length onward while D_{Cyl} already includes corrections for short chains. Also D_{flex} introduces corrections for short flexible chains. Although no physical insight can be gained from such a fit, it is quite helpful to separate electrolyte friction from the effects on D due to conformational changes. It can be used to obtain an effective total persistence length (including electrostatic stiffening).

6.2 Salt dependence of polymer diffusion

6.2.1 Method of investigation

As before, the time evolution of the charged system is modeled by a Langevin equation

$$\dot{\mathbf{r}}_i(t) = \sum_{j=1}^{2N+2N_s} \mu_{ij}(|\mathbf{r}_i - \mathbf{r}_j|) \left[-\nabla_{\mathbf{r}_j} U(\{\mathbf{r}_k\}) + \mathbf{h}_j \right] + \boldsymbol{\xi}_i(t) \quad (6.31)$$

with the main difference that the constant external field \mathbf{h}_j only acts on the monomers, $\mathbf{h}_j = h \hat{\mathbf{e}}_z$ for $j < N$ and zero otherwise. Comparison with eq. (6.2) gives $F_G = N h$. Eq. (6.2) is much more convenient than eq. (6.1) from a numerical point of view. The potential U consists again of an elastic, a Lennard-Jones and an electrostatic part. The screening length κ^{-1} includes $2N_s$ salt and N counterions:

$$\frac{\kappa}{a} = \left(\frac{4\pi \zeta (N + 2N_s)}{(B/a)^3} \right)^{-1/2} \quad (6.32)$$

and is varied by changing the box size B , keeping N_s approximately constant. Except for very low salt concentrations, B is well above κ^{-1} . The coupling parameter ζ is defined in eq. (2.26).

In fig. 6.3 it is checked that the external field $\tilde{h} = 0.05$ is small enough that the fraction of bound counterions ϕ , defined as the fraction of counterions that are within a distance of $2a$ to a monomer, and the mean orientation ψ do not deviate much from their limiting values, and that the inferred diffusion constant D is close to its limiting value at $h \rightarrow 0$. At very low salt concentrations (fig. 6.3a) the counterion distribution, which is here characterized by ϕ , is sensitive to even small fields h . But in that case D is not very dependent on the form of the counterion cloud any more and already close to the limiting diffusion constant at zero salt concentration D_0 . The overestimation will therefore be small. Further checks were made for the radius of gyration R_g and the current divided by the sedimentation field,

$$\sigma = \sum_i s_i \dot{z}_i / h \quad (6.33)$$

where the sum runs over all particles and $s_i = \pm 1$.

The time step $\tilde{\Delta}$ is chosen of the order of 10^{-3} . It is also important to check the box size dependence, which is a measure for the semidiluteness of the polymer solution. It has

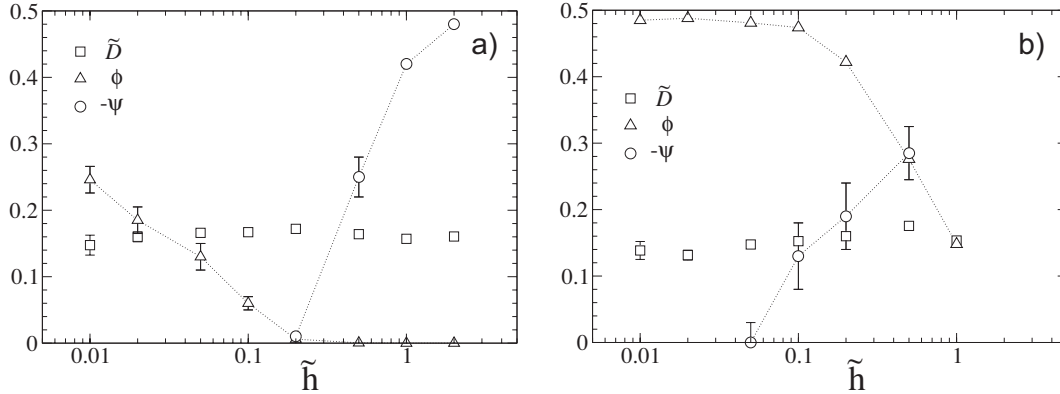


Figure 6.3: Test of the linear response regime for $N = 20$, $N_s = 40$ and $\ell_P/L = 10$ by looking at the field dependence of the rescaled diffusion constant \tilde{D} , the fraction of bound counterions ϕ and the mean orientation ψ . a) Low salt conditions ($\kappa^{-1}/L = 224.1$). b) High salt ($\kappa^{-1}/L = 0.238$). Except for the fraction of close counterions ϕ in a) $\tilde{h} = 0.05$ seems to be a sensible value.

been shown [115, 184] that even small volume fractions can markedly affect the diffusion. In fig. 6.6a, the diffusion constant and rescaled current $\tilde{\sigma}$ is plotted against the box size B for $\tilde{\kappa}^{-1} = 126.9$ showing that the condition $B > 2\kappa^{-1} + L$ is often already sufficient to obtain results characteristic for the infinite-box-size limit.

6.2.2 Charged spheres

Most of the analytical work for salt-dependent diffusion has been done for charged colloidal spheres with [16, 80, 129] and without [29, 114, 115, 159] hydrodynamic interactions. The free-draining results were also extended to spheroids [3, 176]. Schurr [159], and Medina-Noyola and coworkers [29, 114] calculate approximately the fluctuating electrostatic force of the small ions on the central sphere in the free draining case. The different approximation schemes in these calculations are summarized in [29]. They all agree that D equals its value for an uncharged sphere at very high and very low salt concentrations but has a minimum at $\kappa^{-1} \approx R$ where R is the radius of the sphere. Booth [16] and Ohshima [129] use a hydrodynamic continuum ansatz starting with a diffusion equation for the small ions, the Stokes equation for the fluid and the Poisson equation, and solve the coupled set of partial differential equation for small sedimentation velocities. In the limit of small surface charges one finds for the diffusion constant divided by its value for a neutral sphere, denoted by D_0 [16, 56]

$$\frac{D}{D_0} \equiv \left[1 + \Delta\zeta_{\text{el}} \frac{D_0}{k_B T} \right]^{-1} = \left[1 + \frac{Z^2 \ell_B a_i}{12R^2} f_B(\kappa R) \right]^{-1} \quad (6.34)$$

where Z and R are the valency and radius of the colloidal sphere, and a_i is the hydrodynamic radius of the small ions, which are assumed to be equal in valency and size. $\Delta\zeta_{\text{el}}$ is termed *electrolyte friction*. The dimensionless function

$$f_B(x) = \frac{1}{(1+x)^2} \left(\frac{1}{5}x^2 - \frac{1}{2}x + \frac{3}{2} - \frac{21}{4}x^{-1} - \frac{39}{2}x^{-2} \right)$$

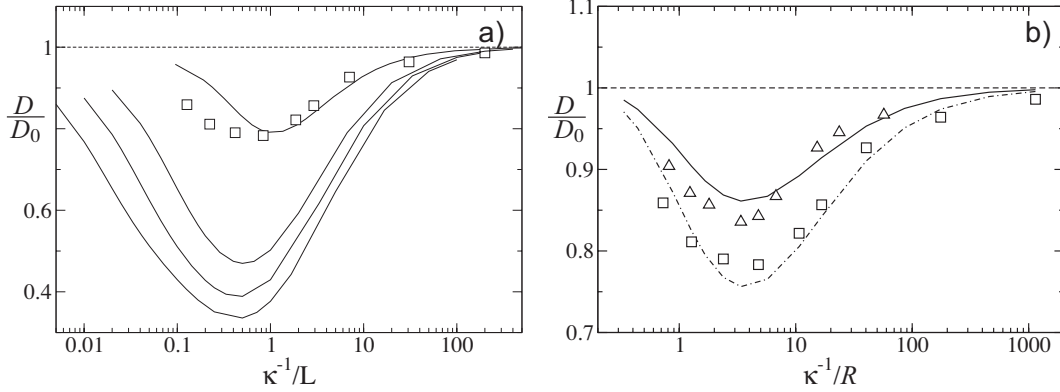


Figure 6.4: Isotropic elastic rod with $N = 10$ and $\ell_P = 5L$. a) Simulations with $\zeta = 5$ (squares) and analytical results (6.40 - 6.42) for $N = 1, 5, 10$ and 20 (solid lines from top to bottom). b) Simulations with coupling parameters $\zeta = 5$ (squares) and $\zeta = 2.5$ (triangles) compared with eq. (6.44) with $f = 0.5$ in both cases. The equivalent radius is given by eq. (6.43).

$$\begin{aligned}
& + \frac{2}{3} \left[\frac{1}{16} x^3 (x^2 - 12) T(x) + \frac{2}{3} (1 + x^{-1}) \right]^2 \\
& + \frac{1}{15} x^2 (4x^5 - 90x + 180) T(2x) \Big) \quad (6.35)
\end{aligned}$$

with

$$T(x) = x^{-1} - x^{-2} + 2x^{-3} - 6x^{-4} - e^x \int_x^\infty \frac{e^{-t}}{t} dt \quad (6.36)$$

displays a bell-like curve on a log-linear scale with a maximum of $f_B \approx 0.1$ at $\kappa R \approx 0.3$. The width of the curve is about one decade. $\Delta\zeta_{el}$ is much smaller than in the treatments of Schurr and Medina-Noyola et al. As pointed out in [56, 161] these two approaches are in some sense complimentary.

This point could be further clarified by Nägele and coworkers [80, 113] using a mode-coupling approximation including both Rotne-Prager level hydrodynamic interactions and fluctuating electrostatic forces. Their result is close to the formula of Booth, eq. (6.35), which means that the influence of the direct fluctuating forces on the electrolyte friction is greatly reduced by the hydrodynamic interactions. Experiments [157] seem to support their results up to a certain degree, showing that the approximations made in the derivation (lowest order mode-coupling, Debye-Hückel electrostatic interactions) are still quite strong.

For $\kappa R \ll 1$, the Onsager limiting behavior

$$f_B(\kappa R) \sim \kappa R \quad (6.37)$$

is recovered by Booth's dimensionless function; in the opposite limit $\kappa R \gg 1$ one finds

$$f_B(\kappa R) \sim \kappa^{-4}. \quad (6.38)$$

In the non-hydrodynamic theory of Schurr the salt dependence of D can also be expressed in the form of eq. (6.34) but with a different function

$$f_S(x) = \frac{1}{x} \left(1 - [1 + 2x] e^{-2x} \right) \quad (6.39)$$

which shows the same $\kappa R \ll 1$ asymptotics, but $f_S(\kappa R) \sim \kappa^{-1}$ in the limit $\kappa R \gg 1$. In the following it is investigated whether this behavior can also be found for non-spherical objects, especially for semi-flexible polymers.

6.2.3 Rod-like polymers

The method of Medina-Noyola et al. can be extended to prolate ellipsoids [3, 176] by treating parallel and perpendicular friction separately. In the bead model of this thesis the ratio of the major semiaxis $a_>$ to the minor semiaxis $a_<$ is given by N . Denoting by $\gamma = 1$ the perpendicular and by $\gamma = -1$ the parallel case, and defining $c_N = \sqrt{N^2 - 1}$ the following expressions for the electrolyte friction coefficients are obtained [176]:

$$\Delta\zeta_{\text{el}}^{\gamma} = \frac{6\pi\eta a_i Z^2 \ell_B}{12a_>} \frac{3N}{4\kappa a_<} \int_0^1 du \frac{1 + \gamma + u^2(1 - 3\gamma)}{1 + (c_N u)^2} \left(1 - \left[1 + 2\kappa a_< \sqrt{1 + (c_N u)^2} \right] e^{-2\kappa a_< \sqrt{1 + (c_N u)^2}} \right). \quad (6.40)$$

With the salt-free friction coefficients [139]

$$\zeta_0^{\gamma} = \frac{16\pi\eta(N^2 - 1) a_>}{\left[N^2(3 - \gamma) - \frac{1}{2}(5 + \gamma) \right] N (N^2 - 1)^{-1/2} \ln(N + \sqrt{N^2 - 1}) - \frac{1}{2}(1 - 3\gamma)N^2} \quad (6.41)$$

one finally gets

$$\frac{D}{D_0} = \frac{2 \left[\zeta_0^{\perp} + \Delta\zeta_{\text{el}}^{\perp} \right]^{-1} + \left[\zeta_0^{\parallel} + \Delta\zeta_{\text{el}}^{\parallel} \right]^{-1}}{2/\zeta_0^{\perp} + 1/\zeta_0^{\parallel}}. \quad (6.42)$$

where the notation $\zeta^{(1)} = \zeta^{\perp}$ and $\zeta^{(-1)} = \zeta^{\parallel}$ is used. In the bead model, $a_i = a_< = a$ and $a_> = Na$, and therefore $\mu_0 = 1/(6\pi\eta a_i)$.

The simulations are done with $N = 10$ monomers and $N_s = 40$ pairs of salt ions. The persistence length is chosen $\ell_P = 5L$ with $L = 2a(N-1)$. Due to the electrostatic contribution to the persistence length [104, 127, 163] this is sufficient for the polymers to be rod-like. An isotropic elastic medium is assumed, eq. (3.6). Fig. 6.4 shows the rescaled diffusion constant D/D_0 as a function of the rescaled screening length. Starting at infinite dilution (of polymer and salt concentration) D decreases until $\kappa^{-1} \approx L$ and then begins to increase again. The simulation data are rescaled with the cylinder value of eq. (6.15), i.e. $D_0 = D_{\text{cyl}}$. In fig. 6.4a the $\zeta = 5$ result is compared with the prolate ellipsoid model (6.40 - 6.42) for aspect ratios $N = 1, 5, 10$ and 20 . A qualitatively similar trend in κ can be seen, but the minimum is much too deep. Even an improved treatment [3] does not alleviate this disagreement. As already announced for spherical objects, hydrodynamics seem to be essential for a proper description of electrofriction. The theory of Schurr and Medina-Noyola is therefore discarded in this work. It is interesting to note that according to their results the influence of electrofriction gets stronger for larger aspect ratios.

Since no hydrodynamic theory for non-spherical objects is available the rod-like polymer is treated as an effective sphere with equivalent radius R which is derived from the cylinder model eq. (6.15),

$$R = \frac{1}{6\pi\eta D_{\text{cyl}}}, \quad (6.43)$$

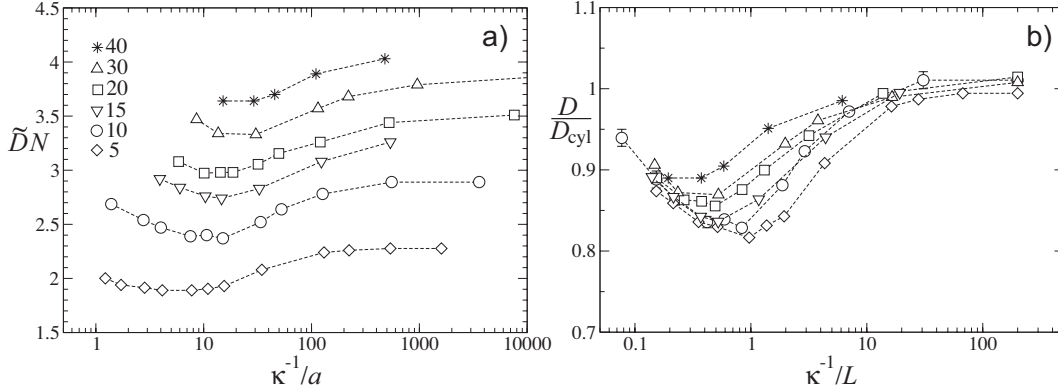


Figure 6.5: a) Diffusion constant (multiplied by N for better visibility) as a function of screening length for several N . Parameters: $\ell_p/L = 0.22$, $\gamma = 120 k_B T/a$ and $\zeta = 5$. Most of the time $N_s = 40$ is used, and $\tilde{\kappa}^{-1}$ changed by varying the box size. b) Same data but D measured in multiples of D_{cyl} , eq. (6.15), and $\tilde{\kappa}^{-1}$ in multiples of L . Error bars are - if not shown - of the order of the symbol sizes.

and compared with the theory of Booth which in rescaled units reads

$$\frac{D}{D_0} = \left[1 + \frac{f \zeta N^2 (a_i/a) f_B(\kappa R)}{12 \tilde{R}^2} \right]^{-1}. \quad (6.44)$$

Here, f is a fit parameter to account for the non-sphericity. The factor a_i/a is included in case that the effective radius of the small ions, a_i , is different from the monomer radius. In the simulations, $a_i = a$ always holds. Reasonable matching with the simulation data can be achieved with $f = 0.5$ for both $\zeta = 5$ and $\zeta = 2.5$. The trends in κ and ζ as well as the position of the minimum seem to be correctly described; the dependence of f on the various parameters needs of course further investigation.

6.2.4 Semiflexible polymers

In the last section it was checked that many features of the ionic strength dependence of diffusion also apply to non-spherical rigid objects. I will now move to the main topic of the chapter, the diffusion of slightly semiflexible polymers. The motivation for this is an experiment with 394 bp DNA strands conducted by J. Bayer at the LMU München [8, 154]. Assuming a bare DNA persistence length of 30 nm and a rise per base pair of 0.34 nm one finds

$$\ell_P = 0.22 L. \quad (6.45)$$

Electrostatic effects on the persistence length that lead to $\ell_P \approx 50$ nm under physiological conditions are taken into account explicitly since all monomers and ions are charged. Since DNA is approximately isotropic elastic [165] a relation like eq. (3.6) seems at first to be appropriate. But due to the finite external field h and the repulsive Lennard-Jones potential this would lead to contour length fluctuations by more than 20% and strongly affect the mobility of the chain. For this reason γ was arbitrarily set to the value

$$\gamma = 120 k_B T/a \quad (6.46)$$

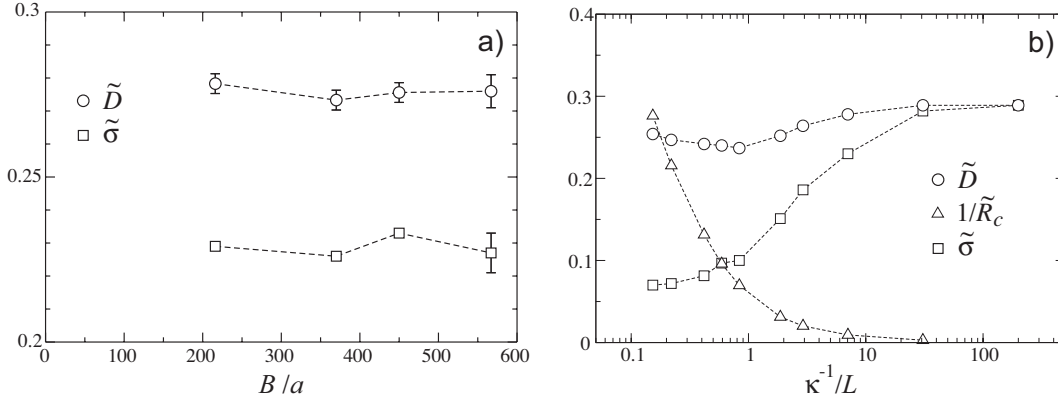


Figure 6.6: $N = 10$ chain with $\tilde{\gamma} = 120$ and $\ell_P = 0.22 L$; $\zeta = 5$. a) Test of the box size dependence for $\kappa^{-1} = 7.05 L$. b) Qualitative explanation of the minimum: \tilde{D} (circles), $1/\tilde{R}_c$ (triangles) and $\tilde{\sigma} = \sigma/(N \mu_0)$ (squares).

at which D starts to become independent of γ for the chain lengths under investigation, $N \leq 40$.

Fig. 6.5a shows the result of such a simulation. As before $\tilde{D} \equiv D/(k_B T \mu_0)$. For $\kappa^{-1}/a < 1$ the system becomes very dense due the finite ion sizes so that hard core repulsion becomes the dominant interaction. Hence, this region cannot be investigated. For better comparison of the various curves, D is rescaled with the diffusion constant of a cylinder, eq. (6.15), which is a good reference value at low salt even for the persistence lengths chosen, since charges increase the effective persistence length. The diffusion constant D exhibits a shallow minimum at a screening length intermediate between monomer size a and polymer length L . As seen in fig. 6.5b, the rescaling results in a collapse of the curves for large and small $\tilde{\kappa}^{-1}/L$ but does not completely eliminate the N -dependence of the position and depth of the minimum. I attribute this mainly to the fact that increasing N while keeping L constant not only changes the aspect ratio of the polymer but also its total charge, since we keep

$$\zeta = \frac{z^2 \ell_B}{a} = 2z \tau \ell_B = 5. \quad (6.47)$$

τ is the linear charge density along the chain and z the valency of the ions and monomers. In principle one needs three different ζ parameters, one for monomer-monomer, for monomer-ion and for ion-ion interactions. If one considers the interaction between the monomers and the counterions the most relevant then for DNA and monovalent ions one gets $\zeta = 8.2$ which is close enough to the chosen one. Writing $Z = Nz$, the total charge of the polymer, one finds

$$Z = \sqrt{\frac{\zeta L}{2\ell_B}} N \quad \text{and} \quad z = \sqrt{\frac{\zeta L}{2\ell_B N}}. \quad (6.48)$$

Hence, one cannot fix the total polymer charge and the valency of the small ions at the same time within this approach. N is therefore more than just a discretization of the chain with given length L . On the other hand, present day computers make it nearly impossible to simulate the correct number of ions even for our short 394 bp strand. More than qualitative agreement cannot be expected.

What is the mechanism behind this decrease of D ? Fig. 6.6b shows for $N = 10$ the diffusion constant as well as the rescaled current $\tilde{\sigma} = \sigma/(N\mu_0)$, and the root mean square radius R_c of the N counterions which are closest to the polymer (and which form the neutralizing counterion cloud). At the evaluation times, for every counterion i the distance r_{ij} to its nearest monomer j is determined. The counterions are sorted with respect to r_{ij} so that

$$R_c = \left\langle \sum_{i=1}^N r_{ij}^2 \right\rangle^{1/2}. \quad (6.49)$$

At infinite dilution of ions, i.e. $\tilde{\kappa}^{-1} \gg L$, the current equals the diffusion constant, $\sigma/(N\mu_0) = \tilde{D}$, in other words, the number of counterions that are dragged along with the polymer goes to zero and the diffusion becomes quasi-free. The decrease of the current for decreasing screening length indicates coupling of counterion motion to polymer motion, resulting in increased hydrodynamic drag and thus a decrease of diffusivity. Upon further decrease of the screening length, $1/\tilde{R}_c$, which is a measure for the hydrodynamic mobility of the neutralizing counterion cloud, starts to increase. The polymer diffusion constant depends on both the fraction of counterions dragged along and the hydrodynamic mobility of the neutralizing cloud. The minimum occurs when the two competing effects are of the same order. For very high salt concentration, the counterion cloud collapses around the polymer, and the polymer diffusivity almost approaches the bare polymer value (modulo the effective increase of the polymer radius due to adsorbed ions).

It may seem at first surprising that not all counterions are moving with the rod, even in the linear response limit. It is checked that this is not an artifact due to finite box size, i.e. finite polymer concentration (see fig. 6.6a). It appears that - depending on κ - only a part of the counterion cloud is bound strongly enough to the polymer such that it will follow its motion if a small perturbation h is applied.

The dependence of σ on κ^{-1}/L deserves some comments: The simulation corresponds to a semi-dilute polymer solution where the volume fraction is determined by B . The system is let to equilibrate before a small external perturbation in form of the field \mathbf{h} is applied to the polymer. During the relaxation to the new stationary state only some finite fraction $\alpha(\kappa)$ of the N counterions, which would neutralize the polymer, follow its motion. The rest is left behind. The ion cloud is nevertheless only slightly distorted as salt ions continuously stream around the polymer. For a finite box size some positive charge (if the counterions are assumed to be positive) will re-enter the box from the opposite side. This leads in the reference frame of the moving polymer to a non-zero flux of positive ions in the negative \mathbf{h} -direction, which seems unphysical for very dilute polymer solutions. This effect of course disappears in the limit $B \rightarrow \infty$. It turns out that is has a negligibly small effect even for the box sizes chosen (see fig. 6.6a).

This transient finite current that persists until the polymer has settled to the bottom of the sedimentation vessel - the polymer plus its co-moving counterions are not charge-neutral - can also be expected from Onsager's reciprocity relations [85]:

$$\begin{aligned} j_{\text{el}} &= L_{11} E + L_{12} h \\ j_{\text{pol}} &= L_{21} E + L_{22} h. \end{aligned} \quad (6.50)$$

j_{el} is the electric current, j_{pol} the mass current of the polymer, which is proportional to its velocity, and L_{11} etc. are constant coefficients with $L_{12} \propto L_{21}$. Since L_{21} is proportional to the electrophoretic mobility also the induced current from the sedimentation cannot be zero.

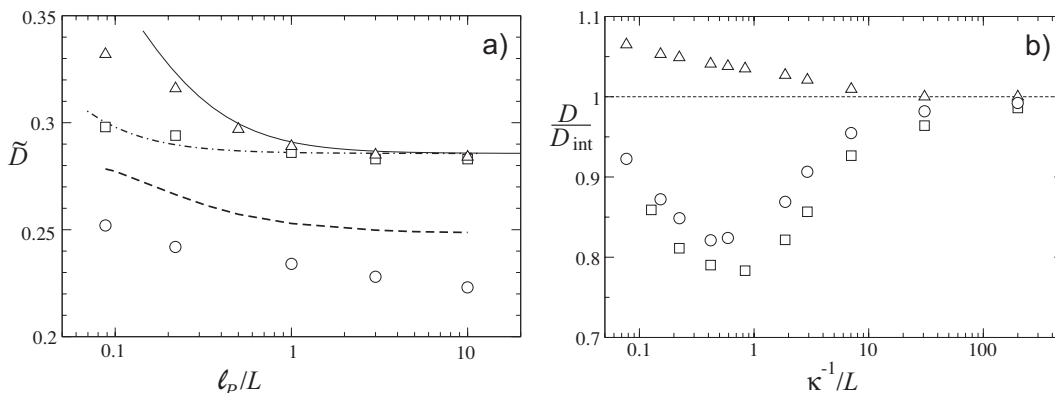


Figure 6.7: Diffusion for $N = 10$. a) ℓ_P/L dependence for neutral ($\kappa^{-1} \rightarrow \infty$, $\zeta = 0$ and $\tilde{\gamma} = 360$; triangles) and charged polymers ($\kappa^{-1} \rightarrow \infty$, $\zeta = 5$ and $\tilde{\gamma} = 360$; squares) at zero salt concentration, as well as close to the minimum ($\kappa^{-1}/L = 0.42$, $\zeta = 5$ and $\tilde{\gamma} = 120$; circles). The solid and the dotted-dashed lines are eq. (6.30) with $\alpha = 3$, in the second case an effective persistence length of $5.5 \ell_P$ is used. The dashed line is again eq. (6.17). b) D/D_{int} at $\zeta = 5$ for $\ell_P/L = 5$ (squares) and $\ell_P/L = 0.22$ (circles) - data taken from fig. 6.4a and fig. 6.5b - compared with the inverse (Kirkwood) hydrodynamic radius divided by its limiting value $1/R_h^0$ for $\kappa^{-1} \rightarrow \infty$, R_h^0/R_h , of the $\ell_P/L = 0.22$ data set (triangles).

The analysis neglects of course configurational changes of the semiflexible and slightly extensible polymer: The counterions very close to the polymer screen the electrostatic repulsion between the charged monomers and lead to an increased coiling of the polymer chain that raises D slightly. Nevertheless, configurational changes of the chain do not dominate the dependence of D on $\tilde{\kappa}^{-1}$ at $\ell_P/L = 0.22$ since the curves for rods (fig. 6.4b) and semiflexible chains (fig. 6.5b) are quite similar. The rescaled diffusion at $\kappa^{-1}/L = 0.42$, which is approximately the minimum of $D(\kappa^{-1}/L)$, shows only a slight decrease with ℓ_P/L (fig. 6.7a, circles). At vanishing ionic strength, a similar trend is observed (squares). Since electrostatic stiffening makes the chain more rod-like, also the $\zeta = 0$ case (triangles) is shown together with the interpolation eq. (6.30). The limiting cylinder behavior (6.15) is reached within a few percent. The dotted-dashed line is the same interpolation with an effective persistence length of $5.5 \ell_P$. The effective persistence length is merely a fit parameter to obtain closed-form solutions for charged chains at zero salt which will be used in fig. 6.7b. One can see that the correction for the flexibility at zero salt is in fact rather small for $\ell_P/L = 0.22$; this is the reason why in fig. 6.5 and fig. 6.8 the established D_{cyl} is used for the rescaling.

How much of the decrease of D/D_0 can be attributed to electrolyte friction and what is due to bending? Fig. 6.7b plots again the diffusion constants already shown in fig. 6.4a and fig. 6.5b for $N = 10$ and $\zeta = 5$, but in this case rescaled by D_{int} with $\alpha = 3$ and an effective persistence length of $5.5 \ell_P$. By this procedure, chains with different persistence lengths are much easier compared. Also shown is the relative increase of the inverse (Kirkwood) hydrodynamic radius R_h with respect to its numerically determined limiting value at $\kappa^{-1} \rightarrow \infty$. In the preaveraging approximation, the inverse hydrodynamic radius $1/R_h$ is a measure of the diffusion constant influenced by the configuration of the polymer alone. Adding salt therefore gives rise to two effects which cancel each other partially, electrolyte friction and coiling. This also shifts the minimum slightly.

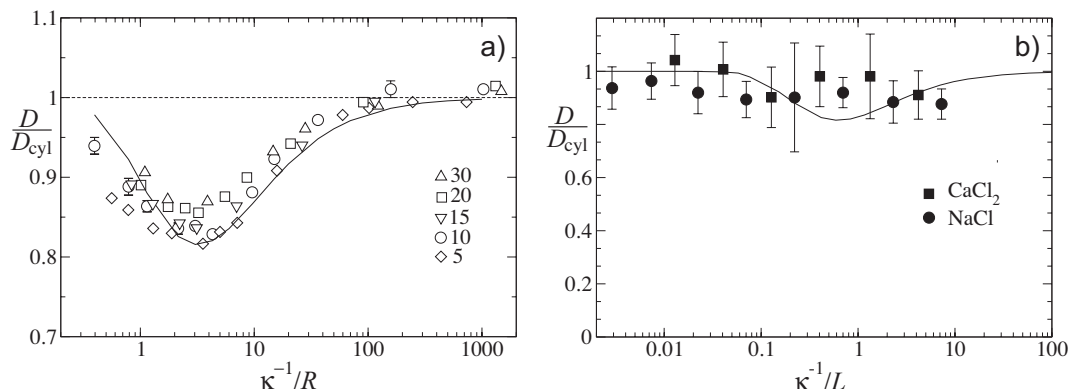


Figure 6.8: a) Data of fig. 6.5 but rescaled with R , eq. (6.43). The solid line is the fit function eq. (6.51) with $f_1 = 5.3$. b) Experimental data for 394 bp DNA [154] in mono- and divalent salt solution compared with the fit function of a). For the rescaling a rise per base pair of 0.34 nm and an effective diameter of 3.49 nm is used.

It might be useful to have a fit function for the semiflexible polymer diffusion. Instead of fitting to an equivalent sphere, eq. (6.44), and using the approximations of Booth as done in fig. 6.4, a simple fit function is presented which gives the same asymptotic behavior, eq. (6.37) and eq. (6.38), as well as the position of the minimum:

$$\frac{D}{D_0} = \left[1 + \frac{f_1 \zeta(a_i/a)}{12} \frac{\kappa R}{(1 + f_2 \kappa R)^5} \right]^{-1}. \quad (6.51)$$

The high exponent of 5 is a result eq. (6.38). The minimum of $x/(1 - f_2 x)^5$ occurs at $x = 1/(4f_2)$ which fixes $f_2 \approx 0.8$ to give Booth's position of the minimum. One fitting parameter remains: $f_1 = 5.3$ if fitted to $N = 10$ and $\ell_P/L = 0.22$ (cf. fig. 6.8). f_1 has only a small N dependence. It can also be seen that rescaling with R instead of L gives a better collapse of the minima but a different $\kappa^{-1} \rightarrow 0$ behavior.

6.3 Discussion and comparison with experiments

Among the plethora of measurements of the diffusion constant of semiflexible polymers there are only few that consider both, systematically varying the ionic strength and measuring at very low polymer concentration. Dynamic Light Scattering (DLS) experiments have mainly probed the semidilute polymer regime [126, 177]; extrapolating these results to infinite dilution gave at most a small ionic strength dependence for rod-like polymers. Using Fluorescence Correlation Spectroscopy (FCS) [8, 71, 184] or the stopped migration method in capillary electrophoresis [169, 170], polymer self-diffusion constants in very high dilution could be determined.

Diffusion of semiflexible polymers

Fig. 6.8b shows the diffusion constant of a 395 bp DNA fragment with a covalently bound dye determined by FCS (data taken from [154]) for two types of salt, NaCl and CaCl₂. The

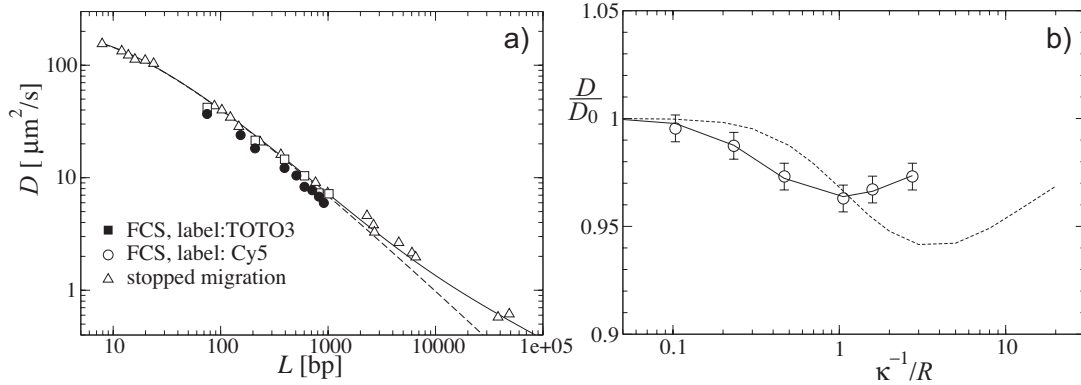


Figure 6.9: a) Diffusion data of [8] for intercalating and covalently labeled DNA (squares and circles) as well as data of [170] (triangles) compared with the cylinder prediction, eq. (6.15) (dashed line), and the interpolation formula, eq. (6.30) (solid line). b) Rescaled TMV diffusion data [158] fitted to eq. (6.51) (solid line) and compared with eq. (6.44) (dashed line).

statistical errors of the experiment are too large to resolve a systematic variation of D with ionic strength. Nevertheless, an upper bound of approximately 10% to this variation can be given, consistent with the theoretical result of eq. (6.51).

Fig. 6.9a displays the diffusion constant of double-stranded DNA as function of the number of base pairs. Squares and circles are FCS measurements at an ionic strength of 75 mol/l [8], triangles are obtained from the stopped migration method [170] at an ionic strength of 40 mol/l. The values for DNA labeled with a covalently bound dye are slightly lower owing to the larger hydrodynamic diameter which is estimated by 3.49 nm. To compare experimental and theoretical results, a rise per base pair of 0.34 nm, a diameter of 2 nm and an effective persistence length of $\ell_p = 50$ nm is assumed. The dashed line is again the cylinder prediction, eq. (6.15), the solid one the interpolation formula eq. (6.30). Reasonable agreement with fig. 6.2b is obtained.

Rod-like macromolecules

The only systematic measurement for rod-like macromolecules I am aware of is that for tobacco mosaic virus (TMV) by Schumacher and van de Ven [158]. They extrapolated DLS results to infinite dilution and changed the KCl concentration over a range of two decades. Their data are shown in fig. 6.9b with error bars indicating reproducibility within 95% confidence. They fitted their experimental results with the theory of Vizcarra-Rendón et al. [176], eq. (6.40), using the TMV charge Ze as adjustable parameter. Although the data can be described very well by this curve, the fitted κ -dependent charge, the maximal value of which is $120e$, is much too low as they admit. It is checked whether the data can instead be described with Booth's theory using an equivalent sphere, eq. (6.44). For the TMV a length of $L = 300$ nm, a diameter of 15 nm, an effective charge of $Z = 415$ [158] is assumed, and for the ions an effective radius of $a_i = 0.2$ nm. An equivalent radius of the macroion of $R = 45$ nm is calculated using eq. (6.43). The fit parameter f accounting for the non-sphericity should be of the order of one and is set $f = 0.5$ as in the simulations. The resulting curve (dashed line) is not able to describe the experimental data. Especially the experimental minimum

occurs at $\kappa^{-1} \approx R$. This is surprising since spheres can be well described by Booth's formula where the minimum occurs at $\kappa^{-1}/R \approx 3$ [157]. The data points are also parametrized by eq. (6.51) with $f_1 = 0.116$ and $f_2 = 0.253$ (solid line). Summarizing one can say that the non-hydrodynamic theories overestimate the magnitude while the hydrodynamic ones, which only exist for spheres so far, predict a wrong position of the minimum. Nevertheless, Booth's theory cannot be ruled out completely since the DLS diffusion data are obtained indirectly by extrapolation and contain large error bars. Further measurement would be required.

Flexible polymers

Polylysine diffusion was investigated by DLS [159] and FCS [71]. In the first case, D/D_0 decreases from one at 1 mol/l NaCl to zero at 0.01 mol/l, in contradiction to the FCS measurements. The DLS data were explained by electrofriction in which case the polymer coil was represented by a charged permeable gel sphere. In the FCS experiment a minimum is seen at $\kappa^{-1} \approx R_g$ but the authors did not consider electrofriction.

Conclusions

No theory exists so far that can satisfactorily describe the salt dependence of semiflexible or even rod-like polymers. The only analytical treatment of prolate objects I am aware of is that presented in section 6.2.3. Simulations may provide an alternative although Brownian dynamics quickly reach their limits due to the great number of small ions required for a realistic treatment. As pointed out in [174], page 78, much more papers have concentrated on the secondary effect of double layers on the *concentration dependence* of diffusion coefficients, than on the primary effect which double layers have on isolated particles. The last chapter collects different approaches to electrofriction as well as experimental results that are scattered around the literature and attempts to extract common features that could be used in a heuristic description of semiflexible polyelectrolyte diffusion. Simulation were carried out to test the speculations. Nevertheless a unified description is still missing.

Chapter 7

Electrophoresis of Charged Rods

The last chapter of this work deals with external electric fields and thereby completes the problem of chapter 3 where rod-like particles in an external field were investigated under the neglect of electrostatic interactions. It is organized as follows: In the first part effects which are first order in the electric field E are discussed. The field-induced parallel and perpendicular components of the dipole moment of the polymer including its counterion cloud are determined as a function of polymer length, salt and polymer concentration with and without hydrodynamic interactions. The second part deals with the orientation of the rods resulting from the distortion of the ion cloud. Here I concentrate on the Kerr limit, i.e. on effects quadratic in E . It will be contrasted with the hydrodynamical orientation mechanism of chapter 3. Special emphasis is paid to anomalous birefringence which is usually caused by a perpendicular orientation of the rod-like particles with respect to the electric field. Five scenarios in which anomalous birefringence might be caused by hydrodynamic orientation are presented: High electric fields, very low and very high salt concentrations, overlapping counterion clouds in semi-dilute polymer solutions, and high aspect ratios $L/(2a)$. Limitations of the system size make some of the analysis indirect: A decrease of the polarizability will often be interpreted as a sufficient hint for anomalous birefringence without actually showing that perpendicular orientation occurs, which in many cases is unfeasible with present-day computers. In some extreme cases, nevertheless, a direct observation of the transition to anomalous birefringence is presented.

The emphasis of the first part is on the mechanism that leads to the observed dielectric increment, i.e. the change of the frequency dependent dielectric constant of the polymer solution with respect to the pure salt solution, by induced dipoles and to electric birefringence and dichroism. Electric birefringence is the difference of the refractive index between two beams in the directions parallel and perpendicular to the electric field, electric dichroism the difference of the absorbance. Existing models are presented and extended. Experiments are discussed together with the simulation results where three main open questions encountered in the literature are tackled: Is the dependence of the polarizability α on the rod length given by L^3 or a smaller power law [190]? How does the salt concentration [89] and polymer concentration [81] affect the results? Is birefringence mainly an effect of the condensed counterions or of the dilute counterion cloud [89]? The second part deals with complications of this simple picture and concludes with a discussion for both parts.

7.1 Polarizabilities of ion clouds

Polarizabilities of aqueous polymer solutions are conventionally measured by dielectric spectroscopy [17, 19]. It amounts to determining the impedance at frequencies from the kHz regime up to several GHz from which the complex permittivity is obtained. While the high-frequency range (GHz) is dominated mainly by the orientation of the water molecules it is believed that at intermediate (1-100 MHz) and low frequencies “free” counterions may play an important role [17, 103]. The dielectric increment at low frequencies is often associated with “bound” counterions [135] where of course the distinction between “free” and “bound” counterions needs some clarification. The explanation of the polarization mechanism is by far not conclusive [17] which can be seen from the great number of recent publications dealing with the subject [39, 89, 179]. Electric birefringence and dichroism provide another method to determine polarizabilities. In this case the polarizability is obtained only indirectly from the mean orientation of the particles, and the results are sometimes complicated by other processes.

In the following I will concentrate on the stationary case, i.e. the low frequency limit. The modulation of the electric field $E(t)$ is assumed to be slow enough for all double layer processes to have relaxed and to attain a stationary state, but fast enough to avoid electrical breakdown at high voltages; in the simulation the electric field is just constant.

7.1.1 Method of investigation and definitions

The Langevin equation (2.22) together with the potential eq. (2.23) and (3.3) is the general starting point. The elastic parameters γ and ε are always large enough to assure that the chains are rod-like, usually $\ell_P = 10L$. The dimensional parameters are rescaled as in equations (3.8-3.11) where now

$$q = ze. \quad (7.1)$$

If E points in z -direction then the dipole moment and the polarizability are defined as

$$\mathbf{P} = \sum_i s_i ze \mathbf{r}_i \quad (7.2)$$

$$\alpha = \lim_{E \rightarrow 0} \sum_i s_i ze \frac{\mathbf{r}_i \cdot \mathbf{E}}{E^2}. \quad (7.3)$$

The sum runs over all monomers and ions. The definition is independent of the origin of the coordinate system since the total system is neutral. Rescaling P by $ze a$ and α by $4\pi\epsilon\epsilon_0 a^3$ gives

$$\tilde{\mathbf{P}} = \sum_i s_i \tilde{\mathbf{r}}_i \quad (7.4)$$

$$\tilde{\alpha} = \zeta \sum_i s_i \frac{\tilde{\mathbf{r}}_i \cdot \tilde{\mathbf{E}}}{\tilde{E}^2} \quad (7.5)$$

where $\tilde{\mathbf{E}} = qEa/(k_B T)$. Note the extra factor of ζ in $\tilde{\alpha}$. The motivation for this rescaling is that $\tilde{\mathbf{P}}$ is just a convenient auxiliary variable measuring the displacement of charge while $\tilde{\alpha}$ is compared with experiments for which reason is it useful to remove the implicit dependence on the ion valencies.

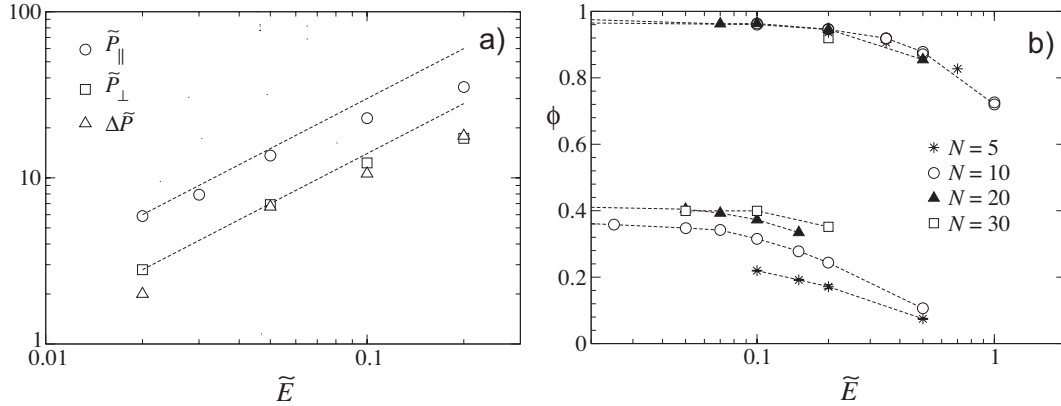


Figure 7.1: a) Linear response regime for $N = 10$ rod with $N_s = 10$, $\tilde{B} = 54.3$ and $\zeta = 5$, i.e. $\tilde{\kappa}^{-1} = 9.2$. The lines have slope unity. b) E -field dependence of the fraction of bound counterions ϕ : Upper set of curves show $\tilde{\kappa}^{-1} = 7.98$, $\zeta = 20$ and $N_s = 0$, i.e. $43 \leq \tilde{B} \leq 78.3$ depending on N ; lower set of curves same parameters except $\tilde{\kappa}^{-1} = 15.96$ and $\zeta = 5$.

α_{\parallel} and α_{\perp} denote the polarizabilities of a system where the long axis of the rod \mathbf{R}_e is fixed parallel or perpendicular to the electric field. The orientation of the rod due to this induced dipole mechanism is just of the order $\mathcal{O}(E^2)$ in the limit of $E \rightarrow 0$. Hence, at small fields the particles are randomly oriented and thus

$$\alpha = \frac{1}{3}(\alpha_{\parallel} + 2\alpha_{\perp}). \quad (7.6)$$

To calculate α_{\parallel} and α_{\perp} one could determine at each sampling time the components of \mathbf{P} and \mathbf{E} parallel and perpendicular to \mathbf{R}_e and divide them by each other, e.g. $\alpha_{\parallel} = P_{\parallel}/E_{\parallel}$. It turns out that the statistics are too bad to make this procedure feasible. On the other hand, fixing the rod in space requires virtual forces that hydrodynamically influence all particles in the system, i.e. inverting a $N \times N$ matrix every time step (see section 4.2), which is also hardly possible for long rods with the workstations available. I will therefore use a third alternative. The rod is free to orient but the electric field follows its motion. $\mathbf{E}(t)$ is either parallel to $\mathbf{R}_e(t)$ or in that direction perpendicular to it that lies in the x - y plane:

$$\mathbf{E}_{\parallel}(t) = E \frac{\mathbf{R}_e(t)}{R_e(t)} \quad (7.7)$$

$$\mathbf{E}_{\perp}(t) = E \frac{(R_{e,y}, -R_{e,x}, 0)}{\sqrt{R_{e,x}^2 + R_{e,y}^2}}. \quad (7.8)$$

This method is especially efficient for long rods which have long orientational diffusion times $\tau_D \propto L^3$. It is always checked that for the separately measured α , α_{\parallel} and α_{\perp} eq. (7.6) holds within ten percent. As before the rod length is defined as $L = 2a(N - 1)$.

Fig. 7.1a shows the range of the linear response regime, where $P \propto E$ holds, for the example of $N = 10$ and $N_s = 10$ with rescaled box size $\tilde{B} = 54.3$. Relevant for birefringence is the difference

$$\Delta\mathbf{P} = \mathbf{P}_{\parallel} - \mathbf{P}_{\perp} \quad (7.9)$$

$$\Delta\alpha = \alpha_{\parallel} - \alpha_{\perp}. \quad (7.10)$$

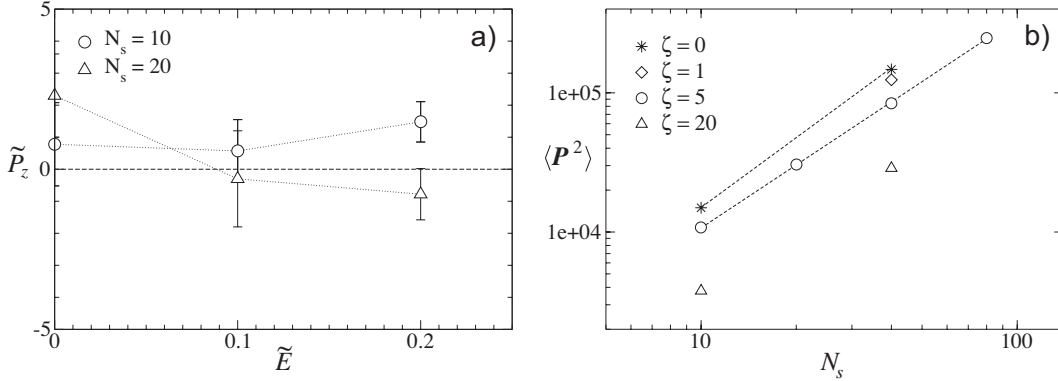


Figure 7.2: a) Dipole moment in field direction of a pure salt solution, i.e. $N = 0$, for 10 and 20 pairs of salt ions at $\zeta = 5$ and box size $\tilde{B} = 54.3$. p_z is zero within error bars. b) Equilibrium average of P^2 , cf. eq. (7.13), for pure salt solution of concentration $N_s/\tilde{B}^3 = 6.25 \times 10^{-5}$. The dashed lines are power law fits with slopes $3/2$ and $5/3$, respectively.

which is also shown. The range of the linear response turns out to be κ -dependent; more extended clouds are more easily destroyed. For each set of parameters at least three \tilde{E} -values are simulated to be sure to probe the linear regime and to estimate the error. Usually 10^7 to 10^8 steps with a rescaled time step $\tilde{\Delta}$ of the order of 10^{-3} are needed to get reasonable accuracy.

For the later investigations I define the "close layer" of counterions as the set of all counterions that lie within a cutoff distance of $4a$ to the polymer center line. These counterions will also be called "bound" later on and their number be denoted by N_b . This is a more neutral term than "condensed" which refers to Manning's counterion condensation [110]. The fraction of bound counterions, i.e. the fraction of neutralized charge on the polyion, is denoted

$$\phi = \frac{N_b}{N} \quad (7.11)$$

and gives a characterization of the double layer. ϕ decreases with \tilde{E} as seen in fig. 7.1b giving another upper limit of the linear response regime. The dipole moment containing only those ions and the polymer,

$$\tilde{\alpha}^b = \zeta \sum_i s_i (\mathbf{r}_i - \mathbf{R}_{CM}) \cdot \frac{\tilde{\mathbf{E}}}{\tilde{E}^2}, \quad (7.12)$$

depends on the origin chosen, which is in this case the center of mass of the polymer, \mathbf{R}_{CM} , since the polymer-condensed ions complex is not neutral.

The polarizability can also be determined at equilibrium using the fluctuation-dissipation theorem [88]:

$$\tilde{\alpha} = \frac{\zeta}{3} \langle \tilde{P}^2 \rangle. \quad (7.13)$$

Fig. 7.2a shows the dipole moment of a pure salt solution ($N = 0$) at small values of the electric field. As a result of the minimal image boundary conditions the dipole moment is zero within error bars. Simulating a polymer solution it is often a good check for the error of the dipole moment to redo the simulation with a pure salt solution and the same random numbers. The

mean square dipole moment of a pure salt solution is plotted for several coupling parameters ζ (fig. 7.2b). For a non-interacting gas ($\zeta = 0$) of constant density one expects a scaling

$$\langle \mathbf{P}^2 \rangle \sim N_s B^2 \sim N_s^{5/3}. \quad (7.14)$$

It can be understood as a random walk with N_s steps of the center-of-mass position of the positive particles with respect to center of mass of the negative particles, where the step size is of the order of the box size B . Since the particles are non-interacting the steps are independent of each other. The dipole moment \mathbf{P} is the sum of all steps, so that its mean square displacement is given by eq. (7.14). For interacting particles ($\zeta > 0$) in a dilute solution the exponent is slightly smaller, $\langle \mathbf{P}^2 \rangle \sim N_s^{1.5}$. Since the background zero-field polarizability (of the salt) is quite high, calculating the (excess) polarizability of the polymer solution via eq. (7.13) at zero field amounts to subtracting two large numbers and renders this method impractical. I therefore use finite fields. In the salt-free case, however, it was successfully used in a recent Monte Carlo study [179].

If the rod has different *optical polarizabilities* parallel and perpendicular to its long axis then the birefringence Δn_θ at an angle $\theta = \arccos[\mathbf{R}_e \cdot \mathbf{E}/(R_e E)]$ is related to the saturation birefringence Δn_s of complete orientation by [48]

$$\Delta n_\theta = \Delta n_s \psi \quad (7.15)$$

where $\psi = 3 \cos^2 \theta / 2 - 1/2$, as in the chapter 3. With the energy of the induced dipoles in the electric field

$$U = \frac{1}{2} \Delta \alpha E^2 \cos^2 \theta \quad (7.16)$$

the mean birefringence is given by

$$\Delta n = \Delta n_s \frac{\Delta \alpha E^2}{15 k_B T}, \quad (7.17)$$

which follows from integrating eq. (7.15) over all orientations with a Boltzmann weight determined by eq. (7.16). Defining a *modified Kerr* constant by

$$K' = \lim_{E \rightarrow 0} \frac{\Delta n}{\Delta n_s E^2} \quad (7.18)$$

one finds

$$\Delta \alpha = 15 k_B T K' = 15 k_B T \lim_{E \rightarrow 0} \frac{\psi}{E^2} \quad (7.19)$$

or in rescaled units

$$\Delta \tilde{\alpha} = 15 \tilde{K}' = 15 \zeta \lim_{\tilde{E} \rightarrow 0} \frac{\psi}{\tilde{E}^2} \quad (7.20)$$

where $\tilde{K}' = K' k_B T / (4\pi \epsilon \epsilon_0 a^3)$. The wavelength and saturation birefringence dependence have been included in the definition of K' as these quantities are outside the scope of this investigation. $15 \tilde{K}'$ may have other contributions than $\Delta \tilde{\alpha}$, e.g. hydrodynamic orientation.

7.1.2 Analytical calculations

Overview of existing work

Several models have been presented to explain the large induced dipole moment of elongated polyelectrolytes in solution. Schwarz [160] and later Mandel [102] considered the longitudinal movement of counterions bound to the rod-like molecule. Mandel's model is a one-dimensional rod of length L to which the counterions are confined, together with a weak periodic potential coming from discrete charges of the monomers. Applying an external electric field and using Boltzmann statistics he obtains

$$\alpha_{\text{Mandel}}^{\parallel} = \frac{N_b (ze)^2 L^2}{12k_B T} = 4\pi\epsilon\epsilon_0 \zeta \frac{N_b a L^2}{12}. \quad (7.21)$$

N_b is the number of “bound” counterions as above. Interactions between the counterions are neglected. If $N_b \propto N = L/2a$ then the polarizability is proportional to the cube of the rod length. This L^3 -dependence seems to be a general feature of systems with tightly bound counterions where L is the relevant length scale, and will also be reproduced in the following analysis.

Oosawa [135] calculated the equilibrium counterion density fluctuation along a one-dimensional rod to obtain the mean square dipole moment. If U_k is the k th Fourier mode of the counterion interaction potential the polarizability reads

$$\alpha_{\text{Oosawa}}^{\parallel} = 4\pi\epsilon\epsilon_0 \zeta N_b a L^2 \frac{1}{2\pi^2} \sum_{k=0}^{\infty} \frac{1}{k^2} \left[1 + \frac{N_b U_k}{2k_B T} \right]^{-1} \quad (7.22)$$

which reduces to Mandel's result in the limit of $U_k \rightarrow 0$ (since $\sum_k 1/k^2 = \pi^2/6$). Due to the factor $1/k^2$ only the long-wavelength modes contribute significantly. For weak interactions the power law is thus unchanged.

The above theories are incomplete insofar that they use the number of bound counterions N_b as an input. Manning [107] used counterion condensation theory to fix N_b . He also calculated a correction factor to eq. (7.21) for finite κ . Since in his result, α_{\parallel} decreases with decreasing κ , which is contrary to the experiments [89] I am going to describe, his approach will not be further pursued. In a later publication Mandel and co-workers [175] used a two-state model which allows exchange between the bound and unbound counterions with a rate constant K . It predicts a cross-over from $\alpha_{\parallel} \sim L^3$ for weak exchange to $\alpha_{\parallel} \sim l^2 L$ for very strong exchange in which case the new length scale l is given by

$$l = \sqrt{\mu_0 k_B T / K} \quad (7.23)$$

where μ_0 is the counterion mobility.

To include the ionic strength dependence on a more systematic level Rau and Charney [147] investigated a thin long cylinder with counter- and coions using the Smoluchowski equation for both species and the Debye-Hückel approximation. The resulting $\alpha_{\parallel}(L, \kappa, a)$ is presented in form of a Fourier series which becomes independent of the diameter for $a \rightarrow 0$. For $a \ll L < \kappa^{-1}$ they numerically find $\alpha_{\parallel} \sim L^{1.85} \kappa^{-1.15}$, and $\alpha_{\parallel} \sim L \kappa^{-2}$ for $a \ll \kappa^{-1} \ll L$. But as criticized in [109] they mix terms of different order of the electric potential. Nevertheless, the result shows the importance of including the ion cloud.

For completeness the result of Fixman [41] valid for thin double layers is also presented. For monovalent counter- and coions the polarizability parallel to the rod axis is

$$\alpha_{\text{Fixman}}^{\parallel} = 4\pi\epsilon\epsilon_0 \frac{C(L, a) L}{2\gamma^2} \left[1 - \frac{\tanh(\gamma L/2)}{\gamma L/2} \right] \quad (7.24)$$

where

$$C(L, a) = \frac{3}{2} [2 \ln(2L/a) - 7]^{-1} \quad (7.25)$$

and

$$\gamma = [4\pi C(L, a) L c_s / N_b]^{1/2} . \quad (7.26)$$

The formula has been specialized to the case of excess salt with concentration c_s . Depending on γL , the length dependence crosses over from L^3 to L . In a later paper Fixman and Jagannathan [43] tried to relax the thin double layer approximation using a variational method [42]. They included the convective polarization coming from the relative electrophoretic motion of the macroion with respect to the small ions and tabulated their numerical results. They conclude that the outer parts of the ion cloud which are very susceptible to convective effects give the dominant contribution to the polarizability unless $L \gg \kappa^{-1}$.

Among the more recent results are Manning's linear analysis (in E and the electric field of the macroion) [109] and the work by Mohanty and Zhao [117] which is an extension of Mandel's result. Manning's motivation was to get some understanding of the underlying physics in Fixman's numerical analysis by linearizing the fields and ion fluxes but it turned out that the convection-free polarizability is isotropic within this linear analysis contrary to the expectation that it should be much larger parallel to the long axis of the rod than perpendicular. Higher order terms are thus necessary for a proper description.

It is also worth mentioning some simulation results. Yoshida et al. [190] used a Metropolis Monte Carlo method to calculate the counterion distribution of a fixed rod neglecting hydrodynamic interactions and salt ions. They showed that their method is equivalent to Brownian dynamics for a constant external electric field so that they could obtain the polarizability from the relation $\alpha = P/E$. Bound and free counterions are distinguished by a cutoff distance from the rod. One of their main results is that at constant counterion concentration (varying the cell size) $\alpha_{\parallel} \propto L^3$ holds, while at constant cell size (increasing the counterion concentration with L) the polarizability $\alpha_{\parallel}(L)$ seems to saturate when L is increased. The polarizability coming just from the polymer plus bound counterions is always proportional to the cube of the length irrespective of the cell size. No explanation for this behavior could be given.

Washizu and Kikuchi also used Monte Carlo simulations to calculate the equilibrium fluctuations of the dipole moment to obtain the polarization tensor. They propose a criterion to define bound or "condensed" counterions which yield fractions of condensed counterions for short DNA strands that are close to Manning's prediction [179]. It will be discussed in section 7.1.5. α_{\parallel} and α_{\perp} decrease with increasing polymer concentration. For the molecular weight dependence only three rod lengths were investigated; the somehow tentative results are: $\alpha_{\parallel} \propto L^2$ and $\alpha_{\perp} \propto L$. Adding salt to the solution results [178] in a decrease of the anisotropy

$$\Delta\alpha = \alpha_{\parallel} - \alpha_{\perp} . \quad (7.27)$$

Despite the voluminous literature on this subject it fair to say that many issues are still only partly understood.

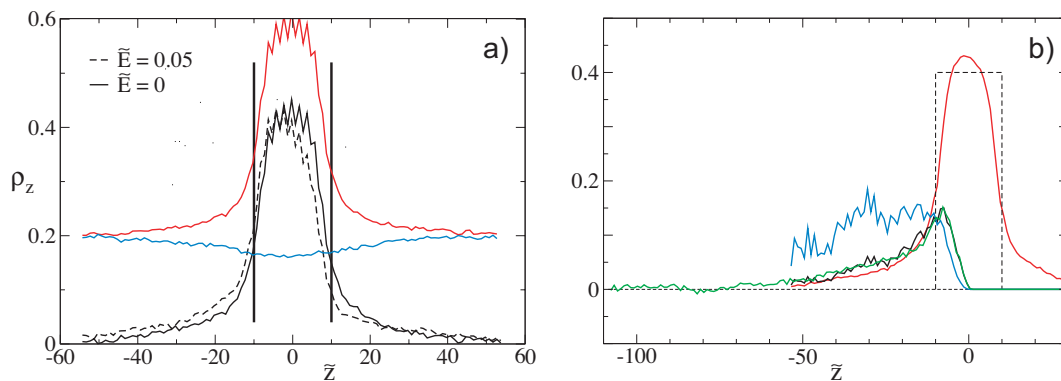


Figure 7.3: a) Vertical density of counterions (red) and coions (blue), and total charge density $\rho_z(z)$ (black) at equilibrium (solid lines) and at a $\tilde{E} = 0.05$ (broken line) within free-draining. The $N = 10$ polymer is fixed at the center of the cell (which has the dimensions $54.3a \times 54.3a \times 108.6a$) with its long axis in the z -direction. $\tilde{\kappa}^{-1} = 10.1$ corresponding to $\zeta = 5$ and $N_s = 20$. The two vertical bars at $\tilde{z} = \pm 10$ show the extension of the polymer. b) Charge density (red, after a low pass filter to reduce the noise), $\Delta\rho_z$ (black) and $-\Delta\rho_z z$ (blue) for the system on the left at $\tilde{E} = 0.01$. The dashed lines mark the position of the polymer. The green line shows $\Delta\rho_z$ for a cell with dimensions $54.3a \times 54.3a \times 217.2a$ but the same $\kappa = 10.1$.

One-dimensional continuum model

A simple model is presented that gives α_{\parallel} and α_{\perp} as a function of L , a and κ^{-1} . It is not attempted to derive it from fundamental equations which has already been done twenty years ago [41, 43] but did not yield explicit results. Hydrodynamic interactions and electrophoretic motion are not taken into account.

Guidance is sought from *free-draining* (FD) Brownian dynamics simulations in which the rodlike polymer is fixed at the center of the simulation cell with its long axis either parallel or perpendicular to the external field

$$\mathbf{E} = E \hat{e}_z . \quad (7.28)$$

Virtual forces to fix the polymer are unnecessary within FD; the polymer motion need not be simulated and acts merely as a boundary condition. Fig. 7.3a shows the vertical densities, defined as the number of particles per z -interval, for the counterions and coions for a rod with $\mathbf{R}_e \parallel \hat{e}_z$ and $\zeta = 5$. The charge density divided by the ion valency, ρ_z , is just the difference of these two densities. The origin of the coordinate system is placed at the center of mass of the polymer. As expected, the coion density is lower and the counterion density higher than their respective bulk values at the cell boundary. The simulation box has a lateral extension of $B = 54.3a$ so that most of the ions in $[-10a; 10a]$ are not in close vicinity of the rod. The charge density decays exponentially with z for $|z| > 10a$. A small electric field of $\tilde{E} = 0.05$ slightly shifts $\rho_z(z)$ without destroying the ion cloud. ρ_z can be directly used to calculate the total dipole moment as done in fig. 7.3b. Since at non-zero E , ρ_z increases for $z < 0$ and decreases for $z > 0$ with respect to its equilibrium value at $E = 0$ it is useful to define

$$\Delta\rho_z(z) = \rho_z(z) - \rho_z(-z) , \quad (7.29)$$

which is the contribution to the charge asymmetry at a given $|z|$. Integration gives the total

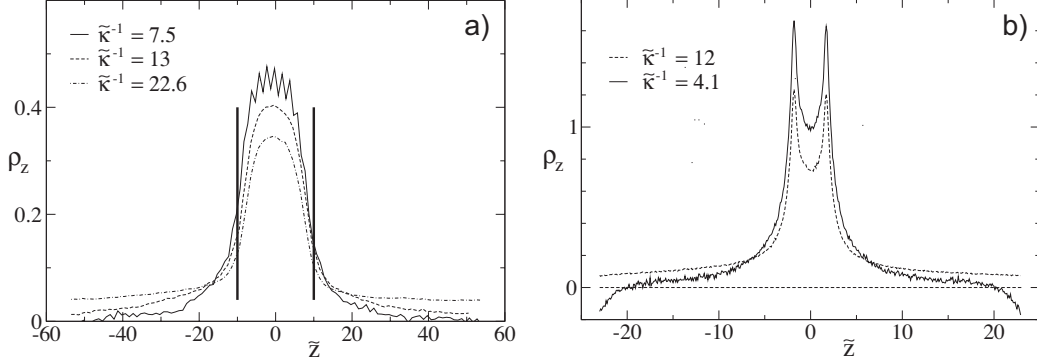


Figure 7.4: a) Charge density in the free-draining case at $\tilde{E} = 0.01$ for $N = 10$, $\zeta = 5$ and a box as in fig. 7.3 for different screening lengths (corresponding to $N_s = 0, 10$ and 40). The long axis of the rod is *parallel* to the field. b) $N = 10$ rod *perpendicular* to \mathbf{E} in a $46a \times 46a \times 46a$ cell with $N_s = 0$ and $N_s = 40$.

dipole moment of the cell,

$$\tilde{P} = - \int_{-\tilde{B}}^0 \Delta\rho_z(\tilde{z}) z d\tilde{z}. \quad (7.30)$$

$\Delta\rho_z$ is shown for two different box sizes but the same screening length $\tilde{\kappa}^{-1}$ (black and green lines; $\Delta\rho_z$ is only defined for $z < 0$). Both lines lie nearly on top of each other indicating that there is no appreciable box size dependence. $\Delta\rho_z$ follows the trend of ρ_z (red line). It is maximal at the ends of the rods as already predicted in [147]. The increment of the dipole moment at $|z|$ is given by $-\Delta\rho_z(z) z$ (blue line). It is greatest at a certain distance away from the polymer although the polymer is highly charged ($\zeta = 5$), underlining the importance of the diffusive double for the polarizability. Fluctuations at large $|z|$ have a great impact on P as they are multiplied by z ; this makes the simulation of the $B \rightarrow \infty$ limit numerically very demanding.

The influence of the screening length for a given box size is presented in fig. 7.4 for parallel and perpendicular orientation of the rod to \mathbf{E} . ρ_z attains a finite value at the cell boundary for salt-free solutions; adding salt continuously decreases this value to zero. For small systems even accumulation of coions at the boundary are possible with a strong influence on the box size dependence of the dipole moment.

To partially mimic the above charge distribution and - at the same time - get simple power law results the following form of $\rho(z)$ in the *parallel* case for small E is assumed:

$$\rho_z(z) = \rho_z^0(z) + \lambda z \quad \text{for } |z| < \frac{L}{2} + \frac{3}{2} \kappa^{-1} \quad (7.31)$$

and zero otherwise. ρ_z^0 is the distribution at zero field and λ a small parameter proportional to E . This means that $\Delta\rho_z$, which first linearly increases for $|z| < L/2$ and then exponentially decreases (see fig. 7.3b), is replaced by just a linear function but over a wider range, $\Delta\rho_z(z) = 2\lambda z$. The reason for using $3\kappa^{-1}/2$ instead of κ^{-1} as the extension of the ion cloud is arbitrary. In principle any number of the order of κ^{-1} is as good within this scaling model but it turns out that the additional factor of $3/2$ gives a better comparison with the data. A calculation for a more realistic form of ρ_z has also been done but the result, beside being more complex, did not yield further insight.

The most severe assumption is probably that a truly one-dimensional interaction potential is taken,

$$U_i = k_B T \frac{\zeta a}{2} \iint \frac{\rho_z(z) \rho_z(z')}{|z - z'|} dz dz' . \quad (7.32)$$

The integrals extend over the whole space except that the region $|z - z'| < a$ is excluded. The energy gain in the electric field is

$$U_E = -qE \int z \rho_z(z) dz . \quad (7.33)$$

q is the charge of an ion since ρ_z is just a number density. Plugging in eq. (7.31) and minimizing $U_i + U_E$ with respect to the distortion parameter λ gives to lowest order in a/L

$$\lambda = \frac{3qE}{2k_B T \zeta a} \left[3 \ln \left(\frac{1}{a} (L + 2\kappa^{-1}) \right) - 7 \right]^{-1} , \quad (7.34)$$

and thus

$$\alpha_{\text{ID}}^{\parallel} = -q \int z(\lambda z) dz = 4\pi\epsilon\epsilon_0 \frac{1}{8} \frac{(L + 2\kappa^{-1})^3}{3 \ln [(L + 2\kappa^{-1})/a] - 7} . \quad (7.35)$$

In the derivation the symmetry arguments

$$\int \rho_z^0(z) z dz = 0 \quad \text{and} \quad (7.36)$$

$$\left[\frac{d}{d\lambda} U_i \right]_{\lambda=0} = 0 \quad (7.37)$$

are used, which mean that only the interactions between the perturbations of the density by the electric field are relevant for the polarizability. The equilibrium charge distribution ρ_z^0 is unimportant. Eq. (7.35) is justified only for long rods, $L \gg a$, and thin double double layers since otherwise the lateral dimension becomes important, and an one-dimensional model becomes dubious.

So far κ^{-1} only entered in the extension of the ion cloud. It could also affect the inter-particle potential directly:

$$U_i' = k_B T \frac{\zeta a}{2} \iint \frac{\rho_z(z) \rho_z(z') e^{-\kappa|z-z'|}}{|z - z'|} dz dz' . \quad (7.38)$$

The same method as above leads in the limit $\kappa L \gg 1$ to

$$\alpha_{\text{ID},r}^{\parallel} \approx 4\pi\epsilon\epsilon_0 \frac{L^3}{24 \text{Ei}(-2a\kappa)} \quad (7.39)$$

where Ei is the exponential integral function. Hence, strong screening does not change the approximate cubic length dependence. In the limit $a \ll \kappa^{-1} \ll L$, the exponential integral function gives a logarithmic dependence of $\alpha_{\text{ID},r}^{\parallel}$ on κa , while in eq. (7.35) the parallel polarizability depends on $\log(L/a)$ in the same limit.

In the *perpendicular* case, the long axis of the rod is placed in x -direction, the field again in z -direction, and the origin is the center of mass. A two-dimensional charge density (number per area) of the following form is assumed:

$$\rho_{xz}(x, z) = \rho_{xz}^0(x, z) + \lambda' z \quad \text{for } |z| < a + \kappa^{-1} \text{ and } |x| < L/2 + \kappa^{-1} \quad (7.40)$$

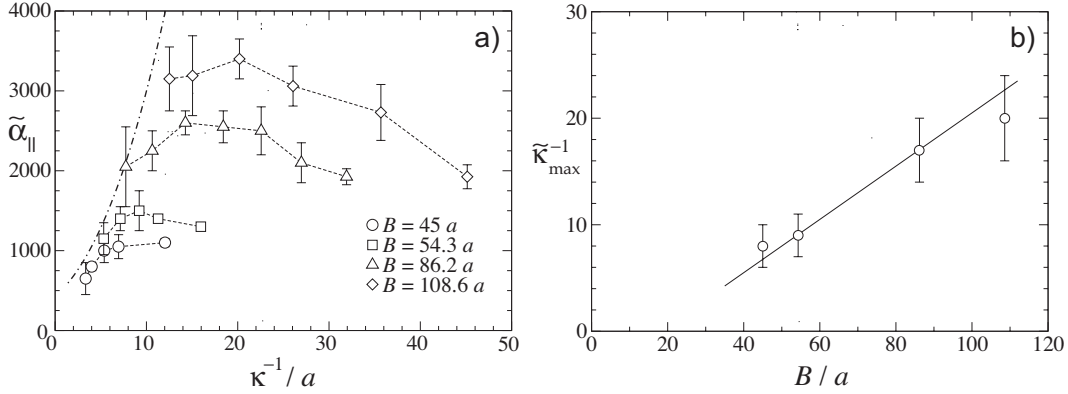


Figure 7.5: a) Parallel polarizability for $N = 10$ and $\zeta = 5$ and various box sizes. $\tilde{\kappa}^{-1}$ is changed by adding salt ions to the system. The thick broken line is eq. (7.35). b) Position of the maximum $\tilde{\kappa}_{\max}^{-1}$ as a function of the box size. The line is eq. (7.44).

and zero otherwise. If the double layer is reasonably thin one can set

$$U_i \approx k_B T \frac{\zeta a}{2} \int \frac{\rho_{xz}(x, z) \rho_{xz}(x', z')}{|x - x'|} dx dx' dz dz' \quad (7.41)$$

$$U_E = -qE \int z \rho_{xz}(x, z) dx dz. \quad (7.42)$$

Following the above procedure and assuming further $\kappa^{-1} \gg a$ one finds

$$\alpha_{2D}^{\perp} = 4\pi\epsilon\epsilon_0 \frac{1}{9} \frac{(2a + 2\kappa^{-1})^2 (L + 2\kappa^{-1})}{\ln[(L + 2\kappa^{-1})/a] - 1}. \quad (7.43)$$

Summarizing the model, the parallel polarizability scales with the longest dimension $L + 2\kappa^{-1}$ cubed, the perpendicular polarizability linearly. The aspect ratio $L/(2a)$ has only a logarithmic influence.

7.1.3 Effects of polymer and salt concentration

The scaling predictions are now tested with simulations as described in section 7.1.1. Fig. 7.5a is one of the main results of this section. For given box sizes (in this case for $N = 10$ and $\zeta = 5$), α_{\parallel} is a non-monotonic function of κ^{-1} which is defined by eq. (2.28). The rightmost point for a given B is always the $N_s = 0$ case, the leftmost point corresponds to 60 – 80 salt molecules. For $\kappa^{-1} \ll B - L$ α_{\parallel} is nearly independent of the box size. It increases with κ^{-1} until it reaches a maximum when the counterion cloud reaches the bounding box. The dilute polymer solution behavior, $B \gg \kappa^{-1}$, is well described by eq. (7.35). It is noteworthy that eq. (7.35) appears to be a good description even for $\kappa^{-1} \approx L$ albeit it is derived for thin double layers. For higher values of κ^{-1} , α_{\parallel} decreases again. The counterion cloud is disturbed by the potential of the polymers in the neighboring boxes. It is - in a sense - an effect of the semidiluteness of the polymer solution and causes the strong dependence of α_{\parallel} on B . The graphically determined position of the maximum of $\tilde{\alpha}_{\parallel}$, $\tilde{\kappa}_{\max}^{-1}$, fits well to a straight line:

$$\tilde{\kappa}_{\max}^{-1} \approx 0.25 (B - L). \quad (7.44)$$

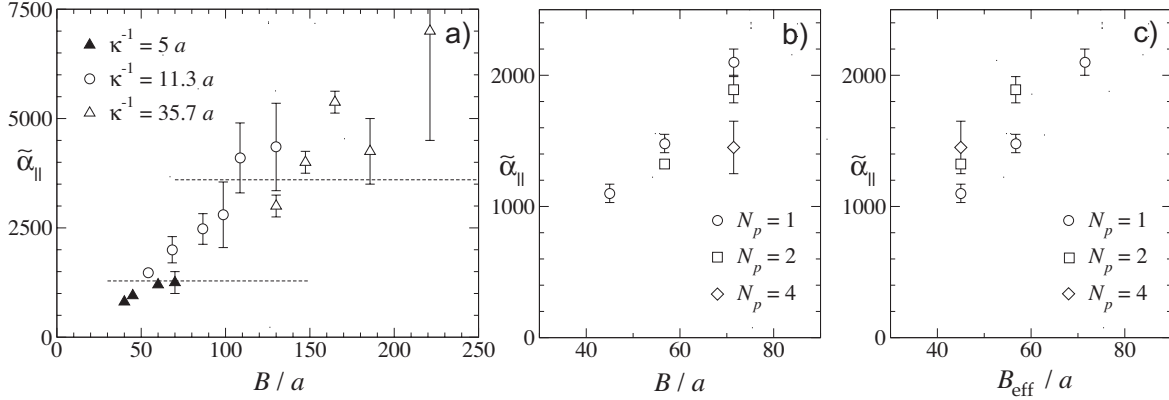


Figure 7.6: Box size dependence of the parallel polarizability of a $N = 10$ rod. a) Simulations at three different screening lengths compared with the limiting values from eq. (7.35) for $\tilde{\kappa}^{-1} = 5$ and $\tilde{\kappa}^{-1} = 11.3$. b) Effect of the number of polymers N_p at $\tilde{\kappa}^{-1} = 12.1$. c) Same as b) but plotted as a function of the effective cell size $B_{\text{eff}} = B/N_p^{1/3}$.

Eq. (7.35) suggests that there exists a finite limiting value at infinite dilution $\tilde{B} \rightarrow \infty$ but constant $\tilde{\kappa}^{-1}$. Free draining ion distributions (see fig. 7.3) show a quick decay of the charge asymmetry $\Delta\rho_z$ towards the cell boundary which is probably exponential due to screening for large enough systems. In fig. 7.6a one can see that the simulation data including HI are consistent with a saturation of α_{\parallel} at value approximately that predicted by eq. (7.35) though the error bars become quite large. Including more than one polymer in the simulation cell also reduces α_{\parallel} (b), which justifies the interpretation of B^{-3} as the polymer concentration c_p . The results are plotted as a function of the effective cell size

$$B_{\text{eff}} = B/N_p^{1/3} \quad (7.45)$$

in (c). It makes thus a difference if all polymers are placed on a regular lattice with spacing B as in the case of $N_p = 1$ or if some are allowed to move with respect to each other ($N_p > 1$). The qualitative behavior, i.e. the overlapping of the counterion clouds, is, however, the same.

Fig. 7.7 shows the perpendicular polarizability and the Kerr constant as function of $\tilde{\kappa}^{-1}$ for different \tilde{B} . For $L + 2\kappa^{-1} \ll B$ both quantities increase with κ^{-1} and follow thus the same trend as $\tilde{\alpha}_{\parallel}$. A decrease of the electric birefringence upon adding salt for a polymer solution well below the overlap concentration has been observed for fd-virus particles [82] and poly(p-phenylene) rods (PPP) [89] of lengths of the order of 10 nm: The birefringence signal nearly vanishes for $\kappa^{-1} \ll L$. The box size dependence of K' is much smaller than that of the polarizabilities, which is a result of the partial canceling of the dependencies from $\tilde{\alpha}_{\parallel}$ and $\tilde{\alpha}_{\perp}$. $\Delta\tilde{\alpha}$ - being the difference of two quantities with large error bars - is not shown as the simulation results were not accurate enough to display a systematic trend. A check of the relation $15\tilde{K}' = \Delta\tilde{\alpha}$ is done in fig. 7.8a.

7.1.4 Length dependence

Earlier in this chapter several theoretical works dealing with the dependence of the polarizability on the length of the rod-like particles were listed. To reduce them to a common

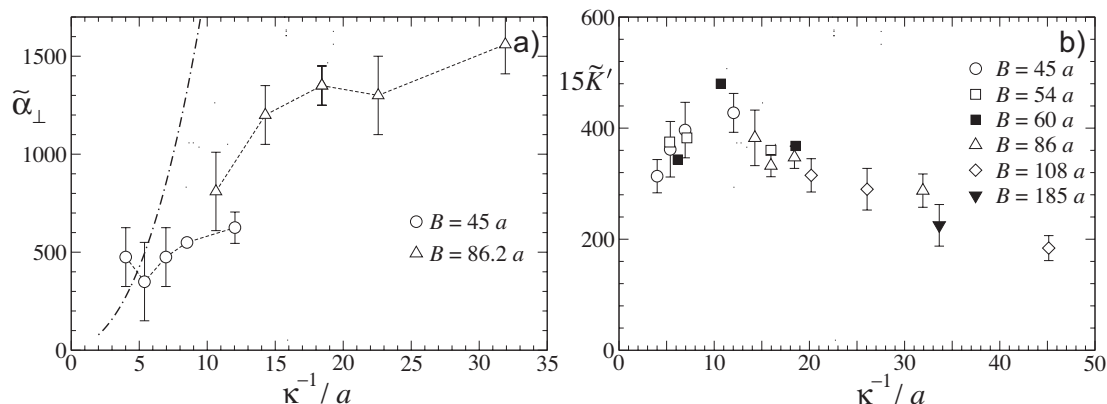


Figure 7.7: a) Screening length dependence of the polarizability perpendicular to the long axis. Since the statistical errors are quite large only two box sizes have been simulated. The broken line is the $\tilde{B} \rightarrow \infty$ prediction eq. (7.43). b) The rescaled Kerr constant which should be equal to $\Delta\tilde{\alpha}$ shows a much weaker dependence on \tilde{B} . $\Delta\tilde{\alpha}$ is the difference of two quantities with large error bars; simulations were not accurate enough to display a systematic trend of $\Delta\tilde{\alpha}$ with $\tilde{\kappa}^{-1}$, only three special cases obtained from long-run simulations are shown in fig. 7.8a.

denominator, a cubic length dependence of α_{\parallel} is expected if the counterions are close to the polymer, whereas for more extended diffusive clouds the exponent may be smaller than three. α_{\perp} is believed to be smaller than α_{\parallel} so that the birefringence is approximately proportional to α_{\parallel} .

The Brownian dynamics simulations applied here avoid many of the approximations made in earlier works. Solvent flow and conduction effects are included from the beginning, no artificial distinction between bound and free counterions needs to be made, as well as the Debye-Hückel approximation. On the other hand, the simulations use only a small number of ions to account for the whole cloud, and a - albeit physically motivated - finite box size. Fig. 7.8a shows the polarizabilities in both major directions, $\tilde{\alpha}_{\parallel}$ and $\tilde{\alpha}_{\perp}$, their difference $\Delta\tilde{\alpha}$, and the modified Kerr constant \tilde{K}' as a function of monomer number. $\Delta\tilde{\alpha}$ equals $15\tilde{K}'$ within error bars. For all N the same $\tilde{\kappa}^{-1}$ and \tilde{B} are used. It is checked that at least $\tilde{B} > \tilde{L} + 4\tilde{\kappa}^{-1}$ which means according to eq. (7.44) the screening length is smaller than κ_{\max}^{-1} . If \tilde{B} is too small or even kept constant while increasing N an effective power less than three of the length dependence of $\tilde{\alpha}$ can be seen. This is exactly what is observed in figure 8 of [190].

In fig. 7.8b, the Kerr constant is shown for monomer numbers in the range from five to forty. The ionic strength dependence is small on this logarithmic scale. I also changed the coupling strength ζ . In the limit of $L \gg \kappa^{-1}$ one clearly sees the cubic behavior, $K' \propto N^3$. For smaller N deviations due to the finite ion cloud extension occur.

Elias and Eden [35] find a cubic length dependence of the Kerr constant for DNA strands shorter than 50 nm at 1 mM salt. For longer chains it crosses over to an approximate quadratic dependence which they attribute to flexibility. Stellwagen [167] finds a quadratic length dependence for DNA up to 400 nm but only after applying a correction factor which is supposed to account for bending. Hogan et al. [70] also find a quadratic dependence for DNA shorter than 80 nm in 2.5 mM salt, obtained from electric dichroism. The DNA concentration was not specified which makes an interpretation difficult. These experimental

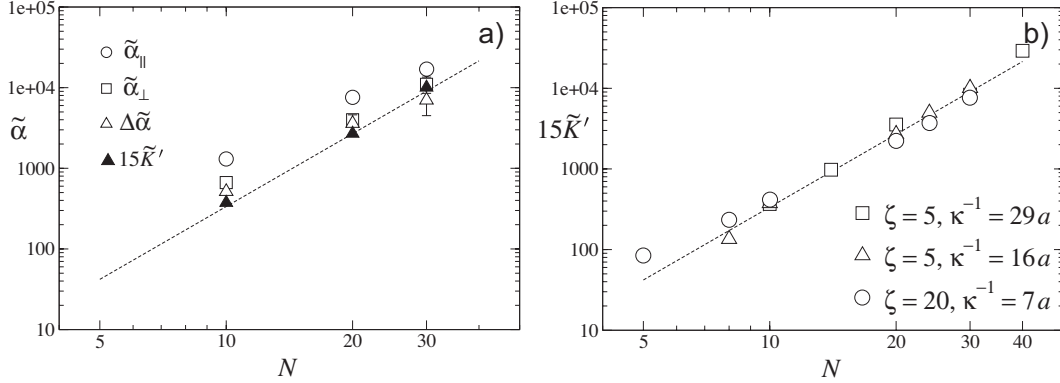


Figure 7.8: a) Connection between the polarizability and the Kerr constant: $\tilde{\alpha}_{\parallel}$ (circles), $\tilde{\alpha}_{\perp}$ (squares) and $\Delta\tilde{\alpha}$ (white triangles) compared with $15\tilde{K}'$ (black triangles). Parameters: $\tilde{\kappa}^{-1} = 15.96$, $\zeta = 5$ and $\tilde{B} = 108.6$. The dashed line is a cubic fit (same as in b). b) Rescaled Kerr constant as a function of monomer number N for the triples of parameters: $\tilde{\kappa}^{-1} = 7.98$, $\zeta = 20$ and $\tilde{B} = 108.6$ (circles); $\tilde{\kappa}^{-1} = 15.96$, $\zeta = 5$ and $\tilde{B} = 108.6$ (triangles); and $\tilde{\kappa}^{-1} = 29.13$, $\zeta = 5$ and $\tilde{B} = 185.7$ (squares). Parameters: $\ell_P/L \geq 10$, and N_s adapted to $\tilde{\kappa}^{-1}$ and \tilde{B} ($0 \leq N_s \leq 55$). The dashed line is a cubic fit to the combined set of points, $15\tilde{K}' = 0.336 N^3$.

results stimulated the search for models [41, 147] able to predict this exponent smaller than three. Although I cannot explain the experimental findings the simulations make clear that it is not just the hydrodynamic interactions and extended ion clouds that lead to the deviations from Mandel's scaling result.

7.1.5 Free versus bound counterions

It shall be investigated whether the close layer (to the polymer) of counterions shows distinct features with respect to polarization which are different from that of the whole cloud as e.g. postulated in [175]. In [122] it was demonstrated that the above cutoff criterion can qualitatively reproduce Manning's counterion condensation behavior of an infinitely long cylinder. In fig. 7.9b it is visible that the fraction of bound counterions only depend on the ionic strength of the solution and not on the box size. It slightly increases for longer chains (cf. the $N = 20$ case).

Washizu and Kikuchi [179] sort the counterions according to their distance from the macromolecule. Displaying this distance as a function of the ordinal number in this list they define the number of bound counterions as the position where the function changes its curvature. Using extensive Monte Carlo simulations they show that the partial polarizability coming from the n innermost counterions has a minimum approximately at $n = N_b$ where N_b is the number of bound counterions. Hence, N_b distinguishes not only spatial distributions of the two kinds of counterions but also their polarization behavior.

The sheath of bound counterions in their definition is quite extended (several rod diameters) and at its boundary already very diffusive, which is not what people expect from experiments with e.g. DNA. I will thus stick to the simple cutoff criterion that defines counterions within a distance of $4a$ to any monomer as "bound". Fig. 7.9a shows the polarizabilities of the bound counterions only, eq. (7.12), as a function of monomer number and for two screening lengths. The scaling is approximately $\tilde{\alpha}_{\parallel}^b \sim N^3$ and $\tilde{\alpha}_{\perp}^b \sim N$ but deviations for large N

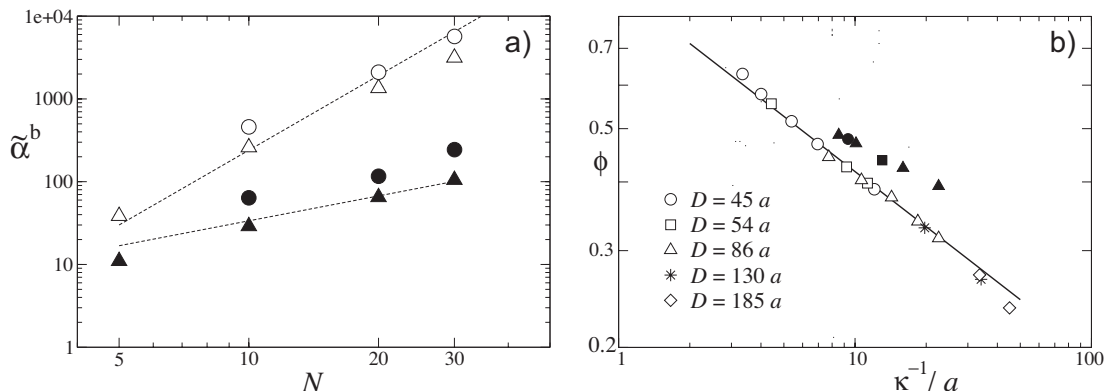


Figure 7.9: a) Polarizability components of the bound counterions: α_{\parallel}^b (white symbols) and α_{\perp}^b (black symbols). Parameters: $\tilde{\kappa}^{-1} = 15.96$, $\zeta = 5$ and $\tilde{B} = 108.6$ (triangles); and $\tilde{\kappa}^{-1} = 7.98$, $\zeta = 20$ and $\tilde{B} = 108.6$ (circles). The lines are cubic and linear guides to the eye, respectively. b) Fraction of bound counterions ϕ as a function of the screening length for $N = 10$ (white symbols) and $N = 20$ (black symbols). The data points for different \tilde{B} all fit approximately to a straight line which has a slope of -0.33 for $N = 10$.

are visible. The $\tilde{\kappa}^{-1} = 7.98$ data points are above those with $\tilde{\kappa}^{-1} = 15.96$ as more counterions are included in the dipole moment.

Lachemayer and Oppermann [89] noticed in their experiments with PPP that the decrease of the birefringence Δn upon addition of salt is very similar to that of the conductivity contribution of the polyelectrolyte. They conclude that since the conductivity contribution of the cloud as a whole is reduced it is the ion cloud and not the condensed counterions that is mainly responsible for polarization. Comparison of the numerical values of the polarizability differences $\Delta\tilde{\alpha}$ and $\Delta\tilde{\alpha}^b$ with $15\tilde{K}'$ in figures 7.8 and 7.9 shows that indeed the bound counterions only give a small fraction of the total polarizability.

7.2 Electric birefringence and anomalies

Prior to an electric birefringence experiment one has to make sure that positive or normal birefringence really corresponds to parallel orientation. This can be done by flow fields. It turns out that all rods under investigation in this thesis belong to this class so that in the following I will use normal birefringence and parallel rod orientation synonymously. O’Konski and Zimm [130] were one of the first demonstrating that normal birefringence seen with TMV is mainly caused by an orientation due to induced dipoles. Many semiflexible or rod-like polymers possess no or only a weak permanent dipole moment, e.g. actin and fd-virus. The ionic double layer polarizability results are therefore of central importance for these experiments. However, several cases of anomalous birefringence have been reported where the induced dipole orientation mechanism cannot work [48, 81, 82, 136]. Most of these cases were explained by various polarization effects [4, 22, 69] but no unified picture could arise. In the following I restrict myself to the proposed hydrodynamic mechanism for anomalous birefringence and dichroism, and to dilute and semidilute polymer solution such that steric interaction are negligible.

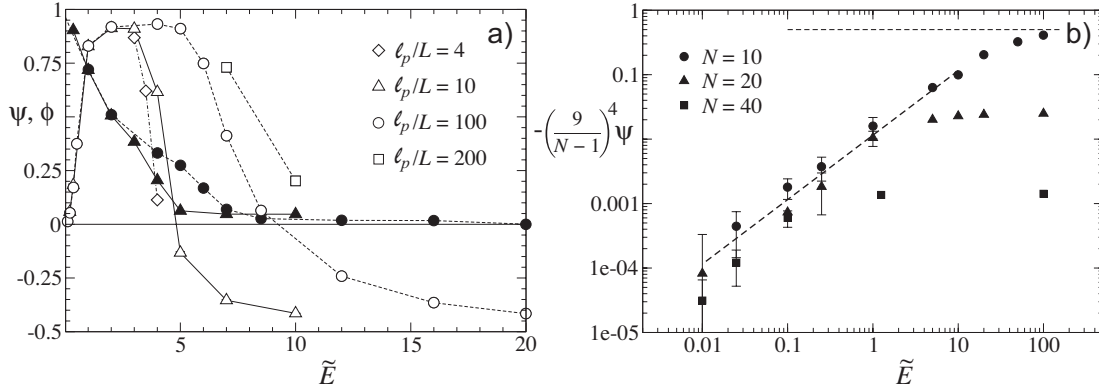


Figure 7.10: a) Orientation parameter ψ (white symbols) and fraction of counterions close to the chain ϕ (black symbols) for various stiffnesses ℓ_P/L . Parameters: $N = 10$, $\zeta = 20$, $\tilde{\kappa}^{-1} = 7.98$ and no added salt, $N_s = 0$, which means $\tilde{B} = 54.3$. b) Purely hydrodynamic, i.e. electrophoretic, orientation (data taken from fig. 3.5) as function of the driving field for $N = 10$. Points for longer chains, $N = 20$ and $N = 40$, are rescaled to match the low field limit of $N = 10$. The persistence length is adapted to \tilde{E} via $\ell_P/L = 100\tilde{E}$.

7.2.1 Arguments for a hydrodynamic orientation

From eq. (3.33) one finds for $\ell_P/L = 10$ and $N = 10$, i.e. $L/a = 18$, in the case of purely hydrodynamic orientation a rescaled Kerr constant of $15\tilde{K}'_H \approx -8.7$, for $\ell_P/L = 10$ and $N = 30$, i.e. $L/a = 58$, $15\tilde{K}'_H \approx -933.6$. These numbers are much smaller than the Kerr constants typically obtained from polarization (see e.g. fig. 7.8b). Since ℓ_P/L cannot be much less than unity for the chain to be approximately rod-like, anomalous birefringence can only be observed if either L/a is a very large number or if the polarizability of the rod-counterion cloud complex is drastically reduced.

Destruction of the ion cloud by high electric fields

One way of reducing the polarizability is to apply high electric field: It is commonly observed (see e.g. [82, 167]) that the electric birefringence saturates at high fields. It can be explained by stripping away the ion cloud from the polymer [148, 190] and is related to the Wien effect in electrophoresis [182].

Fig. 7.10a shows the orientation parameter ψ for $N = 10$ and several stiffnesses ℓ_P/L . Starting at random orientation, $\psi(\tilde{E} = 0) = 0$, increasing \tilde{E} results in a nearly complete alignment of the rod-like polymers in the direction of the field. After passing through a maximum ψ decreases and approaches $-1/2$ which corresponds to perpendicular orientation. The maximum shifts to higher \tilde{E} values for greater ℓ_P/L . This indicates that bending and hydrodynamic orientation are the cause for the decrease of ψ . That the counterion atmosphere is indeed stripped away can be seen from the behavior of the fraction of close counterions ϕ (black symbols, displayed only for two values of ℓ_P/L). The situation is complicated by the dependence of ϕ on the average orientation of the rod, visible from the fact that both curves of ϕ deviate from each other. For comparison, the field dependence of hydrodynamic orientation, fig. 3.5, is replotted but in a slightly different manner in part b) of fig. 7.10.

On the scaling level, the destruction of the counterion cloud sets in when it is shifted by

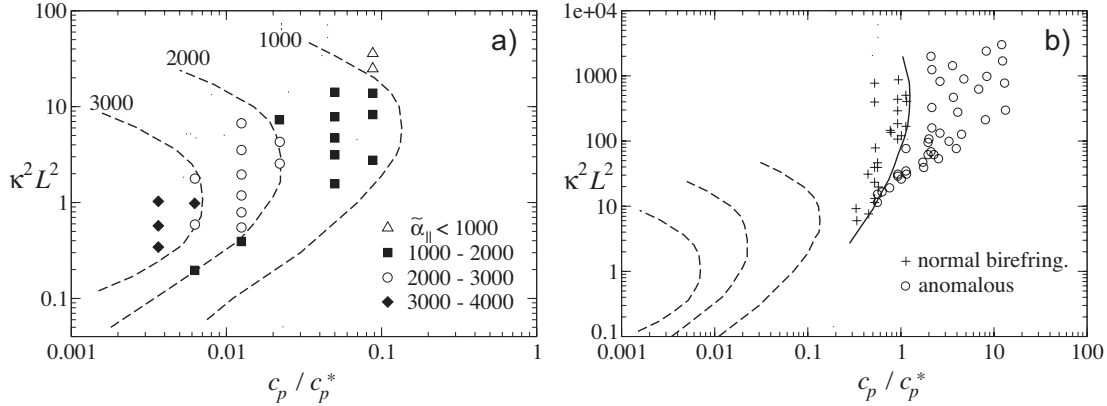


Figure 7.11: a) Contour plot of $\tilde{\alpha}_{\parallel}$ for a $N = 10$ rod as a function of polymer and salt concentration, measured by c_p/c_p^* and $\kappa^2 L^2$, respectively. The dashed contour lines do not only separate the groups of symbols but take also the values of $\tilde{\alpha}_{\parallel}$ within each group into account, e.g. symbols crossed by contour line 2000 are in the range from 1950 to 2050. b) Birefringence data of fd-virus taken from [81] compared with the contour lines of a). The solid line is a guide to the eye separating the normal from the anomalous birefringence regime.

a distance L away from the rod, or in terms of the dipole moment $P = \alpha E \sim qNL$. Since $\alpha \sim L^3$ the critical field E_{ϕ}^* where the cloud is stripped away scales as $E_{\phi}^* \sim 1/L$. From eq. (3.33), one gets for the critical field E_H^* necessary for complete hydrodynamic orientation: $E_H^* \sim (\ell_P/L)^{1/2}/L^2$. The condition $E > E_H^*$ is not sufficient for anomalous birefringence because the induced dipole orientation also becomes stronger with increasing E . It is thus necessary that both conditions, $E > E_H^*$ and $E > E_{\phi}^*$, are fulfilled. From the different scaling of E_H^* and E_{ϕ}^* one can see that for long polymers $E > E_{\phi}^*$ determines the critical field strength for anomalous birefringence.

Experimentally accessible values of \tilde{E} are usually below one, see e.g. the examples in section 3.5. Kramer et al. observe a saturation of the normal birefringence at $E \approx 10^5$ V/m but no further decrease [82]. Instead they find anomalous behavior at low and intermediate field strengths for particle concentrations above the overlap concentration. This so-called *low-field anomaly* cannot be explained within the model presented here.

Overlapping counterion clouds

In fig. 7.11a the data of fig. 7.5a plus two additional curves at $\tilde{B} = 71.1$ and $\tilde{B} = 130$ are presented in a way that is more useful for a direct comparison with experiments: The polymer concentration is expressed in multiples of the overlap concentration,

$$c_p^* = 1/L^3, \quad (7.46)$$

and the salt concentration by $\kappa^2 L^2$, which is proportional to the ionic strength of the solution. The dashed lines are the presumed contour lines where $\tilde{\alpha}_{\parallel} = 1000, 2000$ and 3000 , respectively. They are determined not only by separating the data points into groups; the values of the simulation points at constant c_p/c_p^* are extrapolated to high and small $\kappa^2 L^2$ (see also fig. 7.5a) to give estimates of the contour lines in these regions. Points crossed by the line $\tilde{\alpha}_{\parallel} = 2000$, for instance, are in the range from from 1950 to 2050.

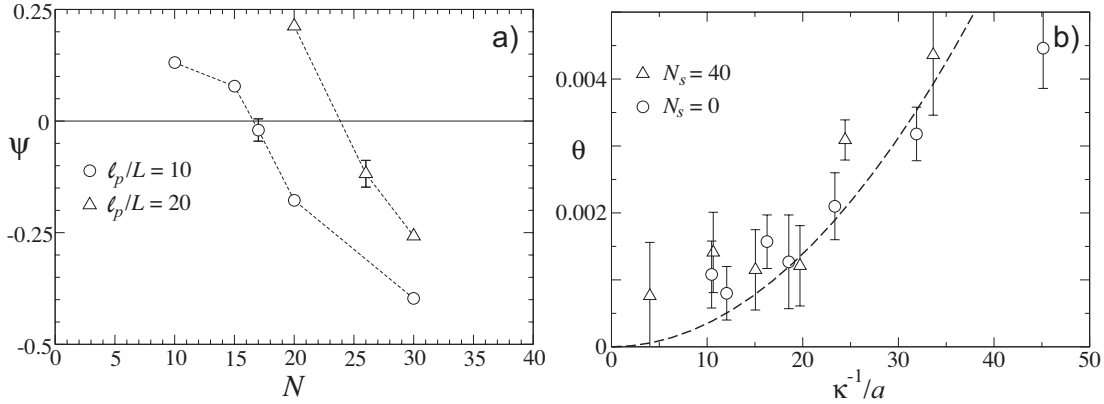


Figure 7.12: a) Crossover from dipole to hydrodynamic orientation with increasing chain length for fixed $\ell_p/L = 10$ (circles) and $\ell_p/L = 20$ (triangles). Parameters: $\tilde{\kappa}^{-1} = 15.96$, $\tilde{E} = 1$, $\zeta = 5$ and $N_s = 0$. The box size can be calculated from these parameters and is in the range $54.3 \leq \tilde{B} \leq 78.3$. b) Bending angle as a function of the screening length for $N = 10$, $\ell_p/L = 10$, and $N_s = 0$ or $N_s = 40$, respectively.

Fig. 7.11b shows fd-virus transient electric birefringence measurements (TEB) [81] at various monovalent salt and fd-virus concentrations. For the rescaling a virus length of 880 nm is assumed. Parameters where normal birefringence occurs, possibly due to an induced dipole orientation mechanism, are marked with a plus, anomalous birefringence with a circle. A solid line is drawn at the boundary where normal birefringence sets in. Kramer et al. explain anomalous birefringence with a model introduced by Hoffmann et al. [69]: In their picture, the overlapping clouds form a three-dimensional network in which counterions can stream along the long axes of the rods without causing any dipole moment in that direction; the small perpendicular polarization should still be possible and be responsible for anomalous birefringence. The simulations agree with their result that overlapping counterion clouds should decrease the parallel polarizability but do not reproduced the perpendicular orientation for rigid rods; only for rods with finite flexibility anomalous orientation in an external field is observed.

I will discard this possibility of such a network formation and rather assume that perpendicular orientation is caused by hydrodynamic effects formulated in chapter 3. Overlapping clouds are merely responsible for the decrease of the parallel dipole orientation effect such that the much weaker perpendicular hydrodynamic orientation can set in. It is conjectured that the solid line in fig. 7.11b is given by a constant small value of $\Delta\tilde{\alpha}$ and thus $\tilde{\alpha}_{\parallel}$. To that end the contour lines of a) are also shown. If one extrapolates these lines to $c_p > c_p^*$ one can see that they can qualitatively describe the boundary between normal and anomalous birefringence although their bow is somewhat steeper. This discrepancy can easily be caused by discretization errors for these short chains ($N = 10$) besides the uncertainty coming from the limited number of points in a). It may also be caused by the screening of hydrodynamic interactions to be discussed at the end of this chapter.

Anomalous birefringence can thus be obtained in two ways: at a particle concentration below overlap by *lowering the salt concentration* to a very small value (crossing the solid line in fig. 7.11 vertically), or by *raising the polymer concentration* at a given salt condition

(crossing the line horizontally).

Collapse of the ion cloud at high salt concentration

In section 7.1.3 experiments were cited [82, 89] that show a strong decrease of the birefringence signal at high salt concentrations. This decrease is also seen in simulations in fig. 7.7b for $\kappa^{-1} < 10a$ although the effect is small which is in part due to the finite ion sizes. Can hydrodynamic orientation be observed under these conditions? Anomalous birefringence is neither seen in these experiments nor in simulations. The small polarizability in the limit $\kappa^{-1} \rightarrow 0$, cf. eq. (7.35), is sufficient to cause parallel orientation, while hydrodynamic orientation is screened due to the high salt concentration. It seems that this possibility is ruled out.

Changing the polymer length

Eq. (3.33) states that the hydrodynamic contribution to the Kerr constant increases with the fifth power of the rod length, beside logarithmic corrections, the polarizability only with the third power. Long semiflexible rods that can be polymerized up to different lengths should exhibit a transition from normal to anomalous birefringence when their length is increased. From eq. (7.35) one finds the following condition for anomalous birefringence,

$$\frac{1}{8}(\tilde{L} + 3\tilde{\kappa}^{-1})^3 \sim \tilde{\alpha}_{\parallel} \sim \Delta\tilde{\alpha} \sim 15\tilde{K}'_H \approx 1.6 \times 10^{-4} \zeta \frac{L^5}{\ell_P a^4}, \quad (7.47)$$

which is valid in very dilute polymer solution. If κ^{-1} is not considerably larger than L , say for definiteness $3\kappa^{-1} = L$, the condition leads to

$$L/a > 10^2/\zeta \sqrt{\ell_P/a} \quad (7.48)$$

Since DNA has a persistence length of 50 nm at 100 mM salt and a diameter of 2 nm the condition can only be fulfilled if the polarizability is weakened by other factors. f-actin is more promising: With $\ell_P/a \approx 2000$ one gets a minimum length of less than $1\mu\text{m}$.

Kobayasi et al. [78] started the polymerization to f-actin by adding a small amount of CaCl_2 (0.5 to 0.7 mM) to a solution of g-actin and observed the birefringence signal over time. A negative birefringence component appeared during this polymerization process. Perpendicular orientation is seen at a length of about $1.5\mu\text{m}$ and possibly already below. With an electric field of 3×10^4 V/m, a persistence length of $17.7\mu\text{m}$ [57], a diameter of 8 nm and a charge density of about $1e/\text{nm}$ equation (3.33) gives complete perpendicular orientation, $\psi = -0.5$, at a filament length of $L \approx 0.7\mu\text{m}$. It is thus likely that Kobayasi has observed hydrodynamic orientation.

In the simulations, fig. 7.12a, the polarizability is weakened by a strong electric field, $\tilde{E} = 1$. When the number of monomers is increases the orientation crosses over from parallel to perpendicular. The dependence of the crossover number on ℓ_P/L hints at an elastic origin.

7.2.2 Discussion

I shall list some objections to the proposition that anomalous birefringence is caused by the coupling of hydrodynamic interactions and elasticity. An overview of electrostatic alternatives

from the literature is given. At the end I try to arrive at a coherent picture of the different effects contributing to perpendicular orientation.

Screening of hydrodynamic interactions

The bending discussed in chapter 3 is caused by overlap of the flow fields from different parts of the polymeric chain and is therefore susceptible to the screening of hydrodynamic interactions during electrophoresis at high salt concentrations. It is exactly the effect that leads to the independence of the electrophoretic mobility of long polymers in salt solutions [108]. Counterions move in the direction opposite to the polymer and cancel the influence of the flow fields on length scales larger than κ^{-1} . The polymer is essentially free draining at high salt concentrations. Hence, if $\kappa^{-1} \ll L$ the hydrodynamic orientation mechanism does not work.

It is important to check whether this screening of the hydrodynamic effects is operative in the simulations. Fig. 7.12b shows the bending angle θ defined in fig. 3.1 as a function of the screening length. To exactly reproduce the results of chapter 3 in the limit $\kappa^{-1} \rightarrow \infty$ the monomer-monomer electrostatic interactions are artificially set to zero. Doing so complications due to an effective electrostatic persistence length are avoided. Two conditions, $N_s = 0$ (just counterion screening) and $N_s = 40$ (excess salt), are treated; the ionic strength is changed by varying the box size. Within error bars these two conditions show no difference in θ which is thus only determined by κ^{-1} . The points are fitted to a parabola as motivated by $\theta \sim L^2 (L/\ell_P)$ (cf. eq. (3.22)) if one assumes that bending occurs over a length κ^{-1} , i.e. replacing L by κ^{-1} .

How many screening lengths κ^{-1} are necessary for a complete screening of hydrodynamic interactions. Experimentally, a related question is: At which length does the electrophoretic mobility of a polyelectrolyte become independent of molar mass for a given ionic strength? For DNA Stellwagen et al. [168] observe a saturation of the electrophoretic mobility at about 150 bp if a buffer with 40 mM ionic strength is used. That is a polymer with $L > 30\kappa^{-1}$ starts to become free-draining. Since at 150 bp the DNA is still approximately rod-like, one can apply the result to the screening of the hydrodynamic bending: Only a κ^{-1} much smaller than L prohibits this hydrodynamic orientation.

From this perspective the the upper part of phase diagram fig. 7.11b ($\kappa^2 L^2 > 100$) can be understood: Positive birefringence is reduced upon the addition of salt because the polarizability is reduced due to the shrinking counterion cloud. This is described by the dashed lines. However, negative birefringence is suppressed due to screening; the solid line does not show this arc-like form. For fd-virus and f-actin which have lengths of the order of one micrometer hydrodynamic orientation is thus only conceivable at minimal salt concentration, 10^{-6} to 10^{-5} M.

Low field anomaly

Several authors have observed perpendicular orientation at small and intermediate electric field strengths in semidilute solutions of rod-like particles using birefringence [82, 120, 136], dichroism [140] and static light scattering [111]. In the case of fd-virus, the birefringence signal is anomalous for electric fields below 10^4 to 10^5 V/m, depending on the polymer and salt concentration. For higher fields the signal becomes normal. The effect clearly depends on the overlap of the counterion clouds as it increases with the polymer concentration and

decreases with salt concentration, i.e. when the cloud shrinks. The orientation parameter ψ of this anomaly is on the percent level and grows approximately with the second power of the electric field [82] so that it could be caused by hydrodynamic orientation (see estimates in section 3.5.2).

To explain the transition to normal orientation at higher field strengths one has to assume that either the polarizability is weakened at small and intermediate field strengths by some unknown process, or that the perpendicular orientation is caused by a mechanism other than hydrodynamic orientation. One such mechanism is the network model of Hoffmann et al. already presented before [69]. Another explanation was given by Cates [22]: The polymers together with their counterion clouds are modeled as mutually avoiding ellipsoidal particles. At high enough polymer concentrations steric effects lead to a *disk-like local order* in the fluid of ellipsoids. For weak electric fields that do not destroy the equilibrium correlation the disk-like clusters can only rotate as a whole. If the ellipsoids are aligned parallel to the field the dipole moments of the rods repel each other and destabilize the configuration. On the other hand, there is an attraction if the ellipsoids are aligned transverse to the fields, which enhances the polarizability and stabilizes this orientation. On average the perpendicular orientation is preferred for low fields. Higher fields destroy the local disk-like order, and particles align parallel to the electric field.

Several authors assume a *permanent perpendicular dipole* orientation as cause for anomalous birefringence since it is first order in the electric field [66, 78, 140]. At higher fields the induced dipole orientation, a second order effect, dominates and causes normal birefringence. However, the helical symmetry of many biopolymers preclude a permanent perpendicular dipole moment. Porschke [140] presents a possible explanation for semiflexible DNA of several hundred base pairs: Thermal bending results in a shift of the center of all charges of the polymer with respect to the center of diffusion giving rise to an effective permanent dipole moment perpendicular to the long axis if the configuration is frozen. He assumes transition barriers of the configurational changes that freeze the bent structure.

Conduction

The presence of an external field not only changes the mutual distances of all molecules and their orientation, it also gives rise to dissipative effects like conduction. It was already argued that even in linear response the polarizability cannot completely be described by a mere balance of the separation due to the external electric field and the electrostatic attraction between polymer and cloud since there is a continuous flux of ions entering and leaving the cloud (see chapter 6). The influence of the motion of the counterions along the polymer on the polarizability, effects like electrostatic friction [123], are not investigated in this thesis although they are included in the simulations. Fixman and Jagannathan [43] showed that convective effects are important for polarization. Conduction effects might therefore be a cause for anomalous birefringence similar to what has been proposed in [69].

Conclusions

It was the goal of this chapter to investigate experimental conditions under which the hydrodynamically induced perpendicular orientation is observable in strong electric fields. The results are relevant for electric birefringence and dichroism measurements, as well as for electrophoresis since the mobility of long rods is a factor of two smaller for perpendicular

orientation compared to parallel one. As a prerequisite, the dependence of the polarizability on salt and polymer concentration and polymer length was investigated. It was argued that anomalous birefringence seen with actin filaments is caused by hydrodynamic orientation, while the anomaly observed in semidilute solutions with overlapping counterion clouds allows for several interpretations. It is also speculated that the Wien effect in very strong fields can lead to a perpendicular orientation.

The screening of hydrodynamic interactions limit our proposed orientation mechanism to dilute salt solutions. It is therefore as likely that the low-field anomaly is rather due to electrostatic and steric effects as for example in the model of Cates since hydrodynamic effects alone cannot explain the weakening of the parallel orientation. It is conceivable that both mechanism contribute to this anomaly in their respective limits, the clustering model of Cates for denser systems, the hydrodynamic model for rather dilute polymer solutions and very extended clouds.

Chapter 8

General Conclusions and Outlook

In this thesis interesting new phenomena in the context of single polymer dynamics in an external field were presented where hydrodynamic interactions play an important role. The chapters 3, 4 and 7 deal with rod-like chains with finite elasticity, chapter 5 with flexible chains and chapter 6 with the intermediate semiflexible range. Electrostatic effects were included for stiff and semiflexible chains but not for flexible ones. The reason for this neglect is that the latter case was already recently covered for free-draining hydrodynamic interactions [122, 123]: Strong electric fields lead to an unfolding transition that depends on the polymer length and charge. It was checked that the use of Rotne-Prager hydrodynamic interactions does not qualitatively change this picture.

The main results of the investigations presented here are three transitions induced by external forces that can be easily observed in experiments: the perpendicular orientation of a semiflexible rod in a homogeneous Stokes flow, the folding of an elastic rotating filament around its axis, and the conformational changes of self-avoiding flexible polymers to a tadpole-shaped structure under sedimentation forces. The first and the last situation are in fact limiting cases of the same problem, the response of an elastic object in a viscous fluid to an external force, for very small and high persistence lengths. In addition the salt-dependence of the diffusion and polarization of polymers was investigated to clarify several issues controversially discussed in the literature.

Some problems had to be left out: The section on electrolyte friction of semiflexible polymers can only serve as a first step although many features can already be seen from the special cases presented. Several conclusions for the birefringence of charged rods were only drawn indirectly from the parallel polarizability due to limitations of the computer power; it is hoped that later investigations can add the missing pieces.

The phenomena are not only important in their own right. Due to their strong length dependence, the hydrodynamic orientation and unfolding mechanisms must be taken into account when polymers are separated in solution according to their molecular weight. With some clever design one might even be able to invent new separation techniques based on these effects that avoid the staining of the sample and other difficulties encountered in capillary electrophoresis [164]. The controlled compactification and unfolding of flexible polymers in an ultracentrifuge by tuning the rotor speed has a great potential in the context of large proteins as their function depends on the tertiary structure. It should be regarded as an alternative to shear flow and electric methods. The difference of their sedimentation coefficients by nearly a factor of two at high rotor speeds offers a new and unambiguous method to separate linear

and circular polymers of the same molecular weight.

Appendix A

Description of the Numerical Method

A.1 Langevin iteration

Boundary conditions

Minimal image boundary conditions are used which means that the simulation box is repeated in all spatial directions, but interactions of a particle are restricted to particles within a box of the size of the simulation box but centered at the particle [1]. In other words, the boundaries of the simulation box are wrapped to form a higher dimensional torus. Two particles interact along their shortest distance in that geometry; self-interaction is not possible. The diameter of the box therefore defines a cutoff of the long-ranged forces which may also have a physical meaning (see chapter 7). If one wants to preserve the long-range character of all forces and of the hydrodynamic interactions, periodic boundary conditions with e.g. Ewald summation techniques [1, 9] should be used, which are usually quite costly from a numerical point of view.

Correlated random numbers

Getting the right equilibrium distribution in the presence of hydrodynamic interactions requires that the correlation matrix of the Brownian random shocks be proportional to the mobility matrix of the monomer units. This leaves one with the task of computing the square root of positive definite symmetric matrix. *Cholesky decomposition* is a very stable exact method but has a computational count of $\mathcal{O}(N^3)$ [144]. The idea is to factorize the positive definite symmetric \mathbf{H} into a lower diagonal, \mathbf{L} , and an upper diagonal part

$$\mathbf{H} = \mathbf{L} \cdot \mathbf{L}^T . \quad (\text{A.1})$$

This can be done by the recursion

$$\begin{aligned} L_{ii} &= \left[H_{ii} - \sum_{k=0}^{i-1} L_{ik}^2 \right]^{1/2} \\ L_{ij} &= \frac{1}{L_{ii}} \left(H_{ij} - \sum_{k=0}^{i-1} L_{ik} L_{jk} \right) , \quad j > i . \end{aligned} \quad (\text{A.2})$$

If $\Delta\xi_G$ is a $3N$ -dimensional Gaussian random vector with zero mean and unit variance then

$$\Delta\xi = (2k_B T \Delta t)^{1/2} \mathbf{L} \cdot \Delta\xi_G \quad (\text{A.3})$$

fulfills (2.8). $\Delta\xi$ is of course not unique; any matrix \mathbf{L} not necessarily lower diagonal with the property (A.1) can serve. Another possible choice is for example

$$\mathbf{H} = \mathbf{S} \cdot \mathbf{S} \quad (\text{A.4})$$

with $\mathbf{S} = \mathbf{S}^T$. Cholesky decomposition provides at the same time a good test whether the mobility matrix fulfills the physical condition of positive definiteness. The Oseen tensor might have negative eigenvalues even for only slightly overlapping beads, which can only be avoided by unfeasible short time steps and very strong stretching forces. On the other hand, the Rotne-Prager tensor which provides a first order correction for the finite bead radius [188] is by construction positive definite. Nevertheless, the minimal image boundary condition, i.e. a non-flat topology, may result in a no more positive definite matrix if the system is very dense and strongly overlapping. But this is only the case for very exceptional examples: Place for instance four unit spheres in a cubic box with edges of length 3.01 and minimal image boundary conditions at the points $(0, 1.5, 0)$, $(1.5, 0, 0)$, $(3, 1.5, 0)$ and $(1.5, 3, 0)$. The smallest eigenvalue of the Rotne-Prager diffusion matrix is -0.0087 ; hence the diffusion matrix is not positive definite.

There are *iterative methods* reported to be faster in certain cases [41, 44, 73] which calculate $\Delta\xi$ without determining \mathbf{L} or \mathbf{S} before: One of these is the Chebyshev polynomial approximation method by Fixman [44] which scales roughly like $N^{2.25}$. Since \mathbf{H} is a symmetric, positive definite matrix it can be written in the following spectral way

$$\mathbf{H} = \sum_{k=0}^{N-1} \lambda_k |k\rangle \langle k| \quad (\text{A.5})$$

where for all eigenvalues λ_k

$$\lambda_{\max} \geq \lambda_k \geq \lambda_{\min} > 0. \quad (\text{A.6})$$

Hence the matrix “square root” can be expressed

$$\mathbf{S} = \sum_{k=0}^{N-1} \sqrt{\lambda_k} |k\rangle \langle k| \quad (\text{A.7})$$

since the $|k\rangle$ are orthogonal. The square root function can be approximated by a sum of Chebyshev polynomials C_n

$$\sqrt{\lambda} \approx \sum_n c_n C_n(a\lambda + b) \quad (\text{A.8})$$

where usually a degree of $\mathcal{O}(10)$ is sufficient and

$$a = \frac{2}{\lambda_{\max} - \lambda_{\min}} \quad (\text{A.9})$$

$$b = \frac{\lambda_{\max} + \lambda_{\min}}{\lambda_{\max} - \lambda_{\min}} \quad (\text{A.10})$$

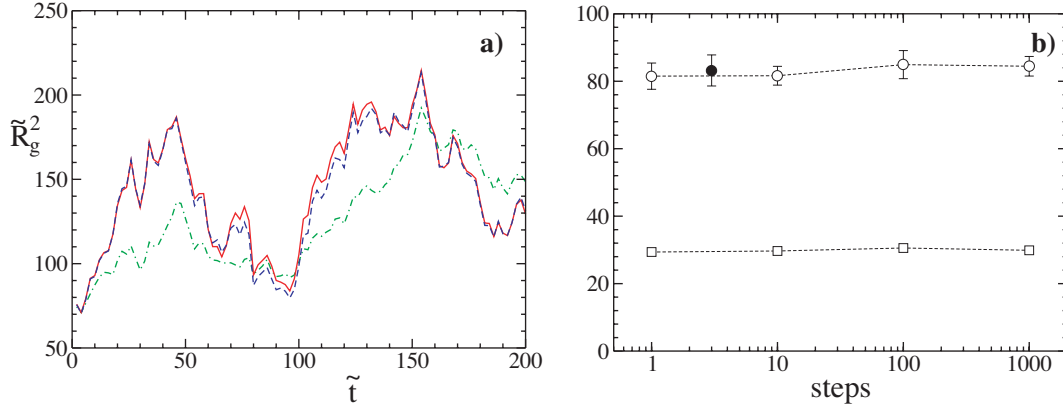


Figure A.1: Test of the approximation made in the correlation of the noise: a) Time evolution of the squared radius of gyration $R_g^2(t)$ of a $N = 50$ flexible chain for $E = 0$ and $\Delta = 10^{-3}$ in the free draining limit (dashed dotted line) and for the Cholesky decomposition done every (full line) and every 10th step (dashed line). b) Equilibrium (R_g^2 , open circles) and non-equilibrium (mobility at $\tilde{E} = 1$, squares) quantities as a function of number of steps between two successive Cholesky decompositions. For comparison, the free draining value of R_g^2 (black circle) is also shown.

to keep the argument of C_n between -1 and 1 . The Chebyshev coefficients c_n of the shifted square root function have to be determined only once at the beginning of the simulation. Plugging eq. (A.8) into eq. (A.8) yields

$$\mathbf{S} \approx \sum_{k=0}^{N-1} \sum_n c_n C_n(a \lambda_k + b) |k\rangle \langle k| = \sum_n c_n \mathbf{C}_n(a\mathbf{H} + b\mathbf{I}). \quad (\text{A.11})$$

\mathbf{C}_n are Chebyshev polynomials of matrices and \mathbf{I} is the unit matrix. The correlated random number of eq. (A.3) can be written as

$$\begin{aligned} \Delta \boldsymbol{\xi} &= (2k_B T \Delta t)^{1/2} \mathbf{S} \cdot \Delta \boldsymbol{\xi}_G \\ &\approx (2k_B T \Delta t)^{1/2} \sum_n c_n [\mathbf{C}_n(a\mathbf{H} + b\mathbf{I}) \cdot \Delta \boldsymbol{\xi}_G] \\ &= (2k_B T \Delta t)^{1/2} \sum_n c_n \boldsymbol{\eta}_n \end{aligned} \quad (\text{A.12})$$

where $\boldsymbol{\eta}$ is determined iteratively by

$$\boldsymbol{\eta}_0 = \boldsymbol{\xi}_G \quad (\text{A.13})$$

$$\boldsymbol{\eta}_1 = [a\mathbf{H} + b\mathbf{I}] \cdot \boldsymbol{\xi}_G \quad (\text{A.14})$$

$$\boldsymbol{\eta}_{n+1} = 2[a\mathbf{H} + b\mathbf{I}] \cdot \boldsymbol{\eta}_n - \boldsymbol{\eta}_{n-1}. \quad (\text{A.15})$$

Compared to Cholesky decomposition which scales as N^3 , Fixman's method requires $\mathcal{O}(10)$ multiplications of a vector times a matrix which scales just as N^2 . The difficulty arises from the unknown λ_{\max} , λ_{\min} and the degree of the polynomial which have to be estimated before the simulation. [73] gives a recipe how to do this. For polymer solutions without small ions I find only a slight improvement in speed for the desired accuracy and less than 200 monomers. In the case of many quickly moving counterions the number of iterations per time

step grows very large so that this alternative is discarded for charged systems. To cope with correlated random numbers, I thus choose a cruder but more efficient approximation: In my implementation, one iteration step scales approximately as $5N^2 + N^3$. So for systems with $N \leq 100$ the numerical effort by including hydrodynamic interactions can be kept within reasonable limits if the square root matrix is updated only every 10th step, which gives a good compromise between accuracy and efficiency (see fig. A.1). The approximation shows only minor effects in both equilibrium and non-equilibrium averaged quantities and no distinct trend. Of course, the use of numerical libraries like LAPACK [2] can raise the speed considerably (up to fifty percent).

Choosing the right time step

It is checked that the relevant equilibrium and non-equilibrium averaged quantities like radius of gyration and mobility do not change drastically any more if the time step Δt is lowered. Usually this is the case when the step sizes $\Delta \mathbf{r}$ of each particle, $\Delta \mathbf{r} = \mathbf{r}(t + \Delta t) - \mathbf{r}(t)$, are only a small fraction of the smallest length scale of the system, say one tenth of the monomer radius a .

In the weak bending regime of chapter 3, small external forces act on a chain with large elastic moduli. The turning speed is very small, and one would expect that Δt could be chosen at a moderate value to keep the monomer displacements well below a . Nevertheless unphysical oscillations of the monomers around their proper positions occur if e.g. the rescaled bending parameter times the rescaled time step becomes $\mathcal{O}(1)$. The onset of this behavior is very abrupt in Δt and more or less independent of external field E and monomer number N . I find empirically the approximate conditions $\gamma \Delta t \leq 4a/\mu_0$ and $\varepsilon \Delta t \leq 2\sqrt{2}a^3\mu_0$ in the case of Rotne-Prager level hydrodynamic interactions, and $\gamma \Delta t \leq a/\mu_0$ and $\varepsilon \Delta t \leq a^3\mu_0$ for the free draining case. In both cases the Lennard-Jones potential and the random shocks are excluded. In the chapters 3 and 7, the bending modulus is chosen proportional to the polymer contour length, $\varepsilon \propto N$. This necessitates the time step changing according to $\Delta t \propto 1/N$

Ergodicity and variance reduction

To check that really all relevant configurations are sampled, runs involving many particles are repeated several times with different initial conditions. This is especially important because large systems are simulated with fewer time steps so that the total simulation time does not exceed two weeks.

In chapter 7 the variance reduction method of [25] is sometimes applied. Two simulations are started with the same initial condition and the same pseudo-random number seed, one with electric field and one without. The simulation time is not very long so that at low electric fields the trajectories of both simulations are quite similar. Quantities whose expectation values at zero electric field vanish, like the dipole moment or the orientation parameter ψ , are calculated by subtracting from the finite-field average the zero-field average. For very long runs this makes no difference as the zero-field average tends to zero. On the other hand the variance is reduced since the random parts in both simulations are close to each other.

A.2 Data analysis

To estimate the numerical error of the observables a block-averaging method was used. It will be briefly described. Ergodicity is always assumed and has to be checked by different methods. Let x be a fluctuating quantity and x_i its measured values. A good estimator for the true expectation value is its average value

$$\bar{x} = \frac{1}{n} \sum_{i=1}^n x_i . \quad (\text{A.16})$$

Since n is a large but finite number (in this thesis usually $n = 10^4 - 10^5$ is used) one can ask for the error of this estimate, i.e. for the standard deviation

$$\Delta\bar{x} = \left[\langle \bar{x}^2 \rangle - \langle \bar{x} \rangle^2 \right]^{1/2} \quad (\text{A.17})$$

which is defined with respect to the true expectation $\langle \cdot \rangle$. The simple estimate for the error of the mean $\Delta\bar{x}$,

$$\frac{1}{n(n-1)} \sum_{i=1}^n (x_i - \bar{x})^2 , \quad (\text{A.18})$$

is valid if the x_i are statistically independent. Otherwise one can split the data points into m blocks such that the simulation time of one block is much longer than the correlation time of the observable x :

$$(\Delta\bar{x})^2 = \frac{1}{m(m-1)} \sum_{k=1}^m \left(\left[\frac{m}{n} \sum_{i=1}^{n/m} x_i \right] - \bar{x} \right)^2 . \quad (\text{A.19})$$

In this thesis $m = 10$ was used. The statistical independence is checked using the density-density correlation function.

A formal way to find the optimal number of blocks is given by a method reminiscent of real space renormalization group techniques [46]. One starts with the whole data set of n points and transforms them in to a new (primed) set half as large:

$$x'_i = \frac{1}{2}(x_{2i-1} + x_{2i}) \quad (\text{A.20})$$

$$n' = n/2 . \quad (\text{A.21})$$

With the definition of the correlation function

$$c_k = \langle x_i x_{i+k} \rangle - \langle x_i \rangle^2 \quad (\text{A.22})$$

the error of the mean can be written as

$$\Delta\bar{x} = \frac{1}{n} \left[c_0 + 2 \sum_{k=1}^{n-1} \left(1 - \frac{k}{n} \right) c_k \right] . \quad (\text{A.23})$$

Since the correlation function transforms as

$$c'_0 = \frac{1}{2}(c_0 + c_1) \quad (\text{A.24})$$

$$c'_k = \frac{1}{4}c_{2k-1} + \frac{1}{2}c_{2k} + \frac{1}{4}c_{2k+1} \quad , \text{ for } k > 0 \quad (\text{A.25})$$

$\Delta\bar{x}$ and \bar{x} remain invariant under the “blocking” transformation. The transformation is repeated until the estimator for c_0 ,

$$\frac{1}{n'-1} \sum_{i=1}^{n'} (x_i - \bar{x})^2, \quad (\text{A.26})$$

does not change any more. At the fixpoint,

$$\Delta\bar{x} = \sqrt{c'_0/n'} \approx \left[\frac{1}{n'(n'-1)} \sum_{i=1}^{n'} (x_i - \bar{x})^2 \right]^{1/2} \quad (\text{A.27})$$

as in eq. (A.19). If c_k decays faster than $1/k$ then it lies in the basin of attraction. At the fixpoint all x'_i are independent Gaussian variables and $c'_k = 0$ for $k > 0$. If the fixpoint has not yet been reached then eq. (A.27) is a lower bound for $\Delta\bar{x}$.

Appendix B

Treatment of Hydrodynamic Orientation

B.1 Quasi-rigid bodies in the bead-model approximation

The following section applies to rigid and semi-rigid bodies, i.e. to ones that can only be slightly deformed and for which the elastic degrees of freedom relax much faster than its orientation to an external field¹. I will restrict the discussion to a weakly bending rod. From the positions of the monomers one can calculate the 3×3 mobility tensors μ_{ij} (Rotne-Prager tensor) for two beads i and j and from them the translational grand mobility matrix \mathcal{M}^{tt} of eq. (2.17). The various 3×3 elements of eq. (3.1) with the origin O as reference point are now given by [50]

$$\zeta^{tt} = \sum_{ij} [(\mathcal{M}^{tt})^{-1}]_{ij} \quad (\text{B.1})$$

$$\zeta_O^{rt\dagger} = \sum_{ij} \mathbf{r}_i \times [(\mathcal{M}^{tt})^{-1}]_{ij} \quad (\text{B.2})$$

$$\zeta_O^{rr} = \sum_{ij} -\mathbf{r}_i \times [(\mathcal{M}^{tt})^{-1}]_{ij} \times \mathbf{r}_j. \quad (\text{B.3})$$

\mathbf{r}_i is the position of the center of bead i , and \times denotes the cross product, e.g. $[\mathbf{a} \times \mathbf{B}]_{\alpha\delta} = \sum_{\beta\gamma=1}^3 \varepsilon_{\alpha\beta\gamma} a_\beta B_{\gamma\delta}$ for any vector \mathbf{a} and matrix \mathbf{B} . The center of reaction \mathbf{r}_{OR} follows as

$$\mathbf{r}_{OR} = - \left[(\text{Tr } \zeta^{tt}) \mathbf{I} - \zeta^{tt} \right]^{-1} \cdot \left[\boldsymbol{\varepsilon} : \zeta_O^{rt\dagger} \right] \quad (\text{B.4})$$

where the second term on the right hand side is a double contraction with the Levi-Civita tensor $\boldsymbol{\varepsilon}$. Shifting the reference point in eq. (B.2) and (B.3) from the origin to the center of reaction R yields

$$\zeta_R^{rt\dagger} = \zeta_O^{rt\dagger} - \mathbf{r}_{OR} \times \zeta^{tt} = \zeta_R^{rt} \quad (\text{B.5})$$

$$\zeta_R^{rr} = \zeta_O^{rr} - \mathbf{r}_{OR} \times \zeta^{tt} \times \mathbf{r}_{OR} + \zeta_O^{rt\dagger} \times \mathbf{r}_{OR} - \mathbf{r}_{OR} \times \zeta_O^{rt} . \quad (\text{B.6})$$

One can invert the generalized friction matrix (3.1) to obtain the generalized mobility matrix (3.2) at the center of reaction R [50]. Note that μ_P^{tt} depends on the reference point

¹Bead models for rigid bodies are reviewed by García de la Torre and Bloomfield [54].

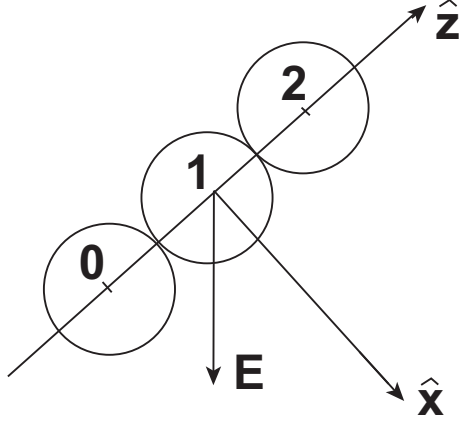


Figure B.1: Sketch of the three-bead model used in B.2. Stretching occurs in \hat{z} -direction and bending in the negative \hat{x} -direction. The distance of two adjacent spheres is $2a$ plus perturbations.

while μ^{rr} is independent. Using the vector from point R to the center of diffusion D

$$\mathbf{r}_{RD} = -[(\text{Tr } \mu^{rr}) \mathbf{I} - \mu^{rr}]^{-1} \cdot [\boldsymbol{\varepsilon} : \mu_R^{rt\dagger}] \quad (\text{B.7})$$

one finally arrives at [180]

$$\mu_D^{tt} = \mu_R^{tt} - \mathbf{r}_{RD} \times \mu^{rr} \times \mathbf{r}_{RD} + \mu_R^{rt} \times \mathbf{r}_{RD} - \mathbf{r}_{RD} \times \mu_R^{rt\dagger} \quad (\text{B.8})$$

$$\mu_D^{rt\dagger} = \mu_R^{rt\dagger} + \mu^{rr} \times \mathbf{r}_{RD} = \mu_D^{rt} \quad (\text{B.9})$$

Equations (B.8) and (B.9) can also be used to transform the mobility matrices to any other point, for example to a point where the total torque vanishes.

B.2 Perturbative calculation of a three-bead rod

It is instructive to see in an explicit example how the coupling between flexibility and hydrodynamic interactions works in the small deformation limit. A rod composed of three beads is placed in an external field at an angle of 45 degrees (fig. B.1). The origin is chosen to be the middle bead, the z-axis parallel to the long axis of the rod, the x-axis perpendicular to it. The third dimension is irrelevant by symmetry. The calculation is done on the Rotne-Prager level.

As in eq. (3.42), I write

$$\mathbf{r}_0 = \begin{pmatrix} 0 \\ -2 \end{pmatrix} + \begin{pmatrix} a_1 \\ b_1 \end{pmatrix} + \begin{pmatrix} a_2 \\ b_2 \end{pmatrix} + \mathcal{O}(E^3) \quad (\text{B.10})$$

$$\mathbf{r}_2 = \begin{pmatrix} 0 \\ 2 \end{pmatrix} + \begin{pmatrix} c_1 \\ d_1 \end{pmatrix} + \begin{pmatrix} c_2 \\ d_2 \end{pmatrix} + \mathcal{O}(E^3) \quad (\text{B.11})$$

which inserted into the elastic potential eq. (3.3) gives up to first order in E

$$\mathbf{F}_0^{(1)} = \begin{pmatrix} qE/\sqrt{2} \\ -qE/\sqrt{2} \end{pmatrix} - \frac{1}{8a} \begin{pmatrix} \varepsilon(a_1 + c_1)/a^2 \\ 4\gamma b_1 \end{pmatrix} \quad (\text{B.12})$$

$$\mathbf{F}_1^{(1)} = 3 \begin{pmatrix} qE/\sqrt{2} \\ -qE/\sqrt{2} \end{pmatrix} - \mathbf{F}_0 - \mathbf{F}_2 \quad (\text{B.13})$$

$$\mathbf{F}_2^{(1)} = \begin{pmatrix} qE/\sqrt{2} \\ -qE/\sqrt{2} \end{pmatrix} - \frac{1}{8a} \begin{pmatrix} \varepsilon(a_1 + c_1)/a^2 \\ 4\gamma d_1 \end{pmatrix}, \quad (\text{B.14})$$

where a is the bead radius. At first order in E , or in the inverse elastic parameters, the rod is just translating without rotation. This leads to

$$\sum_j \mu_{ij}^{(0)} \cdot \mathbf{F}_i^{(1)} = \mathbf{v}^{(1)}, \quad i = 0, 1, 2, \quad (\text{B.15})$$

where $\mu_{ij}^{(0)}$ is the Rotne-Prager tensor at zeroth order. Together with the constraint $\sum_i \mathbf{F}_i = 0$, it can be solved for the unknowns $\mathbf{F}_0^{(1)}$, $\mathbf{F}_2^{(1)}$ and $\mathbf{v}^{(1)}$:

$$\mathbf{F}_0^{(1)} = \mathbf{F}_2^{(1)} = \begin{pmatrix} 216/185 \\ -72/55 \end{pmatrix} qE/\sqrt{2} \quad (\text{B.16})$$

$$\mathbf{v}^{(1)} = \begin{pmatrix} 312/185 \\ -11/55 \end{pmatrix} \mu_0 qE/\sqrt{2}. \quad (\text{B.17})$$

As before, μ_0 is the Stokes mobility of a single bead. Comparison with eqs.(B.12-B.14) yields

$$\frac{a_1 + c_1}{2} = -\frac{124}{185} \frac{qEa^3}{\sqrt{2}\varepsilon} \quad (\text{B.18})$$

$$b_1 = d_1 = \frac{34}{55} \frac{qEa}{\sqrt{2}\gamma}. \quad (\text{B.19})$$

Using this relations, the mobility tensor to first order $\mu_{ij}^{(1)}$ and the forces up to second order $\mathbf{F}_i^{(2)}$ are calculated and plugged into the relation

$$\sum_j \left[\mu_{ij}^{(0)} \cdot \mathbf{F}_j^{(1)} + \mu_{ij}^{(0)} \cdot \mathbf{F}_j^{(2)} + \mu_{ij}^{(1)} \cdot \mathbf{F}_j^{(1)} \right] + \mathcal{O}(E^3) = \mathbf{v}^{(1)} + \mathbf{v}_i^{(2)}. \quad (\text{B.20})$$

If one assumes that $\mathbf{v}_i^{(2)}$ is a pure rotation of the chain around the center bead, i.e. $\mathbf{v}_0^{(2)} = -\mathbf{v}_2^{(2)}$ and $\mathbf{v}_1^{(2)} = \mathbf{0}$, one finds

$$a_1 = c_1, \quad a_2 = -c_2, \quad b_2 = -d_2, \quad (\text{B.21})$$

and the final result

$$v_{0x}^{(2)} = -v_{2x}^{(2)} = \mu_0 (qEa)^2 \frac{-139810\gamma + 204833\varepsilon/a^2}{1302400\gamma\varepsilon}. \quad (\text{B.22})$$

The orientation is a generic second order effect in E . It vanishes if

$$\gamma = \frac{204833}{139810} \frac{\varepsilon}{a^2} \approx 1.456 \frac{\varepsilon}{a^2}, \quad (\text{B.23})$$

which leads to eq. (3.46) for $L = 4a$. For the Oseen tensor one finds the simpler relation

$$\gamma = \frac{55}{14} \frac{\varepsilon}{a^2} \approx 3.929 \frac{\varepsilon}{a^2}. \quad (\text{B.24})$$

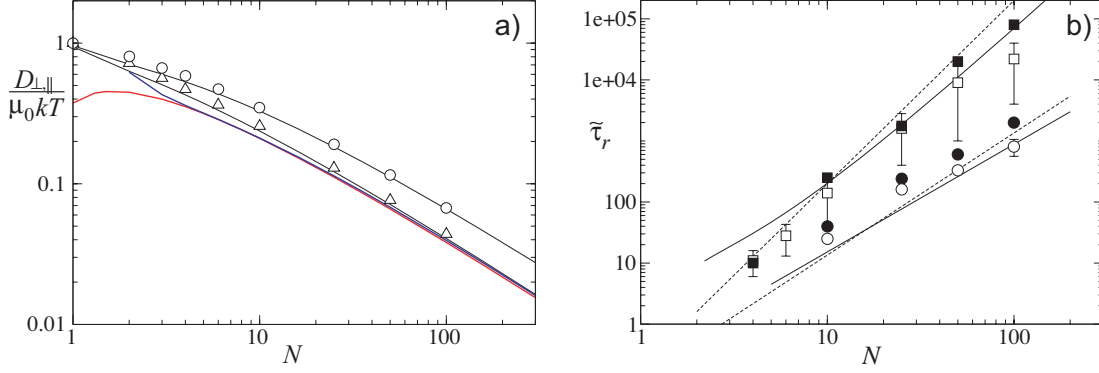


Figure B.2: a) Simulations of the diffusion constant of a neutral rod with $\ell_p = 5L$ for parallel (circles) and perpendicular motion (triangles). Cylinder model of eq. (B.29) for parallel (upper black line) and perpendicular motion (lower black line). Cylinder model of eq. (B.28) (blue line) and prolate ellipsoid model of eq. (B.30) (red line) both for perpendicular motion. b) Rotational diffusion times τ_r with (white symbols) and without hydrodynamic interactions for flexible (circles) and rod-like (squares) chains. Some error bars are neglected for visibility. Solid lines display eq. (B.35) and eq. (B.37) (top to bottom); the dashed lines are a N^3 fit to the free draining simulations and eq. (B.36).

B.3 Consistency checks with analytical results

In this appendix some equilibrium and non-equilibrium quantities for a single neutral flexible or stiff chain will be tested against known analytical results [32]. The Langevin equation (3.7) is used which includes temperature effects. It is the aim of this section to check the simulation results of this thesis for possible numerical artifacts.

Translational diffusion and mobility

Rod-like chains ($\ell_p = 5L$, $\tilde{\gamma} = 4\ell_p/a$) with various N are simulated by Brownian dynamics. By looking at the configurations it is assured that the chains are always very prolate. After short time intervals $\Delta t = 0.1 a^2 / (\mu_0 k_B T)$ (total simulation time $10^5 \Delta t$), the center of mass displacements of the chain parallel, $\Delta R_{CM}^{\parallel}(t_n) \equiv \Delta \mathbf{R}_{CM}(t_n) \cdot \mathbf{R}_e(t_n) / R_e(t_n)$, and perpendicular, $\Delta R_{CM}^{\perp}(t_n)$, to its long axis (i.e. end-to-end vector $\mathbf{R}_e = \mathbf{r}_{N-1} - \mathbf{r}_0$) are calculated:

$$D_{\perp} = \left(\sum_n \Delta R_{CM}^{\perp}(t_n) \right)^2 / (2 \sum_n \Delta t) \quad (\text{B.25})$$

$$D_{\parallel} = \left(\sum_n \Delta R_{CM}^{\parallel}(t_n) \right)^2 / (4 \sum_n \Delta t) \quad (\text{B.26})$$

$$\begin{aligned} D_G &= 1/3 (D_{\parallel} + 2D_{\perp}) \\ &= \left(\sum_n \Delta R_{CM}(t_n) \right)^2 / (6 \sum_n \Delta t). \end{aligned} \quad (\text{B.27})$$

n counts the 10^5 measurement points. The results are compared with analytical (approximate) solutions for long cylinders of Broersma (communicated by Newman et al. [125]) where L is

identified with the length and a with the radius of the cylinder,

$$\begin{aligned} D_{\perp} &= \frac{k_B T}{4\pi\eta L} \left[\ln(L/a) - 0.19 + 4.2 (0.39 - 1/\ln(L/a))^2 \right] \\ D_{\parallel} &= \frac{k_B T}{2\pi\eta L} \left[\ln(L/a) - 1.27 + 7.4 (0.34 - 1/\ln(L/a))^2 \right], \end{aligned} \quad (\text{B.28})$$

with the cylinder calculation of Tirado et al. [172],

$$\begin{aligned} D_{\perp} &= \frac{k_B T}{4\pi\eta L} \left[\ln(L/2a) + 0.839 + 0.185(2a/L) + 0.233(2a/L)^2 \right] \\ D_{\parallel} &= \frac{k_B T}{2\pi\eta L} \left[\ln(L/2a) - 0.207 + 0.98(2a/L) - 0.133(2a/L)^2 \right], \end{aligned} \quad (\text{B.29})$$

and with simplified estimates for ellipsoids (cf. also [139]), in which case L is identified with the long and $2a$ with the short axis of the ellipsoid,

$$\begin{aligned} D_{\perp} &= \frac{k_B T}{4\pi\eta L} [\ln(L/2a) + 0.5] \\ D_{\parallel} &= \frac{k_B T}{2\pi\eta L} [\ln(L/2a) - 0.5]. \end{aligned} \quad (\text{B.30})$$

Fig. B.2a shows good agreement of all calculations at great N but discrepancies for about $N < 10$. The model of Tirado et al. seems to be best suited especially for short chains as it includes numerical correction for end effects. The infinite chain prediction $D_{\parallel}/D_{\perp} = 2$ is approached only logarithmically as can be seen e.g. in the case of eq (B.29) from

$$\frac{D_{\parallel}}{D_{\perp}} \approx 2 \left[1 - \frac{1.05}{\ln(L/2a) + 0.84} \right]. \quad (\text{B.31})$$

Rotational diffusion

In terms of the time correlation function of the normalized end-to-end distance vector $\mathbf{u} := \mathbf{R}_e/|R_e|$ the rotational diffusion time τ_r and coefficient D_r of a polymer are defined by [32],

$$C_{\mathbf{u}\mathbf{u}}(t) \equiv \langle \mathbf{u}(t) \cdot \mathbf{u}(0) \rangle = \exp(-2 D_r t) = \exp(-t/\tau_r). \quad (\text{B.32})$$

In chapters 3 and 7 the total simulation time is at least an order of magnitude longer than the rotational diffusion time of the polymer.

For a *rod-like polymer* the expression for birefringence (cf. chap. 3) reads

$$\Delta n \approx \Delta n_s \chi = \Delta n_s \left\langle \frac{3}{2} \left[\mathbf{u}(t) \cdot \frac{\mathbf{E}}{E} \right]^2 - \frac{1}{2} \right\rangle, \quad (\text{B.33})$$

where Δn_s is the saturation birefringence. Setting $\mathbf{u}(0) = \mathbf{E}/E$ results in the rotational diffusion time τ_r being one third of the slowest relaxation time τ_{relax} of the birefringence signal [48]

$$\begin{aligned} \Delta n &= \Delta n_s \exp(-t/\tau_{\text{relax}}) \\ &= \Delta n_s \exp(-3t/\tau_r) = \Delta n_s \exp(-6 D_r t). \end{aligned} \quad (\text{B.34})$$

A typical way of obtaining τ_r or D_r is to plot $C_{\mathbf{u}\mathbf{u}}(t) := \int \mathbf{u}(t+t_0) \cdot \mathbf{u}(t_0) dt_0$ versus time on a logarithmic scale. Due to the cubic dependence of the diffusion time of stiff chains on the length, $\tau_r \sim N^3$, one is quickly led to unmanageable long simulation times. Nevertheless, qualitative agreement between simulation and theory is achieved (fig. B.2b): For rods with hydrodynamic interactions the cylinder model by Tirado et al. [172] is used

$$D_r = \frac{1}{2\tau_r} = \frac{k_B T}{3\pi\eta L^3} \left[\ln(L/2a) - 0.662 + 0.917(2a/L) - 0.05(2a/L)^2 \right]. \quad (\text{B.35})$$

If hydrodynamic interactions are neglected τ_r scales as N^3 for rod-like polymer. Fig. B.2b displays a fit to the first four data points.

Flexible chains in the free draining case are approximately described by the Rouse model,

$$\tau_r = \frac{4a^2}{3\pi^2\mu_0 k_B T} N^2, \quad (\text{B.36})$$

where (among other things) the excluded volume is neglected; or by the good solvent Zimm model (in the case of hydrodynamic interactions),

$$\tau_r = \frac{a^2}{6\pi^2\mu_0 k_B T} (R_g/a)^3, \quad (\text{B.37})$$

where R_g is taken from Fig. 6.1 and incorporates excluded volume interactions. Fig. B.2b shows already huge error bars; also some systematic underestimation of τ_r for the highest N values due to the finite stiffness might well be present. But, all in all, one can conclude that the simulations reproduce the known analytical results.

B.4 Diffusion of semiflexible chains - some calculations

The explicit result of Yamakawa's diffusion constant of a semiflexible chain [189] of section 6.1 for the two cases, $L > 4.556 \ell_P$ and $L \leq 4.556 \ell_P$, reads up to $\mathcal{O}(d/L)^5$ and $\mathcal{O}(d/\ell_P)^5$

$$D(L > 4.556 \ell_P) = \frac{k_B T}{3\pi\eta L} \left\{ \frac{4}{3} \sqrt{\frac{6}{\pi}} \left(\frac{L}{2\ell_P} \right)^{1/2} + A_2 + A_3 \left(\frac{L}{2\ell_P} \right)^{-1/2} + A_4 \left(\frac{L}{2\ell_P} \right)^{-1} + A_5 \left(\frac{L}{2\ell_P} \right)^{-3/2} \right\} \quad (\text{B.38})$$

$$D(L \leq 4.556 \ell_P) = \frac{k_B T}{3\pi\eta L} \left\{ C_1 \ln \left(\frac{L}{d} \right) + C_2 + C_3 \left(\frac{L}{2\ell_P} \right) + C_4 \left(\frac{L}{2\ell_P} \right)^2 + C_5 \left(\frac{L}{2\ell_P} \right)^3 + C_6 \left(\frac{d}{L} \right) \ln \left(\frac{L}{d} \right) + C_7 \left(\frac{d}{L} \right) + C_8 \left(\frac{d}{L} \right)^2 + C_9 \left(\frac{d}{L} \right)^3 + C_{10} \left(\frac{d}{L} \right)^4 \right\}. \quad (\text{B.39})$$

$d = 2a$ is the diameter of the bent cylinder. The coefficients are given by

$$A_2 = - \left[1 - 0.01412 \left(\frac{d}{2\ell_P} \right)^2 + 0.00592 \left(\frac{d}{2\ell_P} \right)^4 \right] \ln \frac{d}{2\ell_P} - 1.0561 - 0.1667 \frac{d}{2\ell_P}$$

$$\begin{aligned}
& -0.19 \left(\frac{d}{2\ell_P} \right)^2 - 0.0224 \left(\frac{d}{2\ell_P} \right)^3 + 0.019 \left(\frac{d}{2\ell_P} \right)^4 \\
A_3 &= 0.1382 + 0.0691 \left(\frac{d}{2\ell_P} \right)^2 \\
A_4 &= - \left[0.04167 \left(\frac{d}{2\ell_P} \right)^2 + 0.00567 \left(\frac{d}{2\ell_P} \right)^4 \right] \ln \frac{d}{2\ell_P} - 0.3301 + 0.5 \frac{d}{2\ell_P} \\
& - 0.5854 \left(\frac{d}{2\ell_P} \right)^2 - 0.0094 \left(\frac{d}{2\ell_P} \right)^3 - 0.0421 \left(\frac{d}{2\ell_P} \right)^4 \\
A_5 &= -0.03 + 0.1209 \left(\frac{d}{2\ell_P} \right)^2 + 0.0259 \left(\frac{d}{2\ell_P} \right)^4 \tag{B.40}
\end{aligned}$$

and

$$\begin{aligned}
C_1 &= 1 - 0.01412 \left(\frac{d}{2\ell_P} \right)^2 + 0.00592 \left(\frac{d}{2\ell_P} \right)^4 \\
C_2 &= 0.3863 - 0.1667 \frac{d}{2\ell_P} - 0.0016 \left(\frac{d}{2\ell_P} \right)^2 - 0.0224 \left(\frac{d}{2\ell_P} \right)^3 - 0.0007 \left(\frac{d}{2\ell_P} \right)^4 \\
C_3 &= 0.1667 + 0.0222 \left(\frac{d}{2\ell_P} \right)^2 + 0.0017 \left(\frac{d}{2\ell_P} \right)^4 \\
C_4 &= 0.01883 - 0.00789 \left(\frac{d}{2\ell_P} \right)^2 - 0.00038 \left(\frac{d}{2\ell_P} \right)^4 \\
C_5 &= -0.002039 + 0.000805 \left(\frac{d}{2\ell_P} \right)^2 + 0.000017 \left(\frac{d}{2\ell_P} \right)^4 \\
C_6 &= 0.04167 \frac{d}{2\ell_P} + 0.00567 \left(\frac{d}{2\ell_P} \right)^3 \\
C_7 &= 0.5 + 0.0786 \frac{d}{2\ell_P} - 0.0094 \left(\frac{d}{2\ell_P} \right)^2 + 0.0107 \left(\frac{d}{2\ell_P} \right)^3 + 0.0039 \left(\frac{d}{2\ell_P} \right)^4 \\
C_8 &= -0.0625 + 0.00132 \left(\frac{d}{2\ell_P} \right)^2 - 0.00055 \left(\frac{d}{2\ell_P} \right)^4 \\
C_9 &= 0.001302 \frac{d}{2\ell_P} + 0.000181 \left(\frac{d}{2\ell_P} \right)^3 \\
C_{10} &= 0.001953 - 0.000064 \left(\frac{d}{2\ell_P} \right)^2 + 0.000027 \left(\frac{d}{2\ell_P} \right)^4 . \tag{B.41}
\end{aligned}$$

Bibliography

- [1] M.P. Allen and D.J. Tildesley, *Computer Simulations of Liquids* (Clarendon Press, Oxford, 1987).
- [2] E. Anderson et al., *LAPACK Users' Guide*, 3rd ed. (SIAM, Philadelphia, 1999).
- [3] O. Alarcón-Waess and E. González-Tovar, *Chem. Phys. Lett.* **239**, 201 (1995).
- [4] J.M. Antosiewicz and D. Porschke, *Biophys. Chem.* **33**, 19 (1989).
- [5] H. Asai and N. Watanabe, *Biopolymers* **15** 383 (1976).
- [6] J.-L. Barrat, J.-F. Joanny. *Theory of Polyelectrolyte Solutions*, *Adv. Chem. Phys.* **94**, 1 (1996).
- [7] A.R. Bausch and K. Kroy, *Nature Physics* **2**, 231 (2006).
- [8] J. Bayer and J. O. Rädler, *Electrophoresis* (2006), in press.
- [9] C.W.J. Beenakker, *J. Chem. Phys.* **85**, 1581 (1986).
- [10] H.C. Berg and R.A. Anderson, *Nature* **245**, 380 (1973).
- [11] R.M. Berry and H.C. Berg, *Biophys. J.* **76**, 580 (1999).
- [12] J. Bertolotto, M. Campo, G. Roston, and M. Ascheri, *Colloids Surf. A* **203**, 167 (2002).
- [13] J. Bertolotto, G. Roston, M. Ascheri, and M. Campo, *Physica A* **327**, 185 (2003).
- [14] J. Bertolotto, G. Roston, and M. Ascheri, *Prog. Colloid Polym. Sci.* **128**, 25 (2004).
- [15] N. Bjerrum, *Kgl. Danske Videnskab. Selskab. Mat.-fys. Medd.* **7**, 1 (1926).
- [16] F. Booth, *J. Chem. Phys.* **22**, 1956 (1954).
- [17] F. Bordi, C. Cametti, and R.H. Colby, *J. Phys.: Condens. Matter* **16**, R1423 (2004).
- [18] J.C. Borges, H. Fischer, A.F. Craievich, and C.H.I. Ramos, *J. Biol. Chem.* **280**, 13671 (2005).
- [19] C.J.F. Böttcher and P. Bordewijk. *Theory of Electric Polarization*, Vol. 2 (Elsevier, Amsterdam, 1978).
- [20] S. Broersma, *J. Chem. Phys.* **32**, 1626 (1960).

- [21] J. Buitenhuis and A.P. Philipse, *J. Colloid Interface Sci.* **176**, 272 (1995).
- [22] M.E. Cates, *J. Phys. II France* **2**, 1109 (1992).
- [23] S. Chen and G.D. Doolen, *Annu. Rev. Fluid Mech.* **30**, 329 (1998).
- [24] S. Childress, *Mechanics of Swimming and Flying* (Cambridge University Press, Cambridge, 1981).
- [25] G. Ciccotti and G. Jacucci, *Phys. Rev. Lett.* **35**, 789 (1975).
- [26] R.W. Clark and C.S. Lange, *Biopolymers* **19**, 945 (1980).
- [27] H. Clausen-Schaumann, M. Seitz, R. Krautbauer, H.E. Gaub, *Curr. Op. Chem. Biol.* **4**, 524 (2000).
- [28] H. Cölfen, manuscript in preparation (2006).
- [29] G. Cruz de León, M. Medina-Noyola, O. Alarcón-Waess, and H. Ruiz-Estrada, *Chem. Phys. Lett.* **207**, 294 (1993).
- [30] J.M. Deutch and I. Oppenheim, *J. Chem. Phys.* **54**, 3547 (1971).
- [31] Z. Dogic and S. Fraden, *Phys. Rev. Lett.* **78**, 2417 (1997).
- [32] M. Doi and S.F. Edwards, *The Theory of Polymer Dynamics* (Clarendon Press, Oxford, 1986).
- [33] R. Dreyfus, J. Baudry, M.L. Roper, M. Fermigier, H.A. Stone and J. Bibette, *Nature* **437**, 862 (2005).
- [34] L. Durlafsky, J.F. Brady, and G. Bossis, *J. Fluid Mech.* **180**, 21 (1987).
- [35] J.G. Elias and D. Eden, *Macromolecules* **14**, 410 (1981).
- [36] C. Elvingson, *Biophys. Chem.* **43**, 9 (1992).
- [37] C. Elvingson, *Chem. Phys. Lett.* **214**, 91 (1993).
- [38] D.L. Ermak and J.A. McCammon, *J. Chem. Phys.* **69**, 1352 (1978).
- [39] I. Ermolina et al., *Biochimica et Biophysica Acta* **1622**, 57 (2003).
- [40] B.U. Felderhof, *Physica A* **89**, 373 (1977).
- [41] M. Fixman, *Macromolecules* **14**, 1710 (1981).
- [42] M. Fixman, *J. Chem. Phys.* **75**, 4040 (1981).
- [43] M. Fixman and S. Jagannathan, *J. Chem. Phys.* **75**, 4048 (1981).
- [44] M. Fixman, *Macromolecules* **19**, 1204 (1986).
- [45] H. Flores et al., *Bull. Math. Biol.* **67**, 137 (2005).
- [46] H. Flyvbjerg and H.G. Petersen, *J. Chem. Phys.* **91**, 461 (1989).

- [47] S. Fraden, in: M. Baus et al. (eds.), *Observation, Prediction, and Simulation of Phase Transitions in Complex Fluids* (Kluwer Academic Publ., Dordrecht, 1995).
- [48] E. Fredericq and C. Houssier, *Electric Dichroism and Electric Birefringence* (Clarendon Press, Oxford, 1973).
- [49] H. Freundlich, *Zeitschr. Elektrochemie* **22**, 27 (1916).
- [50] J.M. García Bernal and J. García de la Torre, *Biopolymers* **19**, 751 (1980).
- [51] J.M. García Bernal, M.M. Tirado, J.J. Freire and J. García de la Torre, *Macromolecules* **23**, 3357 (1990).
- [52] J.M. García Bernal, M.M. Tirado, J.J. Freire and J. García de la Torre, *Macromolecules* **24**, 593 (1991).
- [53] J. García de la Torre and V.A. Bloomfield, *Biophys. J.* **20**, 49 (1977).
- [54] J. García de la Torre and V.A. Bloomfield, *Quat. Rev. Biophys.* **14**, 81 (1981).
- [55] J. García de la Torre, M.C. López Martínez, M.M. Tirado, and J.J. Freire, *Macromolecules* **17**, 2715 (1984).
- [56] U. Geigenmüller, *Chem. Phys. Lett.* **110**, 666 (1984).
- [57] F. Gittes, B. Mickey, J. Nettleton and J. Howard, *J. Cell Biol.* **120**, 923 (1993).
- [58] R.F. Goldstein, *J. Chem. Phys.* **83**, 2390 (1985).
- [59] R. Götter, K. Kroy, E. Frey, M. Bärmann, and E. Sackmann, *Macromolecules* **29**, 30 (1996).
- [60] R.D. Groot and P.B. Warren, *J. Chem. Phys.* **107**, 4423 (1997).
- [61] J. Gray and G.J. Hancock, *J. Exptl. Biol.* **32**, 802 (1955).
- [62] P.D. Grossman and D.S. Soane, *Anal. Chem.* **62**, 1592 (1990).
- [63] J. Happel and H. Brenner, *Low Reynolds Number Hydrodynamics*, 2nd ed. (Nordhoff Intern. Publ., Leyden, 1973).
- [64] S.E. Harding et al., *Analytical Ultracentrifugation in Biochemistry and Polymer Science* (Royal Soc. Chem., Cambridge, 1993).
- [65] L. Harnau, R.G. Winkler, and P. Reineker, *J. Chem. Phys.* **104**, 6355 (1996).
- [66] W. Heller, *Rev. Mod. Phys.* **14**, 390 (1942).
- [67] J. Higdon, *J. Fluid Mech.* **90**, 685 (1979).
- [68] D.A. Hoagland, E. Arvanitidou, and C. Welch, *Macromolecules* **32**, 6180 (1999).
- [69] H. Hoffmann, U. Krämer, and H. Thurn, *J. Phys. Chem.* **94**, 2027 (1990).

- [70] M. Hogan, N. Dattaguota, and D.M. Crothers, Proc. Natl. Acad. Sci. USA **75**, 195 (1978).
- [71] L. Hong and S. Granick, J. Polym. Sci. B **43**, 3497 (2005).
- [72] J. Horbach and D. Frenkel, Phys. Rev. E **64**, 061507 (2001).
- [73] R.M. Jendrejack, M.D. Graham, and J.J. de Pablo, J. Chem. Phys. **113**, 2894 (2000).
- [74] J.G. Kirkwood, J. Polym. Sci. **12**, 1 (1954).
- [75] S. Kim and S.J. Karila, *Microhydrodynamics* (Butterwoth-Heinemann, Boston, 1991).
- [76] M. Kim et al., PNAS **100**, 15481 (2003).
- [77] M. Kim and T.R. Powers, Phys. Rev. E **69**, 061910 (2004).
- [78] S. Kobayasi, H. Asai, and F. Oosawa, Biochim. et Biophys. Acta **88**, 528 (1964).
- [79] S. Kobayasi, Biochim. et Biophys. Acta **88**, 541 (1964).
- [80] M. Kollmann and G. Nägele, J. Chem. Phys. **113**, 7672 (2000).
- [81] H. Kramer et al., Macromolecules **25**, 4325 (1992).
- [82] H. Kramer et al., J. Phys. II France **4**, 1061 (1994).
- [83] O. Kratky and G. Porod, Recueil **68**, 1106 (1949).
- [84] K. Kremer and F. Müller-Plathe, Molecular Simulation **28**, 729 (2002).
- [85] H.J. Kreuzer, *Nonequilibrium Thermodynamics and its Statistical Foundations* (Clarendon Press, Oxford, 1981).
- [86] O. Krichevsky and G. Bonnet, Rep. Prog. Phys. **65**, 251 (2002).
- [87] K. Kroy and E. Frey, Phys. Rev. E **55**, 3092 (1997).
- [88] R. Kubo, Rep. Prog. Phys. **29**, 255 (1966).
- [89] K. Lachenmayer and W. Oppermann, J. Chem. Phys. **116**, 392 (2002).
- [90] L.D. Landau and E.M. Lifschitz, *Hydrodynamik*, 5th ed. (Akademie Verlag, Berlin, 1991).
- [91] L.D. Landau and E.M. Lifschitz, *Elastizitätstheorie*, 7th ed. (Akademie Verlag, Berlin, 1991).
- [92] T.M. Laue and W.F. Stafford, Ann. Rev. Biophys. Biomol. Struct. **28**, 75 (1999).
- [93] M.A. Lauffer, J. Am. Chem. Soc. **61**, 2412 (1939).
- [94] R.G. Lewis, R. Pecora, and D. Eden, Macromolecules **20**, 2579 (1987).
- [95] J. Lighthill, *Mathematical Biofluidynamics* (SIAM Special Issue, Philadelphia, 1975).

- [96] J. Lighthill, *SIAM Review* **18**, 161 (1976).
- [97] L. Livadaru, R.R. Netz, and H.J. Kreuzer, *Macromolecules* **36**, 3732 (2003).
- [98] H.A. Lorentz, *Zittungsverslag Koninkl. Akad. Wetenschappen Amsterdam* **5**, 168 (1896); reprint in English: *J. Eng. Math* **30**, 19 (1996).
- [99] D. Lumma, S. Keller, T. Vilgis, and J.O. Rädler, *Phys. Rev. Lett.* **90**, 218301 (2003).
- [100] N. Madras, *Lectures on Monte Carlo Methods*, (Fields Institute Communications, Toronto, 1998).
- [101] A. Malevanets and R. Kapral, *J. Chem. Phys.* **110**, 8605 (1999).
- [102] M. Mandel, *Mol. Phys.* **4**, 489 (1961).
- [103] M. Mandel and T. Odijk, *Ann. Rev. Phys. Chem.* **35**, 75 (1984).
- [104] M. Manghi and R. R. Netz, *Eur. Phys. J. E* **14**, 67 (2004).
- [105] M. Manghi, X. Schlagberger and R. R. Netz, *Phys. Rev. Lett.* **96**, 068101 (2006).
- [106] M. Manghi, X. Schlagberger, Y.-W. Kim, and R.R. Netz, *Soft Matter*, in press (2006).
- [107] G.S. Manning, *Biophys. Chem.* **9**, 65 (1978).
- [108] G.S. Manning, *J. Chem. Phys.* **85**, 1506 (1981).
- [109] G.S. Manning, *J. Chem. Phys.* **90**, 5704 (1989).
- [110] G.S. Manning and U. Mohanty, *Physica A* **247**, 196 (1997).
- [111] C. Martin et al., *J. Phys. II France* **5**, 697 (1995).
- [112] P. Mazur and W. van Saarloos, *Physica A* **115**, 21 (1982).
- [113] M.G. McPhie and G. Nägele, *J. Phys.: Cond. Mat.* **16**, S4021 (2004).
- [114] M. Medina-Noyola and A. Vizcarra-Rendón, *Phys. Rev. A* **32**, 3596 (1985).
- [115] J.M. Méndez-Alcaraz and O. Alarcón-Waess, *Physica A* **268**, 75 (1999).
- [116] P. Model and M. Russel, in *The Bacteriophages*, edited by P. Calender (Plenum, New York, 1988).
- [117] U. Mohanty and Y. Zhao, *Biopolymers* **3**, 377 (1996).
- [118] H. Mori, *Prog. Theor. Phys.* **33**, 423 (1965).
- [119] G. Nägele, *Phys. Rep.* **272**, 215 (1996).
- [120] J. Narayanan, E. Mendez, and C. Manohar, *J. Chem. Phys.* **100**, 18524 (1996).
- [121] R.R. Netz and H. Orland, *Eur. Phys. J. E* **1**, 203 (2000).
- [122] R.R. Netz, *Phys. Rev. Lett.* **90**, 128104 (2003).

- [123] R.R. Netz, J. Phys. Chem. B **107**, 8208 (2003).
- [124] R.R. Netz and D. Andelman, Phys. Rep. **380**, 1 (2003).
- [125] J. Newman, H.L. Swinney, and L.A. Day, J. Mol. Biol. **116**, 593 (1977).
- [126] T. Nicolai and M. Mandel, Macromolecules **22**, 2348 (1989).
- [127] T. Odijk, J. Polym. Sci. **15**, 477 (1977).
- [128] T. Odijk, Coll. Surf. A **210**, 191 (2002).
- [129] H. Ohshima, T.W. Healy, L.R. White, and R.W. O'Brian, J. Chem. Soc. Faraday Trans. 2 **80**, 1299 (1984).
- [130] C.T. O'Konski and B.H. Zimm, Science **111**, 113 (1950).
- [131] C.T. O'Konski and A.J. Haltner, J. Am. Chem. Soc. **78**, 3604 (1956).
- [132] C.T. O'Konski and A.J. Haltner, J. Am. Chem. Soc. **79**, 5634 (1957).
- [133] C.T. O'Konski and S. Krause, J. Phys. Chem. **74**, 3243 (1970).
- [134] B. Øksendal, *Stochastic Differential Equations* (Springer, Berlin, 1992).
- [135] F. Oosawa, Biopolymers **9**, 677 (1970).
- [136] W. Oppermann, Makromol. Chem. **189**, 927 (1988); *ibid.* 2125.
- [137] C.W. Oseen, *Neuere Methoden und Ergebnisse in der Hydrodynamik* (Akademische Verlagsgesellschaft, Leipzig, 1927).
- [138] F. Pampaloni, G. Lattanzi, A. Jonáš, T. Surrey, E. Frey, and E. Florin, *Elastic properties of grafted microtubules*, arXiv:q-bio.BM/0503037 v1 (2005).
- [139] F. Perrin, Journal de Physique et la Radium **7/5**, 497 (1934).
- [140] D. Porschke, Biophys. Chem. **49**, 127 (1994).
- [141] D. Porschke and J.M. Antosiewicz, J. Phys. Chem. B **109**, 1034 (2005).
- [142] T.R. Powers, Phys. Rev. B **65**, 040903 (2002).
- [143] C. Pozrikidis. *Boundary Integral and Singularity Methods for Linearized Viscous Flow*, (Cambridge University Press, Cambridge, 1992).
- [144] W.H. Press, S.A. Teukolsky, W.T. Vetterling, and B.P. Flannery. *Numerical Recipes in C++*, 2nd ed. (Cambridge University Press, Cambridge (UK) 2002).
- [145] E.M. Purcell, Am. J. Physics **45**, 3 (1977).
- [146] E.J. Ralston and V.N. Schumaker, Biophys. Chem. **9**, 375 (1979).
- [147] D.C. Rau and E. Charney, Biophys. Chem **14**, 1 (1981).
- [148] D.C. Rau and E. Charney, Macromolecules **16**, 1653 (1983).

- [149] P. Résibois, *Electrolyte Theory* (Harper and Row, New York, 1968).
- [150] I. Rouzina and V.A. Bloomfield, *J. Phys. Chem.* **100**, 9977 (1996).
- [151] I. Rubenstein and S.B. Leighton, *Biophys. Chem.* **1**, 292 (1974).
- [152] E. Sackmann, *Macromol. Chem. Phys.* **195**, 7 (1994).
- [153] X. Schlagberger and R.R. Netz, *Europhys. Lett.* **70**, 129 (2005); *ibid.* 563.
- [154] X. Schlagberger, J. Bayer, J.O. Rädler, and R.R. Netz, *Salt-dependent diffusion of semiflexible charged polymers*, submitted to *Europhys. Lett.* (2006).
- [155] X. Schlagberger and R.R. Netz, *Hydrodynamic orientation: a new look at anomalous birefringence*, manuscript in preparation (2006).
- [156] R. Schmitz and B.U. Felderhof, *Physica A* **116**, 163 (1982).
- [157] G.A. Schumacher and T.G.M. van der Ven, *Faraday Discuss. Chem. Soc.* **83**, 75 (1987).
- [158] G.A. Schumacher and T.G.M. van der Ven, *J. Chem. Soc. Faraday Trans.* **87**, 971 (1991).
- [159] J.M. Schurr, *Chem. Phys.* **45**, 119 (1980).
- [160] G. Schwarz, *Z. Phys.* **145**, 563 (1956).
- [161] J.M. Schurr, *Chem. Phys. Lett.* **110**, 668 (1984).
- [162] E.S.G. Shaqfeh, *J. Newton. Fluid* **130**, 1 (2005).
- [163] J. Skolnick and M. Fixman, *Macromolecules* **10**, 944 (1977).
- [164] G.W. Slater, M. Kenward, L.C. McCormick, and M.G. Gauthier, *Curr. Op. Biotech.* **14**, 58 (2003).
- [165] S.B. Smith, Y. Cui, and C. Bustamante, *Science* **271**, 795 (1996).
- [166] K. Soda, *J. Phys. Soc. Japan* **35**, 866 (1973).
- [167] N. Stellwagen, *Biopolymers* **20**, 399 (1981).
- [168] N. Stellwagen, C. Gelfi, and P.G. Righetti, *Biopolymers* **42**, 687 (1997).
- [169] N. Stellwagen, S. Magnúsdóttir, C. Gelfi, and P.G. Righetti, *Biopolymers* **58**, 390 (2001).
- [170] E. Stellwagen, Y. Lu, and N. Stellwagen, *Biochemistry* **42**, 11745 (2003).
- [171] V. Symeonidis, G.E. Karniadakis, and B. Caswell, *Phys. Rev. Lett.* **95**, 076001 (2005).
- [172] M.M. Tirado, C.L. Martinez, J. García de la Torre, *J. Chem. Phys.* **81**, 2047 (1984).
- [173] L. Turner, W.S. Ryu and H. Berg, *J. Bacteriol.* **182**, 2793 (2000).
- [174] T.G.M. van der Ven, *Colloidal Hydrodynamics* (Academic Press, London, 1989).

- [175] W. van Dijk, F. van der Touw, and M. Mandel, *Macromolecules* **14**, 792 (1981).
- [176] A. Vizcarra-Rendón, M. Medina-Noyola, and R. Klein, *Chem. Phys. Lett.* **173**, 397 (1990).
- [177] L. Wang, M.M. Garner, and H. Yuk, *Macromolecules* **24**, 2368 (1991).
- [178] H. Washizu and K. Kikuchi, *Chem. Phys. Lett.* **320**, 277 (2000).
- [179] H. Washizu and K. Kikuchi, *J. Phys. Chem. B* **106**, 11329 (2002).
- [180] W.A. Wegener, *Biopolymers* **20**, 303 (1981).
- [181] W.A. Wegener, *J. Chem. Phys.* **84**, 5989 (1986).
- [182] M. Wien, *Ann. Phys.* **83**, 327 (1927).
- [183] C.H. Wiggins and R.E. Goldstein, *Phys. Rev. Lett.* **80**, 3879 (1998).
- [184] A. Wilk, J. Gapinski, A. Patkowski, and R. Pecora, *J. Chem. Phys.* **121**, 10794 (2004).
- [185] R.G. Winkler, M. Gold, and P. Reineker, *Phys. Rev. Lett.* **80**, 3731 (1998).
- [186] R.G. Winkler, K. Mussawisade, M. Ripoll, and G. Gompper, *J. Phys.: Condens. Matter* **16**, S3941 (2004).
- [187] C.W. Wolgemuth, *Phys. Rev. Lett.* **84**, 1623 (2000).
- [188] H. Yamakawa, *J. Chem. Phys.* **53**, 436 (1970).
- [189] H. Yamakawa and M. Fujii, *Macromolecules* **6**, 407 (1973).
- [190] M. Yoshida, K. Kikuchi, T. Maekawa, and H. Watanabe, *J. Phys. Chem.* **96**, 2027 (1992).
- [191] B.H. Zimm, *Biophys. Chem.* **1**, 279 (1974).
- [192] B.H. Zimm and V.N. Schumaker, *Biophys. Chem.* **5**, 265 (1976).
- [193] B.H. Zimm, *Macromolecules* **13**, 592 (1980).
- [194] R. Zwanzig, *Nonequilibrium Statistical Mechanics* (Oxford University Press, Oxford, 2001).

List of Publications

1. X. Schlagberger and R.R. Netz, *Orientation of elastic rods in homogeneous Stokes flow*, Europhys. Lett. **70**, 129 (2005).
2. M. Manghi, X. Schlagberger and R. R. Netz, *Propulsion with a rotating elastic nano-rod*, Phys. Rev. Lett. **96**, 068101 (2006).
3. H. Boroudjerdi, Y.-W. Kim, A. Naji, R.R. Netz , X. Schlagberger, and A. Serr, *Statics and dynamics of strongly charged soft matter*, Physics Reports **416**, 129 (2005).
4. M. Manghi, X. Schlagberger, Y.-W. Kim, and R.R. Netz, *Hydrodynamic effects in driven soft matter*, Soft Matter **2**, 653 (2006).
5. X. Schlagberger and R.R. Netz, *Unfolding transition of flexible polymers in an ultracentrifuge*, manuscript in preparation (2006).
6. X. Schlagberger, J. Bayer, J.O. Rädler, and R.R. Netz, *Diffusion of a single semiflexible charged polymer*, submitted to Europhys. Lett. (2006).
7. X. Schlagberger and R.R. Netz, *Hydrodynamic orientation: a new look at anomalous birefringence*, to be submitted to Europhys. Lett. (2006).

List of Figures

1.1	Examples of biologically important semiflexible rods	2
3.1	Stationary deformation of an elastic rod at zero temperature	16
3.2	Distribution of elastic forces along a chain	18
3.3	Schematic drawing of three deformation modes	19
3.4	Dynamic orientation of an isotropic elastic rod	20
3.5	Rescaled orientational parameter as a function of temperature	21
3.6	a) Time evolution of the alignment parameter; b) orientational speed	22
3.7	Phase diagram for anisotropic materials	23
4.1	Transmission electron micrographs of <i>E. coli</i> and <i>Pseudomonas putida</i>	30
4.2	Illustration of the resistive-force and slender-body theories	31
4.3	Sketch of the filament and evolution of the center-of-mass angle	32
4.4	Terminal angular velocity as a function of $1/\varepsilon^*$	33
4.5	Critical torque versus rescaled persistence length	34
4.6	Angular and translational velocity in the case of a moving filament	35
4.7	Propulsion velocity and efficiency as a function of the load	36
5.1	a) Test of the $\gamma \rightarrow \infty$ limit; b) test of Zimm's theory for linear chains	40
5.2	Low field configurations of a $N = 40$ chain	41
5.3	Typical configurations for long chains at high fields	42
5.4	Test of the preaveraging approximation for a FJC	43
5.5	Sedimentation coefficient and radius of gyration for several chain lengths	44
5.6	Snapshots at different field strengths	45
5.7	Maximum extension as a function of the sedimentation field	46
5.8	N -dependence of S in the zero temperature limit	47
5.9	Fluctuations of S and R_z around the maximal elongated chain	48
5.10	Sedimentation coefficient rescaled for low and high fields	49
5.11	Sedimentation coefficient and maximum extension of circular chains	51
5.12	Persistence length dependence of birefringence and sedimentation	52
6.1	Radius of gyration and Flory parameter versus monomer number	54
6.2	Diffusion constant of a neutral semiflexible chain	59
6.3	Test of the linear response regime	61
6.4	Charged rod: simulations and analytical results	62
6.5	Diffusion constant as a function of screening length	64
6.6	Test of the box size dependence and qualitative explanation of the minimum	65

6.7	Electrolyte friction versus bending	67
6.8	Test of the fit formula for 394 bp DNA	68
6.9	Experimental diffusion data of DNA and TMV	69
7.1	E -field dependence of dipole moments and fraction of bound counterions . . .	73
7.2	Dipole moments of a pure salt solution	74
7.3	Charge density and dipole moment increment along the rod	78
7.4	Charge density for different screening lengths	79
7.5	Parallel polarizability as a function of the screening length for various box sizes	81
7.6	Dependence of the parallel polarizability on polymer concentration	82
7.7	Perpendicular polarizability and Kerr constant	83
7.8	Length dependence of polarizabilities and Kerr constant	84
7.9	Polarizability of bound counterions	85
7.10	Perpendicular orientation at high E -fields	86
7.11	Contour plot of the polarizability compared with fd-virus data	87
7.12	a) Chain length dependent crossover; b) screening of hydrodynamic bending .	88
A.1	Test of the approximation made in the correlation of the noise	97
B.1	Sketch of the three-bead model	102
B.2	Diffusion constants of rods, various models	104

Acknowledgments

Many people have helped and supported me during my PhD. First of all I want to express my gratitude to Prof. Roland Netz for supervising my doctoral program and introducing me to the world of soft matter physics. Also for giving me the chance to attend many conferences and get in contact with other scientific groups. From him I learned how important it is to communicate scientific results.

I would like to thank Prof. Joachim Rädler and Johannes Bayer for the interesting collaboration about the diffusion of DNA. With Manoel Manghi I shared not only a project on bacterial propulsion but also many exciting conferences. I am also very grateful to Prof. Erwin Frey for accepting to co-referee my thesis within this tight time limit.

I profited a lot from discussions with all members of our group and attended many wonderful activities. Special thanks to Vladimir Lobaskin for his great help in the context of electrolyte friction, and to Alfredo Alexander Katz for many discussions and hints. Also many thanks to the first chemist in our group, Andreas Serr, for always keeping the social life of our group “alive” and for his spontaneous help in setting up the computers after the move to the TU. To Sebastian Fischer for critically proofreading the manuscript and making an uncountable number of suggestions. It was a great time with all present and former group members, with Thomas Einert, Christian Fleck, Dominik Horinek, Jiri Janecek, Swetlana Jungblut, Uli Gerland, Yong Woon Kim, Paul Näger, Christian Sendner, Hirofumi Wada, and Thomas Westphal. Many thanks also to Sonja Ortner for the friendly atmosphere she provides and for her kind hospitality in Konstanz. Last not least to my first colleagues in this group, Ali Najj and Hoda Boroudjerdi, for helping me getting started and saving me when I was snow-blind in Teheran!

This is the place to thank also my parents for their continuous support over so many years, and my sisters for their help in the last difficult months.

Lebenslauf

Name: Franz *Xaver* Walther Eberhard Schlagberger

Geburtsdatum: 20. September 1975 in Bremen

Schule:

1982 - 1986 Grundschule Prüm

1986 - 1995 Regino-Gymnasium Prüm, altsprachlicher Zweig

Juni 1995 Abitur

Studium:

10/1995 - 08/1998 Physikstudium an der Ruprecht-Karls-Universität Heidelberg

Juli 1997 Abschluss des Vordiploms

09/1998 - 04/1999 Physikstudium (non-degree exchange student)
an der York University, Toronto (Kanada)

05/1999 - 07/2001 Fortsetzung an der Universität Heidelberg

Juli 2001 Hauptdiplom in Physik Universität Heidelberg
Diplomarbeit "Elektroschwache Baryogenese mittels Preheating"
Betreuer Prof. Dr. M.G. Schmidt

01/2002 - 03/2002 Praktikum im Risiko-Controlling der Dresdner Bank in Frankfurt/M.

seit 10/2002 Doktorarbeit an der Ludwig-Maximilians-Universität München
Thema: "Polymerdynamik in äußeren Feldern"
bei Prof. Dr. Roland R. Netz

